3-2006

Characterization of the Field Emission Properties of Carbon Nanotubes Formed on Silicon Carbide Substrates by Surface Decomposition

Michael C. Pochet

CHARACTERIZATION OF THE FIELD EMISSION PROPERTIES OF CARBON NANOTUBE FILMS FORMED ON SILICON CARBIDE SUBSTRATES BY SURFACE DECOMPOSITION

THESIS

Michael C. Pochet, Captain, USAF

AFIT/GE/ENG/06-47

DEPARTMENT OF THE AIR FORCE
AIR UNIVERSITY

AIR FORCE INSTITUTE OF TECHNOLOGY

Wright-Patterson Air Force Base, Ohio

AFIT/GE/ENG/06-47

CHARACTERIZATION OF THE FIELD EMISSION PROPERTIES OF CARBON NANOTUBE FILMS FORMED ON SILICON CARBIDE SUBSTRATES BY SURFACE DECOMPOSITION

THESIS

Presented to the Faculty

Department of Electrical and Computer Engineering

Graduate School of Engineering and Management

Air Force Institute of Technology

Air University

Air Education and Training Command

In Partial Fulfillment of the Requirements for the

Degree of Master of Science in Electrical Engineering

Michael C. Pochet, BS, MBA

Captain, USAF

March 2006

AFIT/GE/ENG/06-47

CHARACTERIZATION OF THE FIELD EMISSION PROPERTIES OF CARBON NANOTUBE FILMS FORMED ON SILICON CARBIDE SUBSTRATES BY SURFACE DECOMPOSITION

Michael C. Pochet, BS, MBA

Captain, USAF

Approved:

/signed/	24 Feb 2006
Lt Col James A. Fellows (Chairman)	date
/signed/	24 Feb 2006
Lt Col James A. Lott (Member)	date
/signed/	24 Feb 2006
Maj LaVern A. Starman (Member)	date

AFIT/GE/ENG/06-47

Abstract

Numerous works found in the literature report that carbon nanotubes have excellent field emission properties, emitting high electron current densities at low electric fields. Recent work by the Air Force Research Laboratory Materials and Manufacturing Directorate has shown that dense arrays of vertically aligned carbon nanotubes (CNTs) form on the surface of silicon carbide wafers during high temperature (1400 – 1700^{o}C) anneals under moderate vacuum conditions (10^{-2} – 10^{-5} Torr).

The novelty of this growth method is that the carbon nanotubes form without the aid of a metal catalyst, allowing for potentially defect free carbon nanotubes to form. In this thesis, carbon nanotube films were grown by the surface decomposition of silicon carbide substrates and the associated field emission characteristics were investigated to determine if films grown using this method possessed advantages over films grown using metal catalyzed methods. The anneal time and vacuum conditions used during growth were varied to determine the optimal conditions necessary for fabricating an effective CNT emission surface. Scanning electron microscopy (SEM), transmission electron microscopy (TEM), and atomic force microscopy (AFM) were used to characterize the surface properties of the fabricated films. The associated turn-on voltage, threshold voltage, and maximum current density exhibited by the CNT films were measured using a standard vacuum tube diode test configuration. The stability of the CNT films' emission current was recorded over finite lengths of time.

The presence of adsorbed oxygen molecules on the CNT film's surface altered the field emission performance of samples in a manner that was not fully understood. In some instances, the application of high strength electric fields (ranging from 7.0 – 13.0 V/μm) resulted in improved field emission characteristics (turn-on electric field and maximum emission current density exhibited); while in other instances, the field emission performances drastically deteriorated.

Although the samples tested did not demonstrate improved field emission characteristics when compared to values found in the literature for catalyst-grown CNT films, the data collected shows that further investigation is warranted regarding the emission capabilities of CNT films formed on SiC by surface decomposition. From the measured CNT data, the lowest turn-on electric field was found to be lower than 3.0 V/μm, while exhibiting a high maximum current density of 4.25 mA/cm^2 at 6.7 V/μm.

Acknowledgments

I would like to express my sincere appreciation to my faculty advisor, Lt Col James Fellows, for his guidance and support throughout the course of this thesis. The insight and experience he bestowed on me was certainly appreciated. I would also like to thank my sponsors, Dr. William Mitchel and Dr. John Boeckl from the Air Force Research Laboratory for both the support and latitude provided to me in this endeavor.

Lastly, I must thank my lovely wife. You have listened to me patiently describe what I have been working on, and you have never failed to encourage and support me. You are the love of my life!

Michael C. Pochet

Table of Contents

Page

Page

List of Figures

Figure Page

Figure Page

Figure Page

Figure Page

Figure Page

Figure Page

List of Tables

CHARACTERIZATION OF THE FIELD EMISSION PROPERTIES OF CARBON NANOTUBE FILMS FORMED ON SILICON CARBIDE SUBSTRATES BY SURFACE DECOMPOSITION

Chapter 1: Introduction

Carbon nanotubes (CNTs) have novel physical properties making them promising materials for future applications in field emission devices.

Numerous works found in the literature shows that CNTs have excellent field emission properties, characterized by achievement of high current densities at low applied electric fields. The goal of this research was to investigate the field emission properties of CNT films formed on silicon carbide substrates by surface decomposition. The research was performed by fabricating CNT films of various growth parameters on silicon carbide substrates and measuring the associated turn-on voltages (electric field needed to produce a current of 10 $\mu A/cm^2$), threshold voltages (electric field needed to produce a current of 10 mA/cm^2) and maximum current densities exhibited. The defined turn-on and threshold voltage values were chosen from a literature reference as figures-of-merit encountered in flat panel display technologies, as given by Bonard *et al.* [1].

The data collected was compared with test data associated with field emission tests performed on CNT films grown using catalyst metals and non-CNT film emitters found in the literature. Additionally, the CNT films' stability and ability to withstand prolonged high field conditions was evaluated.

1.1 General Issue

When flat-panel plasma viewing screens were first introduced, many believed that the quest for the ultimate flat-panel display was over. The large, flat plasma screens with their dazzling brightness and wide viewing angles are the hottest items on the commercial television display market; their drawback, however, is that they consume a great deal of power. Such an ultimate display technology should not be marred by such a costly flaw. It is this drawback that leads researchers to search for the next great innovation in display technologies: displays that consume less power than plasma screens while retaining their brightness, wide viewing angle, and size.

In the forefront of emerging display technologies are displays based on the concept of field emission. Field emission is a concept dating back to 1928, and may prove to be the basis for displays that consume far less power than conventional plasma displays while still offering wide viewing angles, unlike the liquid-crystal displays common in laptops, televisions, and small hand held video devices. In "Watching the Nanotube," Gehan Amaratunga [2] notes that a 38-inch color cathode ray tube (CRT) display consumes approximately 70 W, while a similarly sized plasma display consumes approximately 700 W. Although the power consumption of a 38-inch plasma display has fallen to about 350 W in the past 2 years, its power consumption implies that if plasma technology were to become more commonplace, there would be significant implications for electricity generation and distribution. Amaratunga also notes that a 38-inch field emission display is predicted to be able to provide the same performance as a plasma display while consuming only 50 to 70 W [2].

Field emission displays use much less power than plasma displays because their intrinsic operation is far more efficient. Plasma displays generate visible light in a multi-step process: a gas is ionized, which in turn emits ultraviolet light that further stimulates a phosphor to produce visible light [2]. Field emission inherently does away with the high energy ionization step, and stimulates the phosphor directly with electrons.

With the field emission process having been adequately understood since the mid 20th century, one may question why the process has not already been capitalized upon for display technologies. The answer is simply that until recently, the technology to make suitable field emission tips has not been available. The technological capabilities of the past failed to provide adequate field emission materials and micro-processing capabilities.

The key element of the field emission display is the field emission cathode. The field emission cathode is the source of the quantum tunneling phenomenon that drives field emission. In its simplest description, field emission functions not by heating the cathode to 'boil off' electrons *over* a potential barrier as in a conventional CRT, but by emitting electrons *through* a 'thinned' potential barrier.

The primary drawback with field emission displays is that the field emission cathode experiences high temperature conditions during operation. In the past, cathodes have been made of various metals in the form of tiny cones; the devices, however, routinely fail during operation because the emission tips become so hot they melt. The melting of the emission tips causes deformations that damage the geometric characteristics needed for field emission. Moreover, because a metal's resistivity increases with increased temperature, a process known as thermal runaway is

characteristic of metal-cathode field emission devices. Thermal runaway is a feedback cycle where a metal's resistivity increases with increased temperature, and its increased resistance levels ultimately produces more heat, causing a damaging feedback loop.

The ideal material for a field emission device is therefore one that: conducts electricity with virtually no resistance; can be micro-machined into micrometer or nanometer scale tips; does not exhibit a resistive heating feedback cycle; and can withstand high temperatures without deforming.

With the discovery of CNTs in 1991 by Sumio Ijima [3], the ideal field emission material appears to have been found.

1.2 Summary of Current Knowledge

1.2.1 Carbon Nanotubes

The most prominent characteristic of CNTs is simply their size, as they typically have diameters ranging from 1 to 50 nm and lengths of several micrometers [4]. This large length to radius ratio makes CNTs nearly one dimensional, where operating characteristics are driven heavily by quantum mechanics. Additionally, because CNTs are held together by strong carbon-to-carbon bonds, they have an extremely high mechanical stability and chemical inertness. The electrical properties of CNTs are even more promising, as theoretical predictions show that CNTs can conduct electricity with virtually no resistance.

There are several methods to grow CNTs, each resulting in different purity, size, shape, and number of 'walls'. During the past decade, many research studies have focused on characterizing various preparation methods. The three primary methods used

in preparing CNTs include: electric arc discharge; laser ablation; and chemical vapor deposition (CVD). In most all of the derivatives of these three techniques, a metal catalyst (typically Co, Fe, and/or Ni) in the form of nano-particles (particle radius as small as 10 nm) is used ([5], [6]).

One typical problem encountered during catalyst-driven synthesis is that there is an unwanted presence of metal catalyst particles in the CNT product. The metal-catalyst particles contaminate the CNT product, thereby altering the characteristic properties of the CNT [7]. The catalyst residue and impurities have to be removed from the CNTs before experimental characterization. The removal of the unwanted particles from the CNT is difficult, costly, time consuming, and usually damages the CNTs ([5], [8]).

Further information regarding the properties of CNTs is found in Appendix A.

1.2.2 Field Emission

Field emission is a unique quantum-mechanical effect of electrons tunneling from a condensed matter into a vacuum. The process occurs in the presence of high electric fields, typically on the order of $10^7 – 10^8$ V/cm for planar metal surfaces [9]. In order to produce such high electric fields using reasonable potentials, the emitter is typically formed into a tip with an apex radius of curvature ranging from tens of angstroms to several micrometers, making the use of CNTs as field emission cathodes ideal. The high electric field induces field emission by narrowing the potential barrier at the metal-vacuum interface sufficiently for electrons to have a high probability of tunneling from the solid into the vacuum. An overview of this potential barrier narrowing phenomena is given by Figure 1. In Figure 1, as the applied voltage between the cathode and anode is

increased (thereby increasing the electric field strength) as given in the configuration shown in Figure 3(a), the negative slope of the potential barrier will increase, becoming narrower. This narrowing phenomena, including descriptions of the work function, ϕ, and effective work function, ϕ_{eff}, is discussed in Chapter 2.

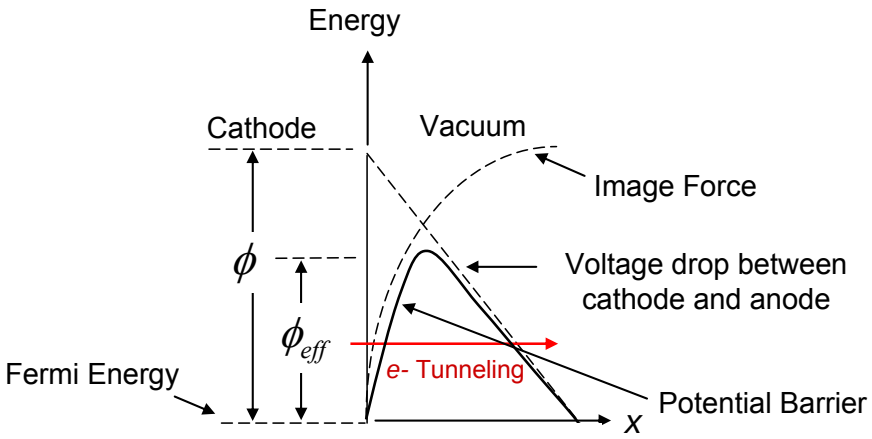

Figure 1. Illustration of the idealized energy barrier at the cathode-vacuum interface resulting from an applied voltage between the anode and cathode as given in Figure 3(a) and image forces, after [10]. Here *x* indicates the distance from the cathode to the anode.

The quantitative description of field emission is known as Fowler-Nordheim (F-N) theory, relating the emission current density to the applied electric field. Great amounts of research have been conducted since the introduction of F-N theory to characterize the field emission characteristics of various geometries and dimensions of field emitters. First published in 1928, F-N theory was originally developed to describe the field emission process from metallic materials [11]. Over the past several decades, this theory has been expanded and adapted to describe the field emission process from various semiconductor materials.

The material properties of CNTs make them potentially extraordinary field emission sources [12]. Their high conductivity, high aspect ratio, nanoscale diameters, and whisker-like shape support this claim. A multi-walled CNT emitter can be heated by its field-emitted current up to 2000 K and remain stable [12]. This characteristic is distinctively different from metal emitters which fail due to thermal runaway.

A current literature review reveals that several research groups are investigating the use of CNTs as field emission devices. Tests have been performed on various orientations of CNTs grown on different substrates and in varied patterns through the use of metal-catalyzed fabrication methods.

1.3 Scope

Research by the Air Force Research Laboratory's Materials and Manufacturing Directorate (AFRL/MLPS) has shown that vertically aligned CNT films form on both the silicon and carbon faces of silicon carbide wafers at high temperatures (approximately 1700^{o}C) through the decomposition of silicon carbide substrates. Most notably, this growth method occurs without the use of catalyst metals, yielding CNTs that are potentially of greater purity than CNTs grown using catalyst metals [13].

The CNT's properties are derived from its homogeneous lattice structure, made entirely of carbon atoms, as Figure 2 illustrates. When impurities are present (such as catalyst metal particles), the CNT's electrical and mechanical properties are altered [7].

AFRL/MLPS's plans involve studying the electrical properties of the CNT films grown using this novel catalyst-free manner on SiC. Potential applications include their use as anodes or cathodes for high power microwave systems, or as chemical sensors for

use in homeland defense. This thesis focused on demonstrating the use of the CNT films grown using the SiC decomposition method in field emission devices. AFRL/MLPS's interest in this topic is based on the goal of further characterizing the properties of CNT films fabricated in this manner, capitalizing on the perceived benefits of catalyst-free growth, and the high thermal conductivity of SiC.

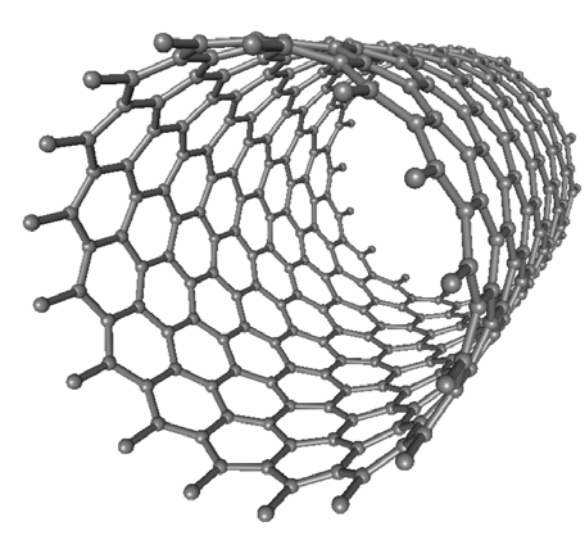

Figure 2. Illustration of the single-walled CNT structure [14].

Vacuum tests were used to investigate the field emission characteristics of the CNT films grown in the manner used by AFRL/MLPS. The threshold and turn-on electric fields, along with the maximum achievable current density for CNT films grown, were measured and compared to one another in an effort to determine the optimal growth parameters for an emission surface. The CNT growth times and vacuum pressures were varied, and the tips of the CNTs were opened, in an attempt to determine the most optimal growth conditions to obtain the most effective emission surface. Scanning

electron microscopy (SEM), transmission electron microscopy (TEM), and atomic force microscopy (AFM) were used to characterize the surface properties of the CNT films.

1.4 Approach

The CNT films' field emission properties was characterized by creating an experimental test apparatus and collecting data relating the applied voltage to the observed emission current. With the recorded field emission current as a function of applied electric field, the field enhancement factor was calculated to characterize the CNT emission surface and compare it to other field emitters found in the literature. In addition, the stability of the CNT films' emission current was recorded over finite lengths of time (15-second intervals). The experimental setup used is illustrated in Figure 3 (a) and (b), with the vacuum chamber operated in the mid 10^{-7} Torr range.

1.5 Main Results

Although the samples fabricated and tested did not demonstrate improved field emission characteristics when compared to values found in the literature, the data collected show that further investigation is warranted regarding the emission capabilities of CNT films grown on SiC substrates by surface decomposition. From the collected data, the lowest turn-on electric field was found to be lower than 3.0 V/μm, while exhibiting a high maximum current density of 4.25 mA/cm^2 at 6.7 V/μm; these values are found to be well within values found in current literature.

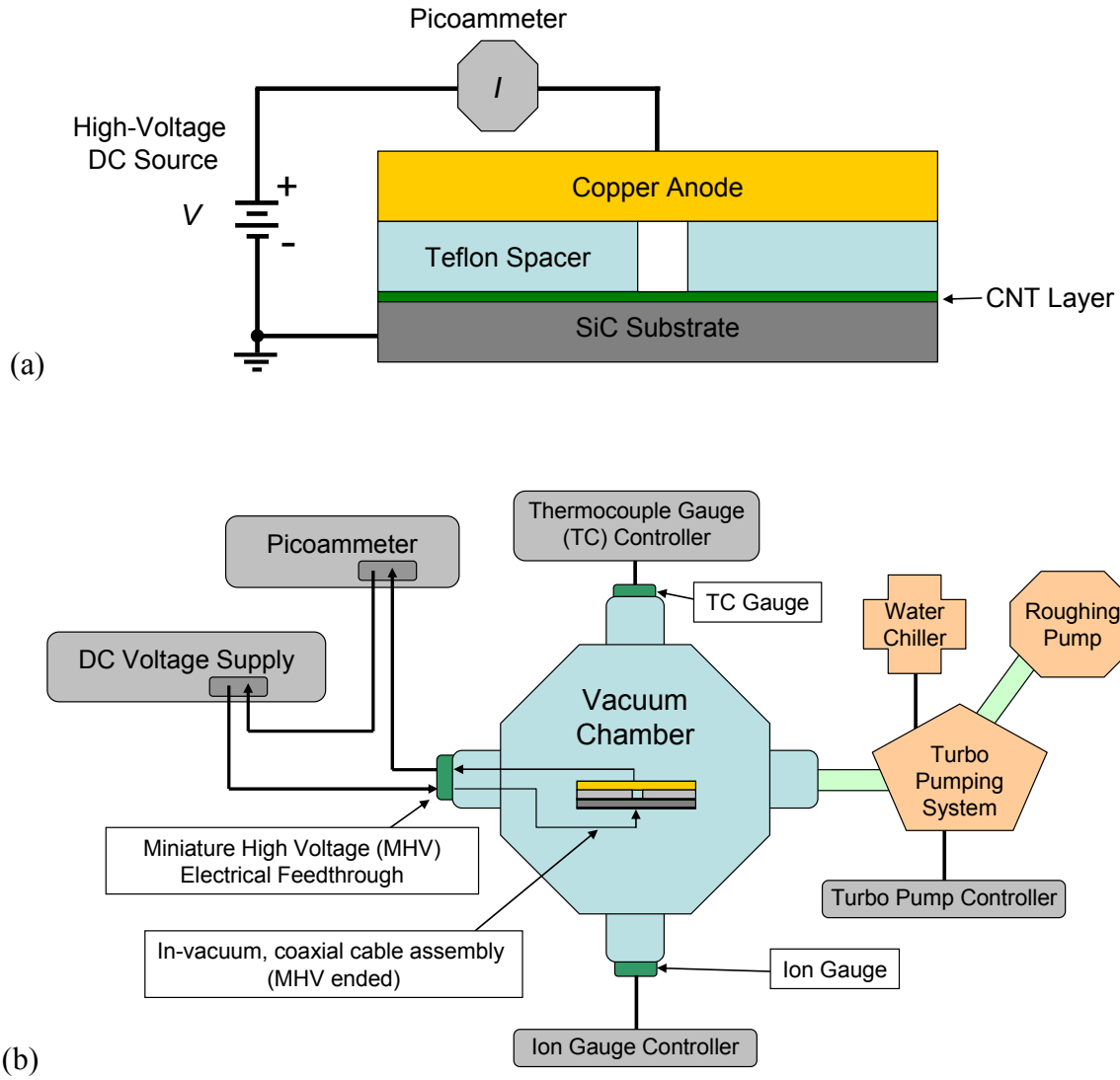

Figure 3. Illustrations of the: (a) vacuum tube diode test setup, and (b) overall test setup.

Chapter 2: Literature & Theory Review

This chapter discusses the field emission process, CNT field emission studies found in the current literature, and the formation of CNTs on silicon carbide substrates by surface decomposition.

2.1 Field Emission Background

When an electric field on the order of 10^7 V/cm is applied to a solid surface with the negative electrical potential on the solid and a positive (anode) potential near the solid surface, electrons inside the solid are emitted into the vacuum toward the anode via quantum mechanical tunneling ([9], [15]). The strong electric fields necessary for field emission can be attained on the tips of very thin needles, as electric fields concentrate at sharp points [15]. High electric fields induce the field emission of electrons by sufficiently narrowing the potential barrier at the metal-vacuum interface for electrons to have a high probability of tunneling from the solid into the vacuum.

An overview of this potential barrier narrowing phenomenon is given by Figure 4. Figure 4(a) illustrates the ideal potential barrier at the cathode to vacuum interface for the case of zero applied voltage to the anode. Figure 4(b) illustrates the potential barrier due to image forces (described later in this section). Figure 4(c) illustrates the potential barrier due to an applied voltage at the anode as shown in Figure 5. The conditions illustrated in Figure 4(c) suggest that as the voltage is increased (increasing the electric field strength), the potential barrier becomes more and more narrow. Figure 4(d) shows the total potential barrier as a summation of the effects given in Figure 4 (a) through (c). Further detail regarding image forces and applied voltages is given in section 2.2.

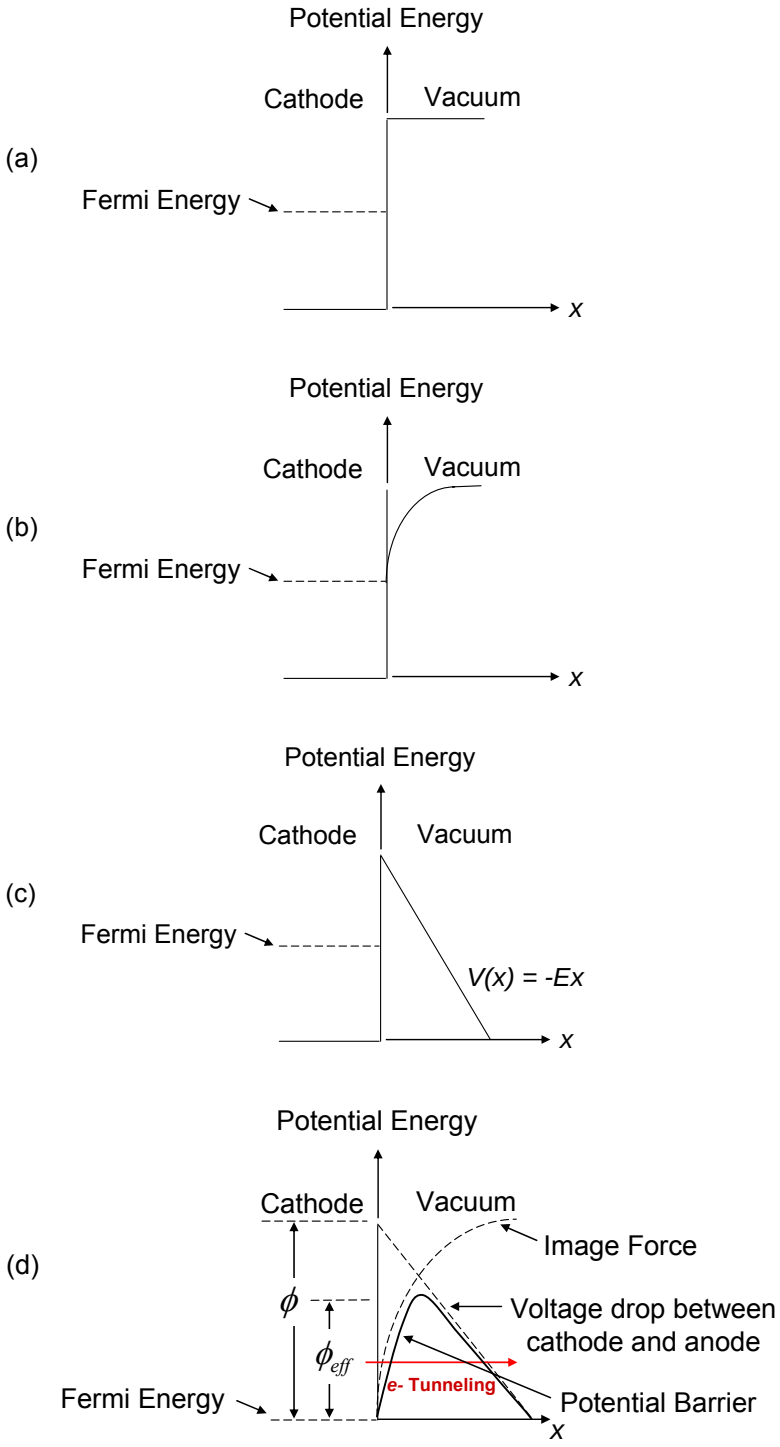

Figure 4. Illustration of the idealized energy barrier at the cathode-vacuum interface under (a) ideal conditions with bias applied, (b) image forces, (c) an applied voltage, and (d) the superposition of barrier effects, after [10]. Here *x* indicates the distance from the cathode to the anode.

Field emission, also commonly referred to as cold cathode emission, contrasts with thermionic emission. In thermionic emission, electron emission occurs *over* the potential barrier rather than *through* it. Thermionic emission occurs from a solid to vacuum at extremely high temperatures and low electric fields [9].

An illustration of the vacuum tube diode field emission test setup is given in Figure 5, where d is the distance between the anode and cathode, V is the voltage applied between the anode and cathode, I is the current flowing through the diode, and the film is the field emission tip material or geometric shape under investigation.

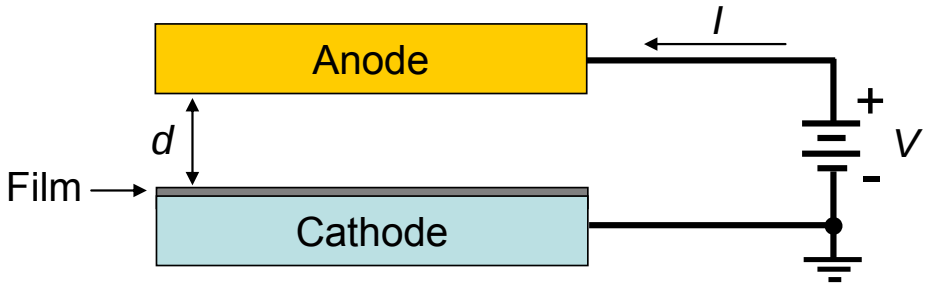

Figure 5. Illustration of the vacuum tube diode field emission test setup, after [16].

2.1.1 Fowler-Nordheim Theory Overview

Fowler-Nordheim (F-N) theory is based on six assumptions. The first assumption states that the metal emission surface obeys the Sommerfeld free electron model with Fermi-Dirac statistics [10]. The basic premise of the Sommerfeld free electron model states that electrons inside the metal are entirely free to roam around, but are unable to leave the metal [10]. The electrons inside the metal are effectively bound by an infinite potential barrier, and the potential energy level of electrons inside the metal is uniform. Fermi-Dirac statistics describe the probability of occupation of an energy state within the metal.

The second assumption states that the metal emission surface is taken to be planar, yielding a one-dimensional situation [9]. Next, F-N theory assumes that the potential within the metal is considered constant. An externally applied electric field is assumed to have no effect on the electron states inside the metal [9]. The next assumption states that, according to the laws of electrostatics, the forces acting on an electron in front of an infinitely conducting sheet are given by replacing the sheet with a 'mirror' charge, which is described as a positively-charged particle the same distance behind the sheet [10]. The force between these two charges is known as the image force, given by [10]

$$F(x) = \frac{e^2}{4\pi\varepsilon_o}\frac{1}{(2x)^2} \tag{2.1}$$

where F is force (Newtons), ε_o is the permittivity of free space (8.854 x 10^{-12} Farads/m), e is the elementary electron charge (1.602 x 10^{-19} Coulombs), and x is the distance from the infinitely large conducting sheet (m). The value of $1/(4\pi\varepsilon_o)$ is equal to $9.0\times10^9\ N\ m^2/C^2$.

The potential energy is the integral of this force from the point x to infinity, and is given by [10]

$$U(x) = \int_x^\infty F(y)dy = -\frac{e^2}{16\pi\varepsilon_o x} \tag{2.2}$$

where U is the potential energy (V), and y is the variable of integration. The F-N calculation is assumed to be performed at the temperature T = 0 K, indicating that the majority of the cathode's free electrons reside at the metal's Fermi level [9]. Lastly, F-N

theory assumes that the electric field between the anode and cathode (E) is constant. The potential due to the applied anode voltage in the vacuum region is therefore given by

$$U(x) = -eEx \tag{2.3}$$

where E is the applied electric field strength in Volts per meter (V/m), and x is the distance from the cathode in meters. Note that script E is the applied electric field strength (V/m), and non-script E is energy.

Taking into account the electric field and the image forces, the potentials can be added to yield the potential barrier as given by Figure 4 (d). The maximum potential barrier present near the metal-vacuum interface can be calculated under the condition given by [9]

$$\frac{d}{dx}\left(-\frac{e^2}{16\pi\varepsilon_o x} - eEx\right) = 0 \tag{2.4}$$

Solving equation (2.4) leads to the value for the maximum potential of the barrier, given by equation (2.5). The energy needed to escape from the metal cathode is reduced by $|V_{max}|$.

$$U_{\max} = -e\left(\frac{eE}{4\pi\varepsilon_o}\right)^{1/2} \tag{2.5}$$

The effective work function, ϕ_{eff}, of the metal cathode is thus reduced from ϕ to that given by equation (2.6), and is illustrated in Figure 4 (d), which shows the total potential at the metal-vacuum interface due to an applied voltage and image forces.

$$\phi_{eff} = \phi - e\left(\frac{eE}{4\pi\varepsilon_o}\right)^{1/2} \tag{2.6}$$

Figure 4 (d) illustrates the case where the presence of an electric field may increase the emission current because more electrons are likely to escape *over* the reduced barrier (note that Figure 4 (d) is not to scale in regards to the work function, effective work function, and potential barrier width). This is not the driver of field emission, as the dominant source of emitted electrons is *through* the barrier as opposed to *over* the barrier. At T = 0 K (a given assumption of F-N theory), the metal's electrons are located at its Fermi level. The field emission process occurs practically independent of temperature. The application of a high voltage between the cathode and anode results in the potential barrier of Figure 4 (d) becoming narrower and facilitating the electron tunneling process.

To derive a theoretical formula for field emission, the tunneling probability of the electrons moving towards the surface is calculated. From the shape of the potential barrier, given by Figure 4 (d), it follows that electrons with higher energy can more easily tunnel through the barrier. At low temperatures, however, there are few of such higher-energy electrons, causing the tunneling current to originate from electrons near the Fermi level. The width of the potential barrier can be calculated by solving for the barrier width at the Fermi level, x_F, in equation (2.7) and the barrier height the electrons face is taken to be ϕ_{eff} [10].

$$-\phi = -eEx_F \tag{2.7}$$

The tunneling current can be approximated by equation (2.8). Substituting equation (2.7) into equation (2.8), the relationship given by equation (2.9) is found [10]. The exponential factor given by equation (2.9) is a strong approximation to the exact

formula, which is described in the next section. Equation (2.9) is the central equation of F-N theory, relating emission current density to the applied electric field.

$$J \approx \exp\left[-\frac{(2m\phi_{eff})^{1/2}}{\hbar} x_F\right] \tag{2.8}$$

where J is the tunneling current density, $\hbar$ is the reduced Planck's constant (given by $h/2\pi$), and m is the free electron mass (9.11×10^{-31} kg).

$$J \approx \exp\left[-\frac{(2m)^{1/2}}{\hbar e}\frac{\phi_{eff}^{1/2}\phi}{E}\right] \tag{2.9}$$

2.1.2 A Detailed Look at Fowler-Nordheim Theory

To calculate the emission current, F-N theory begins by determining the barrier transparency, D, and the flow, n, of electrons incident on the barrier from within the metal. Next, both D and n are integrated over the electron energy on which they are both dependent [9], [17]. Under the assumptions given in the previous section, the current density is given by [17]

$$\mathrm{J} = \mathrm{e}\int_0^\infty n(\mathrm{E}_x)D(\mathrm{E}_x, F)d\mathrm{E}_x\,, \tag{2.10}$$

where e is the electron charge, $n(\mathrm{E}_x)$ is the number of electrons per second having energies between E_x and $\mathrm{E}_x + d\mathrm{E}_x$ and incident on 1 cm^2 of the barrier surface from within the metal. The term $n(\mathrm{E}_x)$ is quantitatively based on Fermi-Dirac statistics. The term E_x is calculated by

$$\mathrm{E}_x = \frac{p_x^{\,2}}{2m}, \tag{2.11}$$

where E_x is the part of the electron kinetic energy carried by the momentum component p_x normal to the surface, m is the free electron rest mass, and E is the applied electric field [9].

The barrier transparency is calculated using the semi-classical method of the Wentzel-Kramers-Brillouin (WKB) approximation [9]. The WKB approximation is a special technique for obtaining an approximation to the solution of the one-dimensional time-independent Schrödinger equation, valid when the wavelength of the solution varies slowly with position. With an applied electric field, E, the potential function is given by

$$U(x) = -\frac{e^2}{16\pi\varepsilon_o x} - eEx. \tag{2.12}$$

An illustration of the potential energy of an electron as a function of the distance x from a metal surface is given in Figure 6, showing the total potential barrier, and the barriers resulting from the image force, and the external applied potential. In the figure, U_p is the potential well depth in the metal, and ϕ is the work function of the metal.

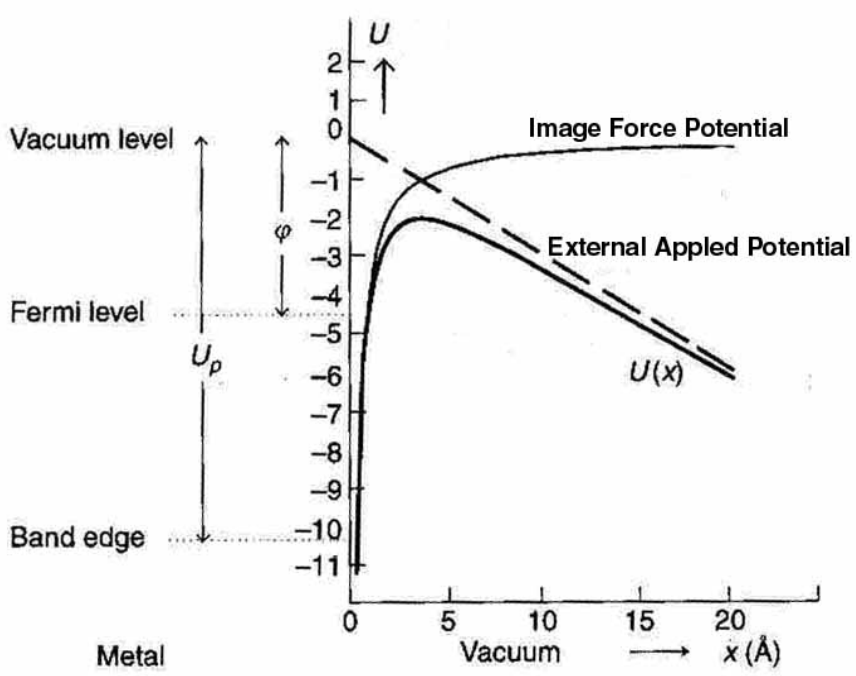

Figure 6. Barrier at the metal-vacuum interface showing the electron potential energy, *U(x)* (in eV), as a function of the distance *x* from the metal surface [9].

Derivations by Fursey *et al.* [9] show that the transparency is given by

$$D(\mathrm{E}_x, E) = \exp\left[\frac{-8\pi(2m)^{1/2}}{3he}\right]\frac{\left|\mathrm{E}_x^{3/2}\right|}{E}\varphi(y) \tag{2.13}$$

where h is Planck's constant, e is the elementary electron charge, m is the free electron rest mass, E_x is a given energy level, E is the electric field strength, and $\varphi(y)$ is the Nordheim function given by [9], [17]

$$\varphi(y) = 2^{1/2}\left[1+(1-y^2)^{1/2}\right]^{1/2}\left[E(k)-[1-(1-y^2)^{1/2}]\right]K(k)\,. \tag{2.14}$$

In equation (2.14),

$$y = \frac{(e^3E)^{1/2}}{\phi} \tag{2.15}$$

Equation (2.14) is further dissected such that [9], [17]

$$\mathrm{E}(k) = \int_0^{\frac{\pi}{2}} \frac{d\alpha}{(1-k^2\sin^2\alpha)^{1/2}}, \tag{2.16}$$

and

$$K(k) = \int_0^{\frac{\pi}{2}} (1-k^2\sin^2\alpha)^{\frac{1}{2}} d\alpha \tag{2.17}$$

are complete elliptic integrals of the first and second kinds, and

$$k^2 = \frac{2(1-y^2)^{1/2}}{1+(1-y^2)^{1/2}}. \tag{2.18}$$

Using equation (2.10), the field emission current density at T = 0 K follows the model given by [9]

$$J = \frac{e^3}{8\pi h}\frac{E^2}{t^2(y)\phi}\left[-6.83\cdot 10^7 \frac{\phi^{3/2}}{E}\varphi(y)\right] \tag{2.19}$$

Substituting the values of constants and expressing ϕ in eV, F in V/cm, and J in A/cm^2 yields another form of the central F-N theory equation [9]:

$$J = 1.54\cdot 10^6 \frac{E^2}{t^2(y)\phi}\left[-6.83\cdot 10^7 \frac{\phi^{3/2}}{E}\varphi(y)\right] \tag{2.20}$$

where $y = (3.79\times 10^{-4})\times\left(\sqrt{E}\right)/\phi$, and $t(y)$ is $\varphi(y) - (2y/3)(d\varphi(y)/dy)$. The terms $\varphi(y)$ and t(y) are tabulated and can be referenced in the literature [9]. Because $t(y)$ is often close to unity and varies weakly with y, it is commonly set to unity [9]. The Nordheim function $\varphi(y)$ varies significantly with y [9].

2.1.3 Deviations from Theory Due to Nanometer-Scale Emitter Tips

F-N theory gives a fair description of the field emission process for atomically smooth emitters having a radius greater than 0.1 μm [9]. In this case, the width of the

potential barrier is significantly less than the cathode's radius of curvature. Additionally, atomic-scale surface roughness and variations of the work function between different emitter faces do not result in a significant deviation from the results obtained with the one-dimensional approximation [9].

As the radii of cathodes used enter the nanometer range, deviations from F-N theory emerge as the field emitter's radius of curvature begins to approach the cathode's potential barrier width. Emitter radii in the nanometer range negate the assumption of a one-dimensional barrier and field uniformity over the apex of the tip, requiring the three-dimensional Schrödinger equation to be solved in order to calculate the behavior of the potential near the surface accounting for its variation with radius, r_e [9].

An in-depth analysis of the effects of non-planar abnormalities on field emission surfaces is made by Forbes *et al.* [18]. In their work, Forbes *et al.* describe what is known as the field enhancement factor, γ, (also given as β by some sources), which is given by

$$\gamma = E / E_M . \tag{2.21}$$

Forbes *et al.* describe the field enhancement factor in the following way [18]:

> In geometrical configurations resembling a parallel-plate capacitor, the macroscopic field, E_M, is defined by: $E_M = V/d$, where V is the voltage applied across a gap of thickness d. The local field E is the field close to the emitting surface (within 1-2 nm of the surface atoms) that determines the barrier through which field-emitted electrons tunnel. This field E is sometimes called the barrier field. E is typically a few *V/nm*, and is often significantly higher than E_M. Their ratio defines a field-enhancement factor γ, $\gamma = E/E_M$.

The geometrical models for a field-enhancing micro- or nano-protrusion, as presented by Forbes *et al.,* are illustrated in Figure 7 and include: a) hemisphere on a plane, b) floating sphere at emitter-plane potential, c) hemisphere on a post, and d) hemi-

ellipsoid on a plane. In the diagram, ρ is taken to be the sphere or hemisphere radius [18].

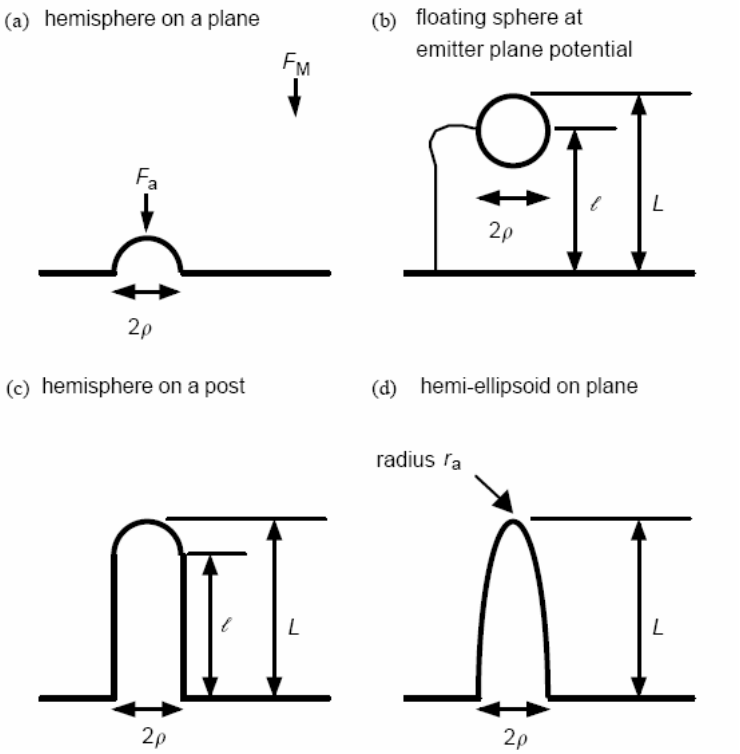

Figure 7. Geometrical models for a field-enhancing micro/nano-protrusion [18].

2.2 Field Emission from Carbon Nanotubes

The material properties of CNTs make them potentially extraordinary field emission sources [12]. Their high conductivity, high aspect ratio, nanoscale diameters, and whisker-like shape support this claim. For an in-depth review of the electrical and mechanical properties of CNTs, along with information regarding the common fabrication methods of CNTs, please refer to Appendix A.

CNTs are robust emitters in vacuum, even at high temperatures. A multi-walled CNT emitter can be heated by its field-emitted current up to 2000 K and remain stable

[12]. This characteristic is distinctively different from metal emitters which fail due to thermal runaway. In metals, resistance increases with temperature, meaning that more heat is produced as higher current is drawn. The combination of high temperature and electric field causes field sharpening of the emitter tips by surface diffusion, which in turn increases the local field, current, and temperature. This positive feedback mechanism causes unstable thermal runaway which leads to emitter failure for metal-based emitters. The resistance of a CNT, in contrast, decreases with an increase in temperature which limits heat generation. Surface diffusion and electromigration is less likely in the strong carbon to carbon covalent bonds of the CNT [12].

Although one would think that single-wall CNTs would be the emitter of choice due to their small diameter, multi-walled tubes are usually used in field emission applications because they are semi-metallic, more robust, and are stiffer. For field emission applications, vertically aligned CNTs, rather than randomly oriented CNTs, are desired because the tips of the CNTs in the vertically-aligned orientation are exposed to the applied electric field and thus work more efficiently as the emitting tip. Moreover, for applications requiring high emission currents, it is necessary to space the emitters twice their height apart from one another to eliminate electric field screening effects between adjacent CNT emitters [12].

CNT field emission deviates from the F-N model, as CNTs cannot be considered usual metallic emitters. This deviation typically results in slope changes of the characteristic F-N plot [19]. The deviations from the F-N model are attributed to space-charge effects [1]. Space-charge is defined as the electrostatic interaction of electrons in the emitted beam. The field created by the high density of negatively charged electrons

effectively screens the cathode from the accelerating field of the positively charged anode; once a limiting density is reached, no further electrons can be added to the beam.

A difference exists in the emission properties of closed and opened multi-walled CNTs. Opened tubes are far less efficient emitters than closed ones, with the voltage needed to obtain the same emission current density typically twice that of closed tubes (proven experimentally by [1]). This is an interesting finding due to the smaller effective curvature of opened CNTs. It is believed that foreign atoms (such as oxygen) are attracted to the free dangling bonds at the ends of the opened CNTs, resulting in localized electron states. Since these states lie well below the Fermi energy of the CNT, electrons are less likely to be emitted. Conversely, experimental work to condition the CNT field emission tips and cause the desorption of foreign atoms, has shown that opened CNTs provide the most favorable current-voltage relationship [16].

2.2.1 Carbon Nanotube Field Emission Tests

The following section discusses results and observations from the testing of CNT films used as field emission sources found in current literature.

In [20], Li *et al.* discussed the growth of a CNT film on a test substrate for use as a field emission source. Their experimental work concluded that CNTs films make strong candidates for field emission sources, as the films demonstrated low turn-on electric fields, a uniform and high emission current density, and good emission stability.

The CNT test apparatus used by Li *et al.* is shown in Figure 8. The anode consisted of an indium-tin-oxide (ITO) glass plate coated with phosphor. A 200 nm thick layer of aluminum was coated on the red phosphor layer in order to protect the phosphor

layer, as well as to aid in removing accumulating charge. A 75 μm thick insulating layer was inserted between the anode and cathode. The cathode and anode were then encapsulated in cylindrical glass vacuum tube. Getters (desiccant material) were mounted within the evacuated glass tube to absorb possible out-gassing. The emission current density was measured by a Tektronix TX3 multi-meter connected to a computer.

The CNTs used in Li *et al.'s* testing were multi-walled with inner and outer diameters of 20 to 100 nm, respectively. The CNT lengths were about 1-2 μm [20]. Their experimental method consisted of taking measurements of the current density versus the applied electric field by applying a voltage to the anode at a vacuum of 4×10^{-7} Torr. Figure 9 shows their recorded emission current density plotted versus electric field strength. Figure 10 shows the F-N representation of the experimental data, which is given by plotting $\ln(I/V^2)$ versus $1/V$.

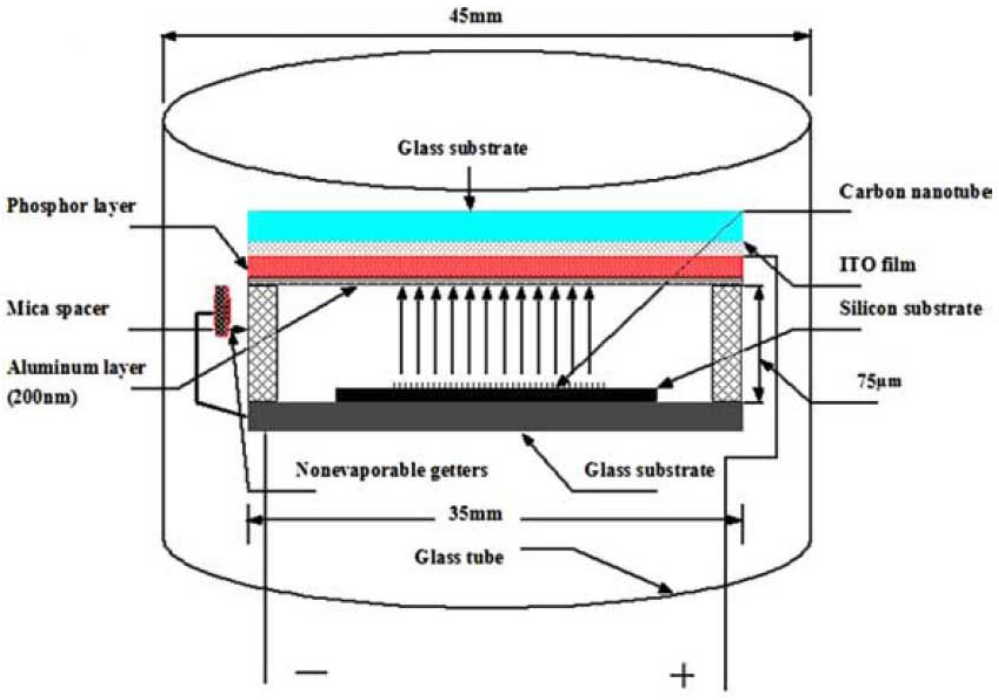

Figure 8. Schematic of Li *et al.*'s field emission test setup [20].

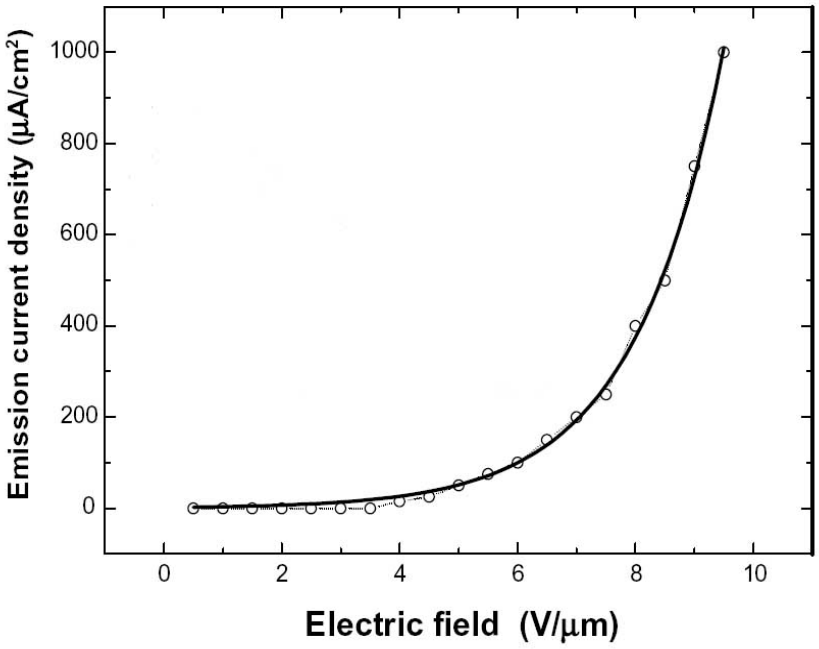

Figure 9. Plotted current density vs. electric field data collected during Li and coworkers' field emission testing [20].

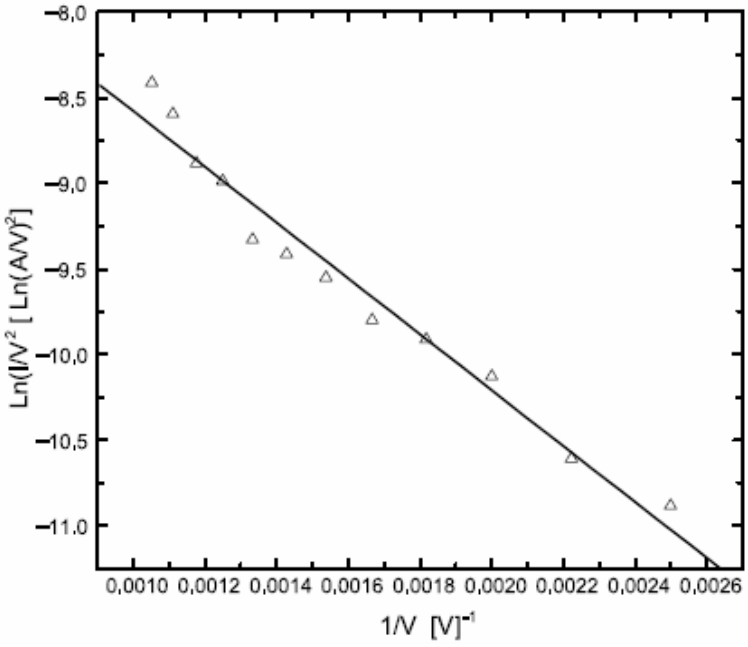

Figure 10. The corresponding Fowler-Nordheim plot of the field emission data plotted in Figure 9, indicating a conventional field emission trend [20].

A recordable emission current started at an electric field of 4 V/μm, and the emission current density approached 1 mA/cm^2 at an electric field of 9.5 V/μm. The linear relationship of the F-N curve in Figure 10 shows that the measured current was the result of field emission according to F-N theory. Further analysis of the experimental data allowed for the calculation of the field enhancement factor, β (also denoted by γ in some sources).

To calculate the field enhancement factor, β, Li *et al.* used the F-N formula given in equation (2.22) [20]. The constants introduced in equation (2.23) are defined in equations (2.23), (2.24), and (2.25) [20]. For equations (2.23) and (2.24), β' is defined as the local field conversion factor at the emitting surface, $B = 6.87 \times 10^7$, ϕ is the CNT work function and is approximately 4.5 eV, and d is the distance between the anode and cathode in cm. Combining equations (2.23) through (2.25) and knowing that the parameter b is given by the slope of the plot in Figure 10, the electric field enhancement factor is calculated using equation (2.26). Based on their collected data and the equations given, Li *et al.* calculated the enhancement factor to be 4,012 [20].

$$I \approx aV^2 \exp(\frac{-b}{V}) \tag{2.22}$$

$$E_{loc} = V\beta' \tag{2.23}$$

$$b = \frac{0.95B\phi^{3/2}}{\beta'} \tag{2.24}$$

$$E_{loc} = \frac{\beta V}{d} \tag{2.25}$$

$$\beta = \frac{0.95B\phi^{3/2}d}{b} \tag{2.26}$$

Figure 11 shows the emission current density as a function of time for an applied electric field of 9 V/ μm [20]. The average fluctuation of the emission current density was less than 5%, indicating an extremely stable emission process.

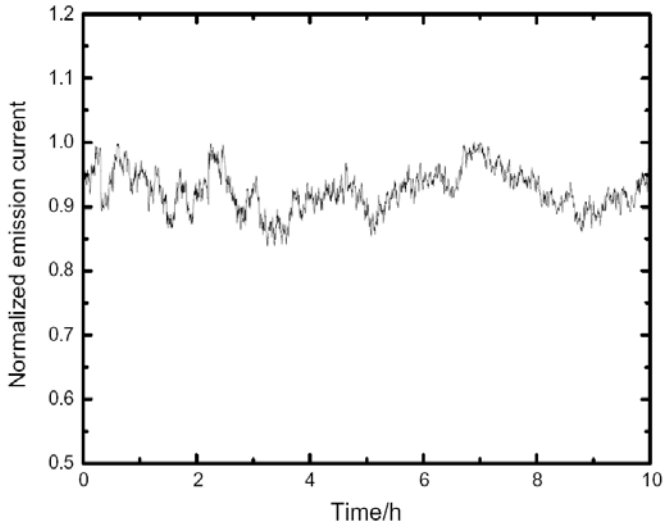

Figure 11. Normalized current fluctuation over time at 9 V/μm applied electric field collected by Li *et al.* during field emission testing [20]. Here time is given in hours, not per hours as indicated by the figure.

Manohara *et al.* [19] discuss results and observations from the testing of single-walled and multi-walled CNTs as field-emission sources. One basic conclusion was that high density CNT films suffered from enhanced screening effects, causing a decreased field emission current. Their experimental results showed that the highest emission currents were measured from disordered and less dense multi-walled CNT films.

The single-walled CNT films tested by Manohara *et al.* were grown by chemical vapor deposition (CVD) with methane as the feed gas. CNT growth specifics included using iron nitrate in an isopropanol solution as the catalyst metal, which was spun onto

silicon substrates. Multi-walled CNTs were grown through a plasma-enhanced CVD process on patterned silicon and silicon dioxide substrates at temperatures below 600^{o}C.

The field emission tests were conducted in the diode configuration, described by the setup in Figure 12 (right), as well as in Figure 5. The test template was fabricated on a 5 mm by 5 mm die of degenerately doped silicon substrate with an oxide layer approximately 1.5 µm. A 3 mm diameter trench 10 µm deep was then etched into the substrate. Using the photoresist from the previous etch step, the catalyst metal was selectively deposited inside the trench and CNTs were grown.

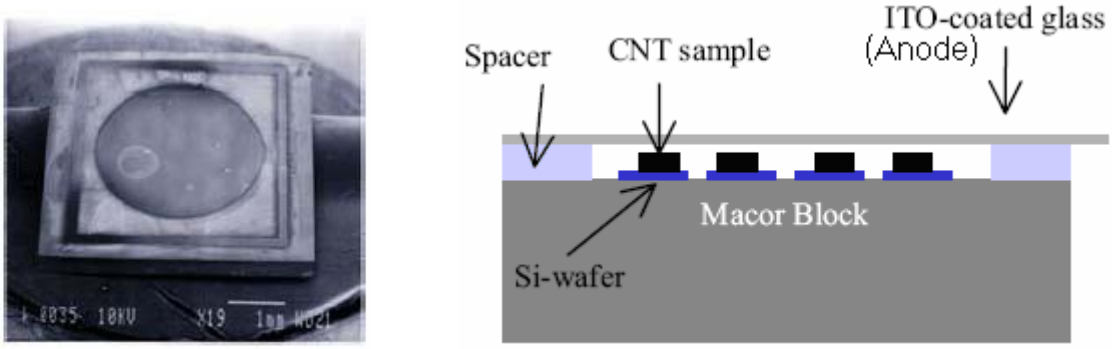

Figure 12. CNT sample template with 3 mm diameter trench (left), and a schematic of the measurement setup inside a high vacuum chamber (right) [19].

Testing involved using a transparent glass slide coated with ITO as the anode. The anode was also coated with blue-pigmented phosphor in order to identify the emission spots. The tests were conducted at vacuum levels in the range of 10^{-6} Torr. Manohara *et al.* note that one advantage of CNTs as field emitters is that they are robust and operate well in high vacuums unlike other field emission tips, which require ultra high vacuums (10^{-9} Torr) for successful operation [19]. The CNT sample template and a

schematic of the measurement setup inside a high vacuum chamber are illustrated in Figure 12 (left).

Manohara *et al.* [19] presented a numerical analysis of their test data similar to that used by Li *et al* [20]. Figures 13 and 14 their plotted results. The conventionally accepted concept is that if F-N plot shown in Figure 14 is linear, then the observed emission current is a result of field emission, as opposed to thermionic emission or other sources of pre-breakdown currents.

Manohara *et al.* [19] fit their experimental data to the F-N relationship given by equation (2.27), which is merely an algebraic manipulation of equation (2.22) used by Li *et al.* [20] in calculating the electric field enhancement factor from their experimental data. In equation (2.27), I represents the emission current in amperes, V represents the applied biasing voltage in volts, and a , and b are constants calculated by equations (2.28) and (2.29), respectively. In equations (2.27) and (2.29), β represents the field enhancement factor, A_e represents the actual emission area in cm^2, ϕ represents the CNT's work function in eV, and d is the gap between the anode and CNT tip in μm.

$$\ln(\frac{I}{V^2}) = \ln(a) - \frac{b}{V} \tag{2.27}$$

$$a = 1.54 \times 10^{-6} (\frac{\beta^2 A_e}{\phi \cdot d^2}) \tag{2.28}$$

$$b = 6.8 \times 10^{7} (\frac{\phi^{3/2} \cdot d}{\beta}) \tag{2.29}$$

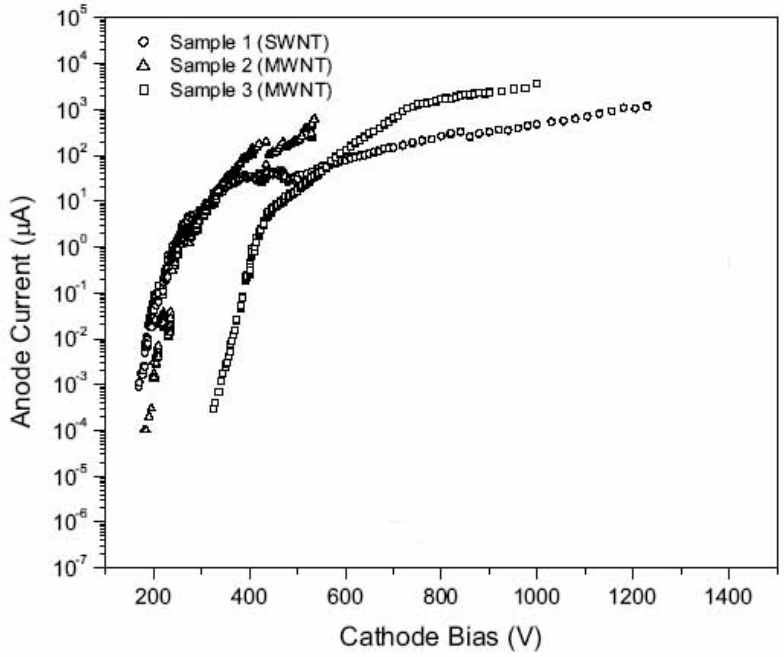

Figure 13. Plot of the measured field emission data given by Manohara *et al.* [19].

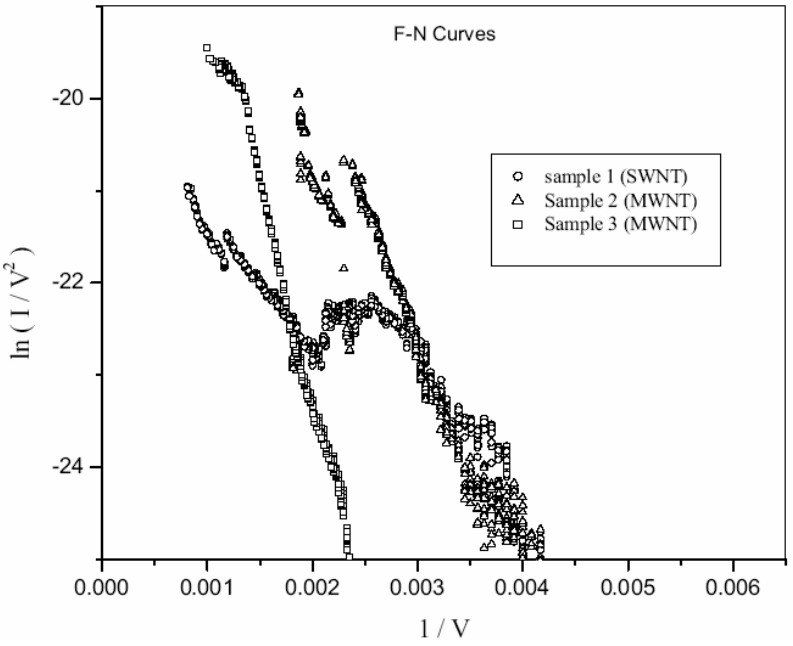

Figure 14. F-N plot of the measured field emission data from Manohara *et al.* [19].

The data plotted in Figure 14 can be represented by a line of the form $y = mx + c$. In the plot, $\ln(I/V^2)$ is plotted versus $1/V$ and is referred to as the characteristic F-N curve. As stated previously, linearity of this curve indicates that field emission is the dominant source of the observed current. By measuring the slope of the F-N line and its y-axis intercept, the constants b and a can be determined, respectively. Knowing the values of a and b, the actual emission area and the field enhancement factor can be determined using equations (2.28) and (2.29) [19].

Manohara *et al.* explain the lack of linearity in their F-N curve shown in Figure 14 by concluding the following: the field emission area contains CNTs of various sizes, which results in a range of threshold voltages for field emission as opposed to a single value; and that field emission is impacted by absorbed impurities which decrease the local work function, causing a lower threshold for field emission at various points in the emission area [19].

Based on the data plotted in Figure 14, Manohara *et al.* approximated the values of the a and b constants to be 1.98×10^{-6} and 5,257, respectively. Next, knowing that the separation d is approximately 160 μm, and the work function of the CNTs is approximately 4.5 eV, Manohara *et al.* calculated the effective emission area, A_e, to be 3.79×10^{-14} m^2. Based on this calculated emission area, they concluded that only 19 CNTs participated in field emission from one of their samples. This low number is concluded to be due to electrostatic screening, and is remarkable in that several billion CNTs are present within the sample's emission area. This low number also shows that there is great potential for much higher emission current densities if CNT growth can be efficiently controlled.

Additional conclusions by Manohara *et al.* were drawn from repeatability tests conducted on two samples to investigate how the emission current varied at a given voltage over a period of time and over different cycles. From their trials, they concluded "that the average value of emission current for a given field was influenced by the rate at which the field was attained [19]." Their data showed that by rapidly increasing the biasing voltage to its set point, the average emission decreased by 2 – 3%. The cause for this decrease was not known.

Lastly, Manohara *et al.* noted that under strong electric fields, the samples failed due to electric arcing and the resulting removal of the CNTs from the surface. Figure 15 shows the images Manohara *et al.* [19] provided of the surface damage, although the scale was not given.

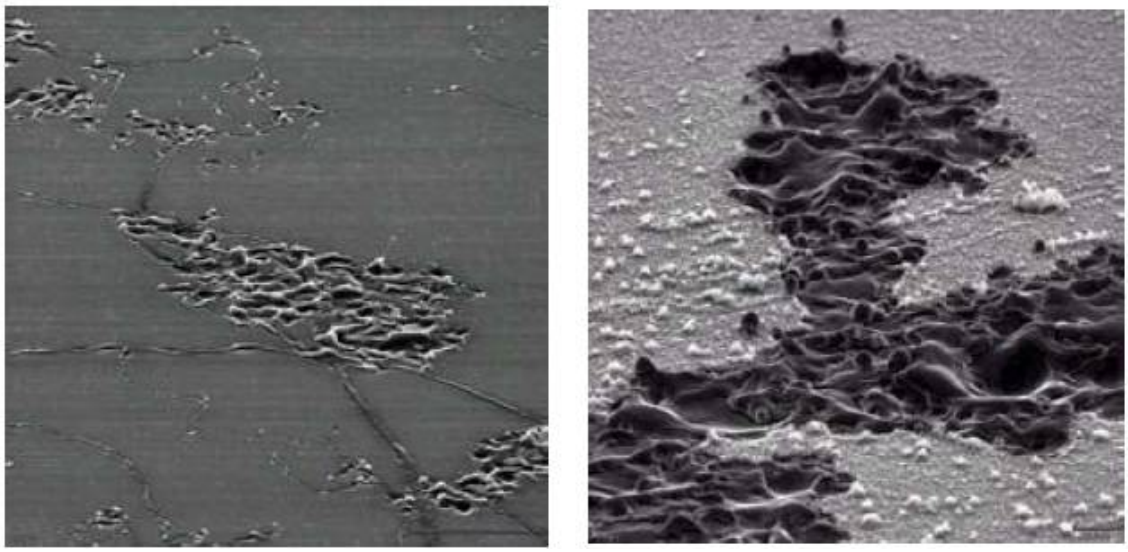

Figure 15. SEM images of a damaged CNT surface, purportedly due to arcing under high fields [19].

The analysis method used here to calculate the actual field emission area is not found in any other works in the literature. Due to this oddity, this method of data interpretation will not be implemented during the experimental phase of this thesis.

2.2.2 Experimental Field Emission Values from the Literature

To analyze the field emission characteristics of the samples tested, known values for field emitters found in the literature are necessary. Li *et al.* [20] reported a turn-on electric field of 4 V/μm, an emission current density of 1 mA/cm^2 at an electric field of 9.5 V/μm, and a field enhancement factor of 4012. Table 1 shows the turn-on electric fields, E_{to}, and threshold electric fields, E_{thr}, in V/μm for various film emitters given by Bonard *et al.* [1]. The non-CNT film emitter values given by Bonard *et al.* were collected from various works to show that their test results achieved turn-on and threshold current density levels at lower excitation fields. [1] notes that several of their values, identified with a superscript a ([a]), were extrapolated from lower current measurements and the true values may be either unattainable or much higher than the extrapolated value. Note that in the table the references given are the references used by [1], not references used for this thesis.

Table 1. Turn-on and threshold fields for various film emitters [1].

Emitter	E_{to} (V μm^{-1})	E_{thr} (V μm^{-1})	Reference
Diamond	24[a]	40[a]	[12]
Diamond B doped	16[a]	30[a]	[12]
Diamond Cs coated	10	28	[26]
Diamond N doped	1.5	≫8[a]	[13]
Amorphous carbon	4	50[a]	[14]
MW nanotubes	2.6	4.6	This work

[a] Values extrapolated from *I–V* characteristics.

Table 2 shows a compilation of field emission test results collected by Bonard *et al.* in [21]. The table shows that successful field emission has been reported for numerous types of CNT films. In the table, d is the inter-electrode distance, S is the emission area, J_{max} is the maximum current obtained without destruction of the emitter, n.a. means that the value was not indicated or could not be deduced by Bonard *et al.* in the reference's figures, and * indicates that the value was estimated or extrapolated from the data presented by the referenced paper. Note that in the table the references given are the references used by [21], not references used for this thesis.

Table 2. Field emission characteristics of various CNT films [21].

Reference	Emitter	d (μm)	S (cm^{-2})	E_{to} (V/μm)	E_{thr} (V/μm)	J_{max} (A cm^{-2})	Remarks
[22]	MWNT	10–40	0.002	n.a.	<25*	1	Very dense "tubulene" film
[153]	MWNT	15	0.003	n.a.	~15*	10	Very dense "tubulene" film
[24]	Arc MWNT	20	0.008	n.a.	20*	0.1	
[154]	Arc MWNT	30	0.007	4.0	6.5		
[113]	Arc MWNT	125	0.07	2.6	4.6		
[79]	Arc MWNT	125	0.07	1.1	2.2		Purified sample with closed caps
[124]	Arc MWNT	20–100	2.5×10^{-5}	7.5*	10*	0.4	Open tubes dispersed in epoxy
[155]	Arc MWNT	80	0.025	0.9*	4*		O_2 plasma treated tubes dispersed in epoxy
[126]	Arc MWNT	200	0.02	n.a.	1.5		Tubes dispersed in epoxy
[120]	SWNT	125	0.07	1.5	3.9		
[156]	SWNT	10–300	0.002	n.a.	4–7	4	
[157]	SWNT	150	3.1	2.1*	n.a.		
[91]	CVD MWNT	n.a.	0.001	1.7*	n.a.		
[93]	CVD MWNT	70	n.a.	n.a.	4.8–6.1		Aligned MWNTs, 15 emitters
[158]	CVD MWNT	150	3.1	n.a.	2.1*		Large amount of graphitic fragments
[134]	CVD MWNT	n.a.	0.0003	4.8	6.5	0.1–1	
[159]	CVD MWNT	600	0.07	n.a.	$\geqslant 5$		
[160]	CVD MWNT	150	0.2	3	6.6*		Si substrate
[99]	CVD MWNT	500	0.1	1.6	5*		Steel substrate
[99]	CVD MWNT	500	0.1	3	5.6*		Ni substrate
[161]	CVD MWNT	10–300	0.002	0.75	1.6	1–3	Catalyst supplied in gas phase
[162]	Graphitic fibers	300	1–10	2.1	n.a.	0.2	

Table 3 compares the field emission characteristics of various film types tested using the same experimental parameters. With some experimental variables controlled,

the impact of individual independent variables was investigated. Although Bonard *et al.* [21] drew some conclusions from comparing the tabulated data, the interpretation of the tabulated results was difficult and misleading because most groups used varied experimental procedures, varied more than one parameter, or did not characterize their samples completely. Note that in the table the references given are the references used by [21], not references used for this thesis.

Table 3. Field emission characteristics of CNT films with identical experimental conditions [21].

Reference	Influence	Emitter	d (μm)	S (cm^{-2})	E_{to} (V/μm)	E_{thr} (V/μm)	Remarks
[101]	Density and geometry	MWNT	25	n.a.	<2.7*	~4.8*	Random alignment
[101]		MWNT	25	n.a.	~40*	n.a.	Short vertical tubes
[79]	Geometry	Arc MWNT	125	0.07	2.6	4.6	Average over 15 emitters
[79]		SWNT	125	0.07	2.8	5.2	Average over 12 emitters
[79]		Open MWNT	125	0.07	4.5	30	Average over six emitters
[79]		Graphitic fibers	125	0.07	5.6	14	Average over five emitters
[164]	Surface treatment	MWNT ta-c coated	125–400	0.01	1.6	n.a.	
[164]		MWNT (as produced)	125–400	0.01	2.4	n.a.	
[121]	Density and geometry	SWNT	10–500	10^{-5}	n.a.	2.4	Randomly aligned
[121]		CVD MWNT	10–500	10^{-5}	n.a.	3.5	Dense aligned arrays
[165]	Density	CVD MWNT	125	0.007	9.8	14.4	Low density, patterned films (Fig. 5(a))
[165]		CVD MWNT	125	0.007	2.2	3.3	Medium density, patterned films (Fig. 5(b))
[165]		CVD MWNT	125	0.007	3.6	5.3	High density, patterned films (Fig. 5(c))

The comparison of the experimental results found in the literature is often beleaguered by minor variations of some sort in the way samples are prepared or handled, the experimental procedures used, or the experimental setup implemented. It is for this

reason that trends in data from some sources negate the trends shown by others. The question as to whether open or closed CNTs show more favorable field emission characteristics falls under this category. When comparing the field emission characteristics of open or closed CNT films, further details as to how the CNTs were initially fabricated, how they were opened, and other post-fabrication steps need to be considered.

2.3 Formation of Carbon Nanotube Films on Silicon Carbide

CNTs are typically produced by either arc discharge, laser ablation of a carbon target, or chemical vapor deposition. In each of these methods, CNT growth is made possible by the presence of metallic particles (typically Co, Fe, and/or Ni) acting as catalysts [6]. The growth of aligned CNT films on the surface of SiC substrates through surface decomposition presents a promising means of CNT growth, as metal catalyst are not necessary. The CNTs formed using this method are free of metal catalyst materials that alter the characteristic properties of CNTs ([7], [15]).

With catalyst-driven growth methods, the metal catalyst and non-nanotube carbon impurities need to be removed without damaging the CNT. To remove the catalyst metal and obtain greater purity, many purification methods have been developed [22]. A common approach has been to use strong oxidation, followed by an acid treatment. The oxidation step removes non-nanotube carbon and exposes the metal catalysts by removing its potential carbon coating. The drawback in this step process is that CNTs are lost or damaged during the oxidation process [22].

The surface decomposition of SiC substrates to produce CNT films was first discovered by Kusunoki *et al.* in 2000 [23] and has since been demonstrated by several other research groups ([13], [24], [25]). Using this method, the SiC film decomposes under the proper conditions and the freed carbon atoms self-organize to form CNT. The process is catalyzed by an oxidation reaction with residual oxygen gas in the chamber used for growth ([24], [25], [13]).

Specific conditions for producing CNTs through the decomposition of SiC substrates involve the following attributes: temperature of 1700^{o}C for half an hour or longer; and vacuum pressures of 10^{-3} to 10^{-5} Torr ([13], [26]). The key issue in preparing CNTs on SiC is controlling the oxidation process, such as not to allow solid SiO_2 to form on the SiC surface. This control of the active oxidation process is ensured by fabricating under the previously listed temperature and vacuum pressure growth attributes. An in-depth discussion of the interaction of oxygen with SiC surfaces at high temperatures is given by Song *et al.* in [27].

The growth results presented by Kusunoki *et al.* [26] showed that CNT growth was limited to the C-face of the SiC. In the work presented by Nagano *et al.* [24] and Mitchel *et al.* [13], however, CNT growth was observed on both the Si- and C-faces. The primary difference in the growth methods used by the two research groups was the surface cleaning and preparation techniques used [24].

Figure 16 (a) shows the highly aligned nature of the CNTs formed by Kusunoki *et al.* [28] through the decomposition of SiC. Both samples shown in Figure 16 were produced at 1700^{o}C and 1 x 10^{-4} Torr for half an hour. Figure 16(b) shows the inability of Kusunoki and coworkers to produce CNTs on the Si-face of SiC.

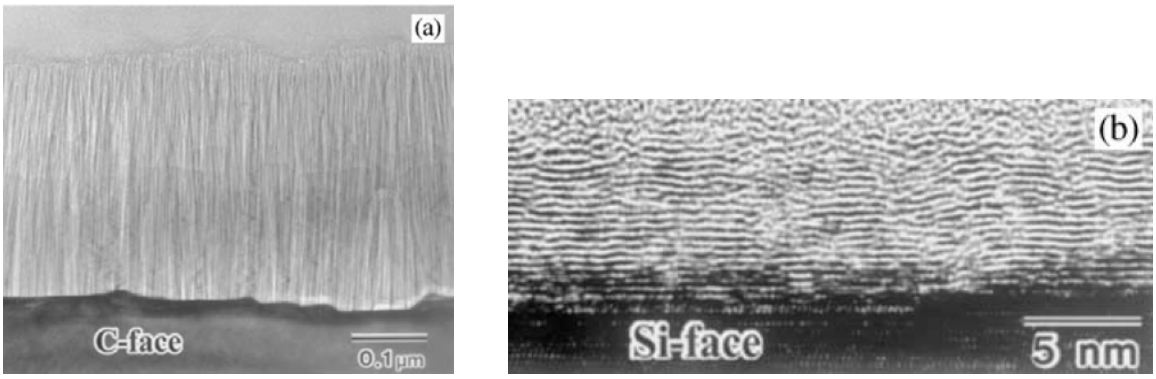

Figure 16. (a) Cross sectional TEM image of a CNT film grown on the C-face of SiC, and (b) graphitic layers that formed on the Si-face of SiC during growth [28].

The chemical reaction resulting in CNT formation is given by (2.30), (2.31), and (2.32) [24]. The oxygen gas acting as a catalyst to the chemical reaction is purported to be residual to the vacuum chamber, thereby making the level of oxygen content in the chamber during growth unknown.

$$SiC(s) \rightarrow Si(g)\uparrow + C(s) \tag{2.30}$$

and/or

$$SiC(s) + \tfrac{1}{2}\, O^2(g) \rightarrow SiO(g)\uparrow + C(s) \tag{2.31}$$

and/or

$$SiC(s) + CO(g) \rightarrow SiO(g)\uparrow + 2C(s) \tag{2.32}$$

The only application of CNT films fabricated through the decomposition of SiC is found in [29], by Ito *et al.* (co-written with Dr. Kusunoki). The paper investigates the field emission characteristics of the CNT film grown with varied parameters. Specifically, the field emission properties of opened and closed CNTs were compared, and the surface density of CNTs was varied.

For their study, SiC samples were heated at 1700^{o}C for varied lengths of time (0.5 – 10 Hours), under two vacuum conditions (3.75 x 10^{-2} Torr, and 7.5 x 10^{-5} Torr) [29]. To open the tubes, they were simply heated in air at 500 – 700^{o}C for approximately 20-minutes. Ito *et al.* found that the density of the CNTs formed at 7.5 x 10^{-5} Torr was approximately 30 billion CNTs per mm^2. Perceiving that this high density would be too dense and lead to high shielding effects between CNTs and poor field emission characteristics, Ito *et al.* decomposed SiC at 3.75 x 10^{-2} Torr, finding that the surface concentration was reduced to 10 billion CNTs per mm^2. AFM analysis confirmed the increased surface roughness of the sample grown at 3.75 x 10^{-2} Torr. It is assumed that TEM images were used to estimate the CNT surface density, although they did not specifically note how the value was determined. Ito *et al.* reported that field emission performance improved due to the increased level of surface roughness, and likewise, reduced electric field screening effects.

Through the investigation of the CNT films fabricated at varied growth times, Ito *et al.* found that the longer the heating time, the lower the surface resistance of the film [29]. The surface resistance of the CNT film heated for 10-hours decreased by a factor of ten compared with the sample heated for 0.5-hours. Ito *et al.* concluded their work by stating that the lowest threshold voltage was achieved by controlling the density of the CNTs, forming a conductive layer through long growth times, and opening the CNT caps. Figure 17 illustrates the improved field emission characteristics of the CNT film after the CNTs are opened [30].

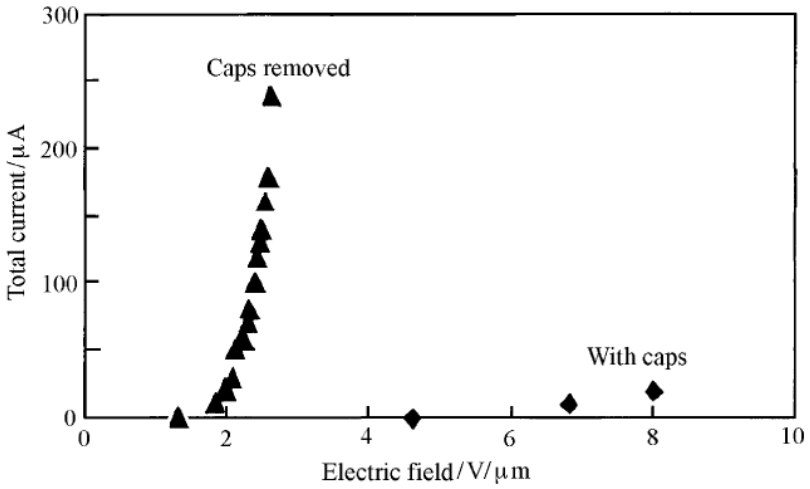

Figure 17. Current vs. voltage field emission characteristics of a CNT film grown through the surface decomposition of SiC [30].

2.4 Electrical Discharges in Vacuum

Field emission is the precursor to electrical breakdown. With this understanding, it is necessary to review other types of electrical discharges in vacuum in order to properly identify observed experimental results.

The first area of electrical discharges is noted as pre-breakdown, and contains two general categories [31]. The first category consists of steady or quasi-steady currents emitted from sites on the cathode through field emission or thermal emission. Field emission is the focus of this work, and will not be covered further in this section. The second category of pre-breakdown current falls under micro-discharges. Micro-discharges are self-limiting bursts of current that are caused by small clumps of material being detached from the cathode that cross the gap to strike the anode. Micro-discharges are also the result of a beam of electrons from the cathode vaporizing a small quantity of material on the surface of the anode. Micro-discharges tend to be most common in vacuum gaps with contaminants on either the anode or cathode surfaces.

The observance of both types of pre-breakdown phenomena, either concurrently or at different voltage levels is possible [31]. Pre-breakdown currents may affect the system as to directly cause breakdown, or they may affect the anode and cathode surfaces such that subsequent breakdowns are more or less likely. In certain high-voltage vacuum devices with low operating currents, pre-breakdown currents can increase to the point where the system's power supply becomes overloaded, preventing proper operation even though breakdown has not occurred [31].

The next area of electrical discharges involves breakdown, and contains four main categories of theories. First, the 'clump' theory states that breakdown is initiated by a particle becoming detached from one electrode, crossing the inter-electrode gap, and impacting the other electrode with sufficient energy to trigger the power supply to sense an overloaded condition [31]. This theory corresponds directly to the micro-discharge occurrence in pre-breakdown. Second, interaction theories assume that a chain reaction that involves electrons, positive ions, negative ions, and photons cause a rapid rise in pre-breakdown current which increases until breakdown of the vacuum gap occurs [31].

Third, cathodic theory assumes that the field emission of electrons from projections on the cathode causes heating and vaporization of the projections, introducing a supply of vapor or plasma into the inter-electrode gap sufficient to cause breakdown [31]. Lastly, anodic theory assumes that as the beam of electrons from the cathode strikes the anode, the beam heats up a small part of the anode surface to produce vapor, which is then ionized by the beam. This vapor consists of material evaporated from the anode, or contaminants desorbed from the surface of the anode, or both [31]. Such contaminants are common and often exist under ultrahigh vacuum conditions [31].

2.5 Stability of Field Emission Currents

The instability of observed field emission currents is discussed by several works found in the current literature. Evtukh *et al.* [32] state that undesirable field emission properties, such as large current fluctuations, low-frequency noise, and some occasional jumping have delayed the widespread application of field emission cathodes. The unavailability of highly reliable cathodes was believed to be solved with the discovery of CNTs; however, some works in the literature indicate that this is not the case ([32], [33]).

Regarding semiconductor materials as field emission cathodes, unstable emission behavior occurs due to the presence of native oxides, adsorbed impurities, chemical reactions with residual gases, and field erosion of the emission tips as a result of bombardment with residual gas ions and overheating [32]. Unstable emission currents from a CNT film were reported by Bonard *et al.*[33], noting that a gradual degradation of the emission performances with time was observed. Bonard *et al*. [33] reported $I-V$ characteristics acquired at different degradation stages showed a decrease in the field amplification factor, and SEM observations on films after emission revealed a substantial decrease of the CNT density.

Figure 18 compares the degradation over time of a single-walled CNT film with that of a multi-walled CNT film emitter [33]. Although the y-axis values are different in value for the two films, they are on the same scale. The degradation was assumed to be caused by the gradual destruction of the CNTs from ion bombardment by gas phase electron ionization or by ion desorption from the anode, both of which are induced by the emitted electrons. The single-walled CNT film degrades significantly faster, and is likely

due to the fact that the multiple walls of the multi-walled CNTs make them more robust and thereby less sensitive to ion bombardment.

Figure 19 illustrates the long-term emission stability at a constant emitted current of 3 mA/cm^2 for a closed multi-walled CNT film [33]. From the figure, it is clear that the applied voltage necessary to achieve a constant emission current density increases with time and is not overly stable.

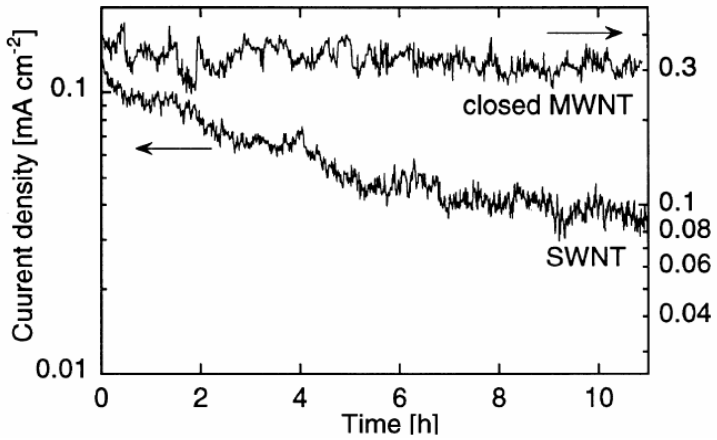

Figure 18. Emission stability for a closed multi-walled CNT and a single-walled CNT under a constant electric field [33].

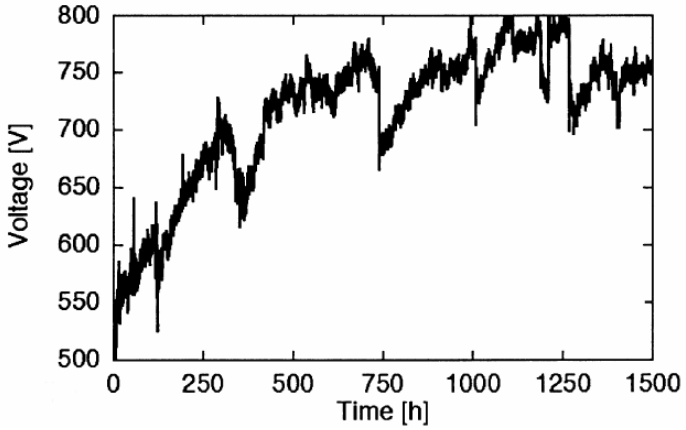

Figure 19. Long-term emission stability at a constant emitted current (3 mA/cm) for a closed multi-walled CNT film [33].

Song *et al.* [32] observed a rather unstable field emission current from a multi-walled CNT array, reporting a 15% fluctuation rate. It was concluded that during the periods of high fluctuation, the emission is dominated by adsorbents on the CNTs. After heating the sample to 400^{o}C for approximately 40-minutes, the field emission current was observed to become much more stable, with the fluctuation rate dropping below 5%. Along with reducing the fluctuation rate, the heating step caused the turn-on electric field to rise from 1.4 V/μm to 1.9 V/μm. Song *et al.* monitored the components of the released gases during the heat treatment using a mass spectrometer, and observed that the principal desorbed gas component was water vapor.

The alteration of an emission tip during field emission was noted by Zhirnov *et al.* [34], whereby after achieving a maximum current, the observed emission current dropped drastically (although this was not on a CNT emitter). SEM analysis of the diamond-coated Si emission tip following the drastic drop showed that the height of the emitter changed from 100 μm to 70 μm, indicating that the tip was destroyed. Figure 20 shows the shift in the emission characteristics, both before and after the destruction of the tip structure. This alteration in emission performance and corresponding SEM analysis indicating tip damage shows that the emission tip was sensitive to the high field effects.

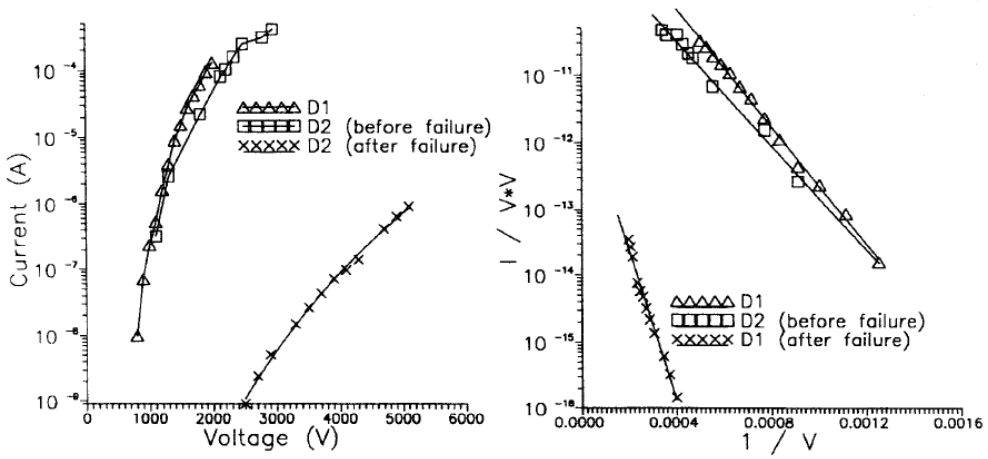

Figure 20. Field emission characteristics of a diamond-coated Si emitter, before and after failure [34].

2.6 Chapter Summary

This chapter provided an in-depth review of the electron field emission process, the quantitative theory describing field emission, the current field emission studies regarding CNTs, the fabrication of CNTs through the surface decomposition of SiC, and theories regarding the electrical breakdown in vacuum.

Chapter 3: Experimental Methodology

This chapter discusses the experimental approach taken to characterize the emission properties of a CNT film. The CNT growth procedures, along with the ohmic contact deposition steps are discussed. The chapter also discusses the sample holding apparatus fabricated for testing, the details of the overall vacuum system setup, and the data gathering and analysis methodology.

3.1 CNT Growth Procedures/Sample Preparation

CNTs are grown by the process described in "Growth of Carbon Nanotubes by Sublimation of Silicon Carbide Substrates," by Mitchel *et al.* [13], which in turn was adapted from the growth methods described by Kusunoki *et al.* discussed in section 2.3 of this work.

CNT fabrication involved using commercial grade n-type SiC substrates that had been polished on both sides using a standard mechanical polish and solvent cleaning [13]. Atomic force microscopy (AFM) measurements showed typical scratch marks due to residual polishing damage on both faces of the SiC. Figure 21 shows a topographical AFM image of the Si-face of the polished SiC wafer. The RMS value shown in Figure 21 is a measure of surface roughness (root-mean-square roughness), and is discussed in section 4.3. The SiC samples were then annealed at 1700^{o}C in a graphite resistance furnace (Oxy-Gon Industries, Inc, Epsom, NH) under a moderate vacuum (10^{-3} - 10^{-5} Torr), forming a dense CNT film on the surface of the SiC. The fabrication steps were carried out using AFRL/MLPS's equipment and assistance. Detailed fabrication steps can be found in Appendix B.

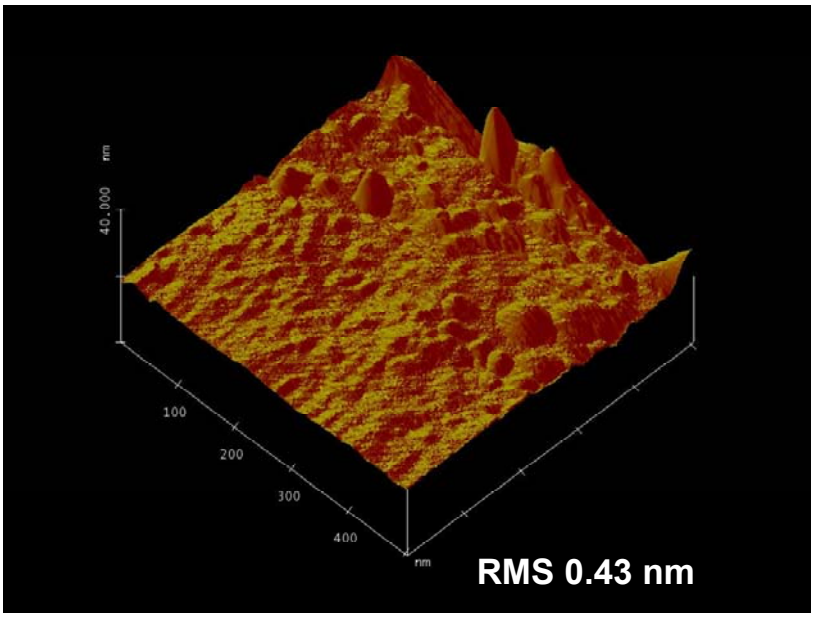

Figure 21. Atomic force microscopy image of the Si-face of the polished SiC wafer, showing typical scratch marks due to residual polishing damage.

Scanning electron microscope (SEM) images of the CNT film grown using the methods discussed are shown in Figure 22. The CNT film shown in the images was grown on the C-face of the SiC sample for 5-hours at 1700^{o}C and 10^{-5} Torr vacuum pressure, and was imaged by cleaving the sample to create a clean edge. The scans were taken with the sample placed at a 45^{o} angle relative to the electron beam of the SEM. Cross-sectional TEM images of the CNT films are shown in Figure 23 (courtesy of Dr. John Boeckl, AFRL/MLPS). The layer seen on top of the CNT film is platinum, which was deposited to protect the CNT surface during ion milling steps used to prepare the TEM samples.

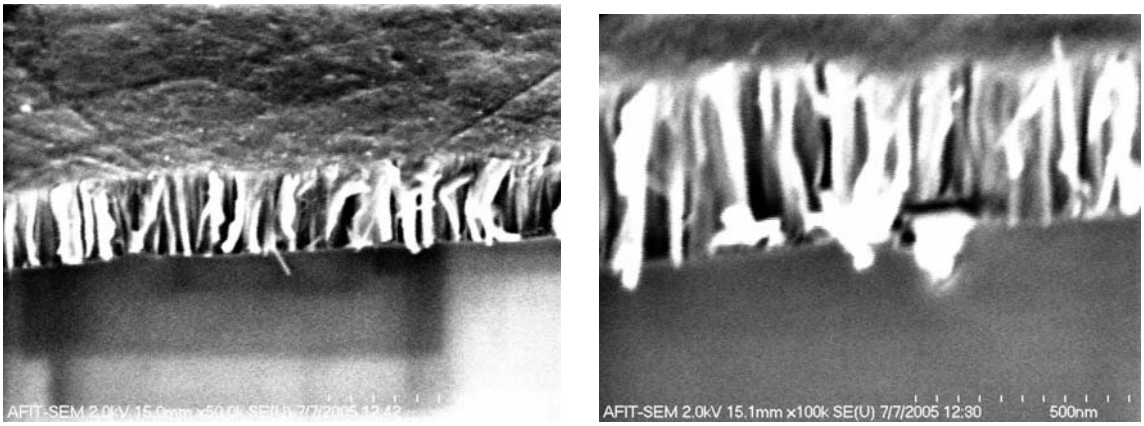

Figure 22. SEM image of CNTs grown on the C-face of SiC, 45^{o} stage tilt: 50,000x magnification (left), and 100,000x magnification (right).

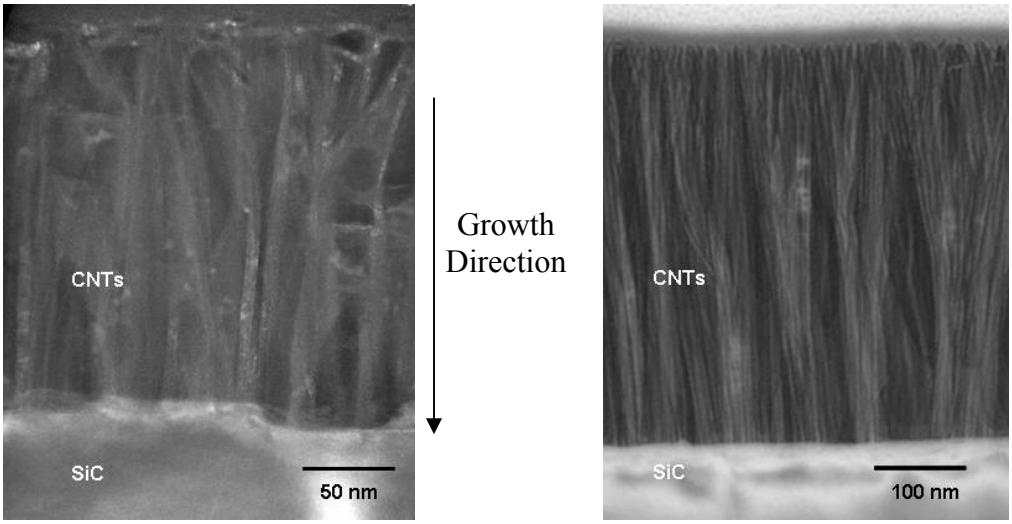

Figure 23. TEM cross-sectional image: (left) C-face – 1 hour decomposition time, and (right) Si-face – 2 hour decomposition time.

In a further attempt to characterize the emission surface, plan-view SEM images of the CNT samples were taken. Figure 24 shows the plan view of a C-face sample grown for 1-hour at 1700^{o}C and 10^{-5} Torr vacuum conditions. The image is inconclusive in regards to describing the surface topology of the sample. From the image, it is difficult to determine whether the contrasting circles on the SEM scan indicate CNT tips or are merely amorphous carbon nano-clusters. The large lighter gray areas are unidentifiable,

but are assumed to be layers of either: adsorbents such as oxygen that adhered to the surface following the sample's removal from the vacuum furnace; or graphitic layers that formed during either the temperature ramp-up or ramp-down process in the vacuum furnace.

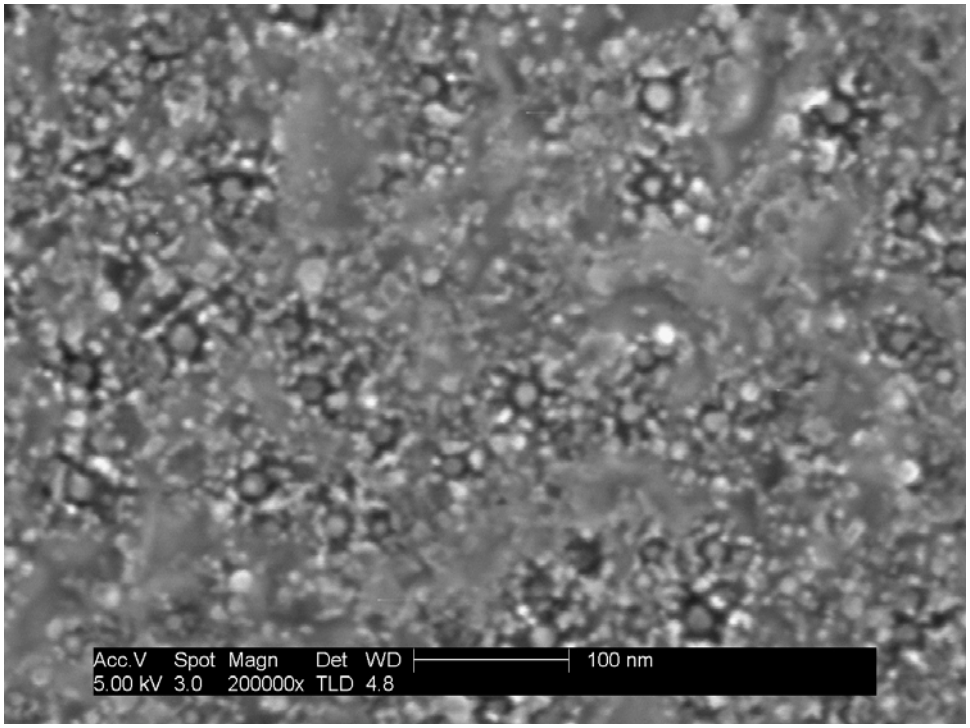

Figure 24. Plan-view SEM image of a CNT film grown on the C-face of SiC at 200,000x magnification.

For testing purposes, CNT growth procedures were varied in anneal time and chamber pressure. Post-growth steps were taken in an attempt to open the CNTs. The purpose of these variations was to investigate the effects chamber pressure and anneal time had on surface topology, and to determine the growth attributes that resulted in the most favorable field emission surface. Regarding growth times, the primary question resides in whether long growth times produce a dense CNT array with many CNT

'outcroppings.' Here, the term 'outcroppings' is used to describe individual CNTs that may grow taller than the rest on the sample, thereby reducing electric field screening effects and improving the surface's field emission characteristics.

The specific CNT growth parameters used are discussed in detail in section 3.5.

3.2 Deposition of an Ohmic Contact Layer

Due to the experimental setup chosen, shown in Figure 25, an ohmic contact was deposited on the backside of the SiC/CNT sample. This configuration ensured that the substrate's entire surface was capable of emitting electrons and that there were no points of interference caused by an electrical connection to the cathode.

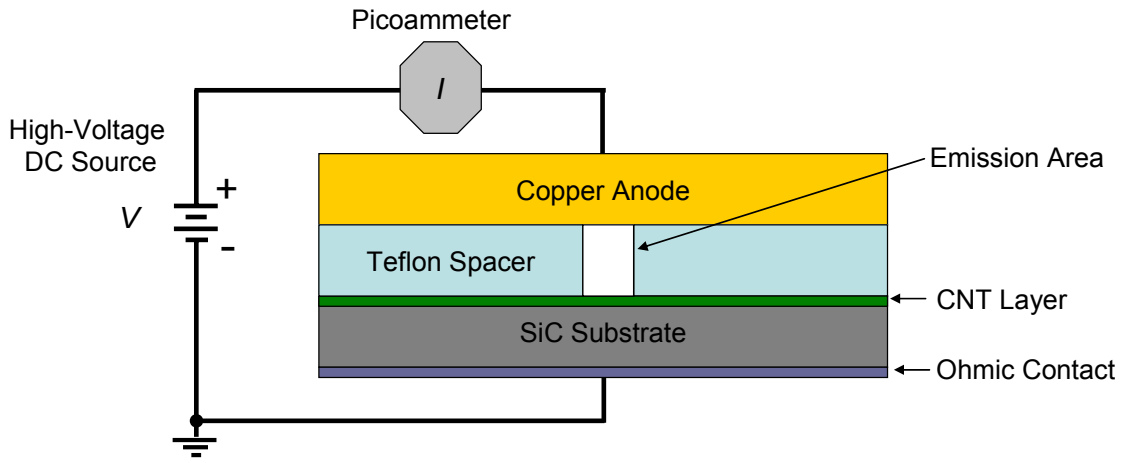

Figure 25. Illustration of the experimental setup showing the need for the ohmic contact.

As reported by Lu *et al.* [35], many materials, including metals, silicides, carbides, nitrides, and borides have been examined for their formation of ohmic contacts on SiC. The type of deposited material does not seem to be the most important factor in the formation of the contact; however, the primary factors are reported to be the use of a

highly doped SiC substrate (upper 10^{18} and 10^{19} cm^{-3}) and a thermal annealing step in vacuum at approximately 1000^{o}C or above [35].

Based on two papers written by Lu *et al.* ([36], [35]), an ohmic contact on the backside of the SiC sample was initially fabricated by depositing a 200 nm thick layer of nickel (Ni) on the SiC using an electron-beam evaporation system. The high evaporation temperature was assumed to suffice as the thermal annealing step. The deposition was carried out by first cleaning the sample with acetone, methanol, and a buffered oxide etch (weak hydrofluoric acid solution) to remove any oxide layers that may have formed on the substrate. Nickel was the metal chosen based on its common use and favorable performance in forming ohmic contacts on n-type SiC [36]. The results of the ohmic contact deposition were successful, as current versus voltage data showed a linear relationship indicating an ohmic contact was achieved. Figure 26 shows the CNT after the Ni contacts had been deposited on the backside of sample. Although the metallization process did not appear to harm the CNTs, this approach was not used to prepare samples for testing due to the potential of unknown affects on the CNT film.

In order to alleviate concerns that the metallization steps performed after CNT-growth steps may damage the CNT film, the ohmic contact was fabricated by depositing a 200 nm thick layer of tantalum (Ta) on the backside of the samples prior to surface decomposition in the graphite resistance furnace. The transfer length method (TLM) was used for assessing the Ta contact quality, and is discussed in section 4.1. Ta was chosen based on its extremely high melting point (3290^{o}C), and the notion that the type of metal used for the formation of ohmic contacts on SiC is not the central concern. Because the

Ta was deposited prior to CNT fabrication, the 1700°C growth process was assumed to be a suitable ohmic contact annealing step.

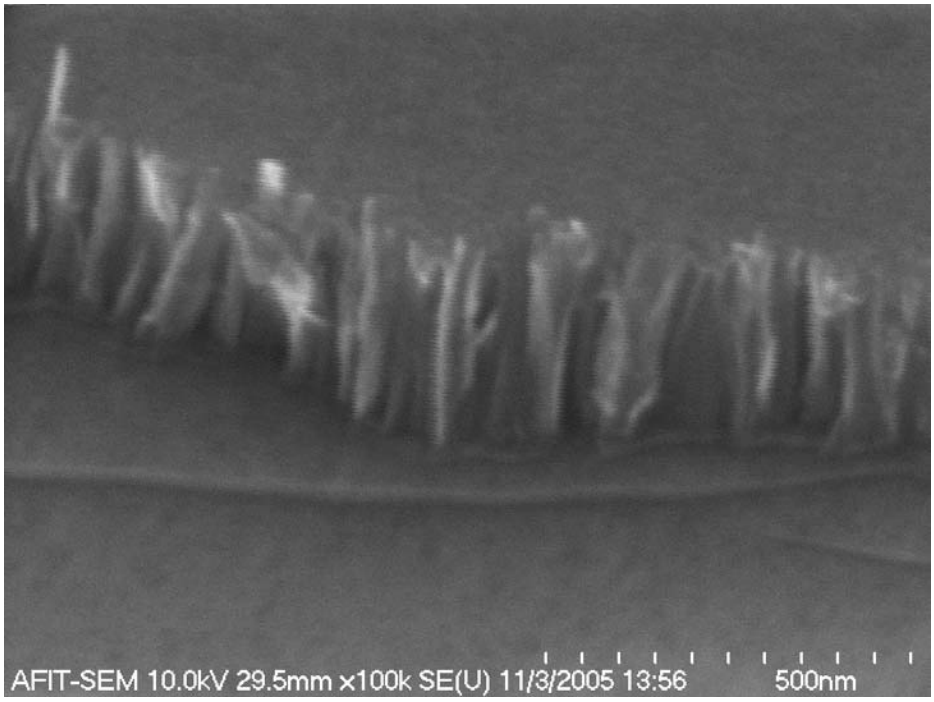

Figure 26. SEM image of a CNT film after Ni had been deposited on the backside of the sample.

3.3 Sample Holding Apparatus

Based on the experimental setup shown in Figure 25, a sample holding apparatus was fabricated, with the design shown in Figure 27. Note that in Figure 27 (b), the original acrylic sample holder arms were replaced after they broke due to fatigue (after testing all samples). Electrical crimp connecters were successfully used to firmly hold the copper anode in place on top of the SiC/CNT sample.

The test platform was electrically isolated from the stainless steel vacuum chamber by constructing the test platform on an acrylic plastic plate. As discussed in

section 3.2, the electrical contact to the SiC/CNT sample was achieved through an ohmic contact placed on its backside, thereby necessitating the sample to be placed on a conducting plate. To achieve this, a polished copper plate that was larger than the sample being tested was attached to the acrylic plastic plate that formed the base of the sample holder apparatus. The negative lead from the high-voltage supply was attached to the copper plate off to the side of the sample, ensuring that the anode and cathode were kept parallel to one another.

(a)

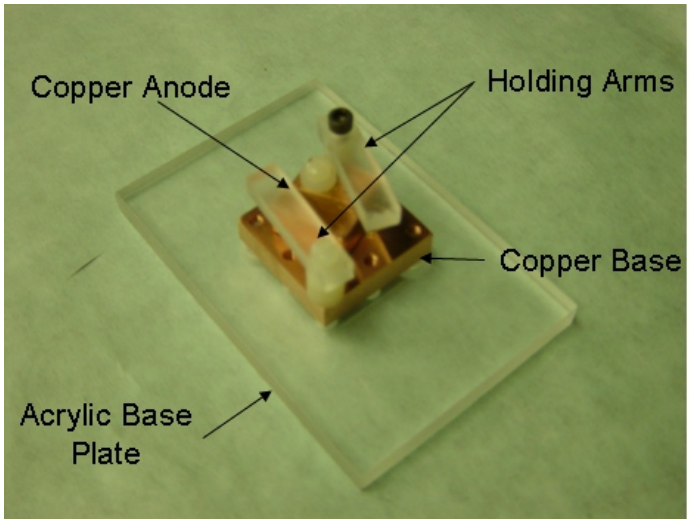

(b)

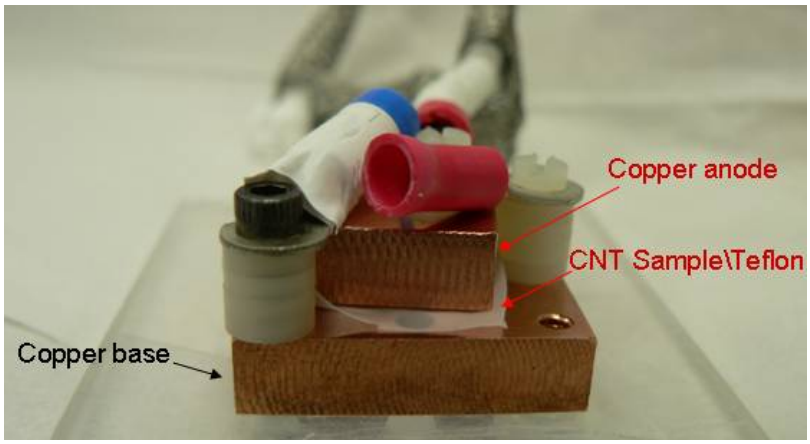

Figure 27. Sample holding apparatus fabricated for use in the vacuum chamber: (a) angle view, (b) side view. In (b), the original acrylic sample holder arms were replaced after they broke due to fatigue (after testing all samples).

A 100 μm thick Teflon® sheet was placed on top of the SiC/CNT sample such that the sample was completely covered by the Teflon®. In order to create a known area for field emission to occur, a 1/16" circular hole in the Teflon® was made using a punch tool. Figure 28 illustrates the circularity of the hole created using the 1/16" punch tool, allowing for a confident calculation of the hole's area based on the measured diameter using the SEM scale bar. Although the 1/16" inch diameter punch translates into a 1.5875 mm diameter hole, the effective diameter was measured to be 1.536 mm using the SEM scale bar. The material within the punched circle is the SEM sample holder's adhesive material. Teflon® was chosen based on its dielectric strength of 60 x 10^6 V/m. At a thickness of 100 μm, the Teflon® spacer is capable of withstanding an applied voltage of 6,000 VDC.

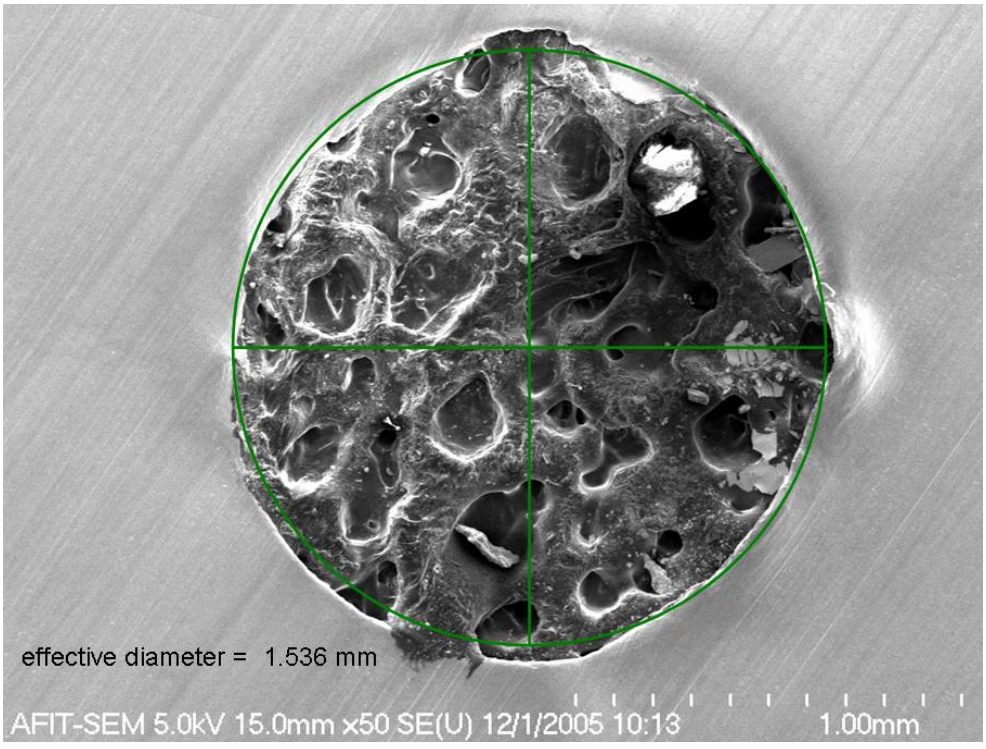

Figure 28. SEM image of the 1/16" hole made using the punch tool.

Although the hole made by the 1/16" punch appears to be rough at its edges, this roughness was considered acceptable due to optical microscope analysis of several holes made using the punch. Other methods used to try and make a suitable hole in the Teflon® sheet involved using a sheet metal punch and a drill. Regarding the sheet metal punch, the Teflon® material was not punctured, but was stretched. The drill, made specifically using a 1/16" bit while the Teflon® sheet was clamped tightly between two wood blocks, resulted in a highly non-circular hole, and is shown in Figure 29.

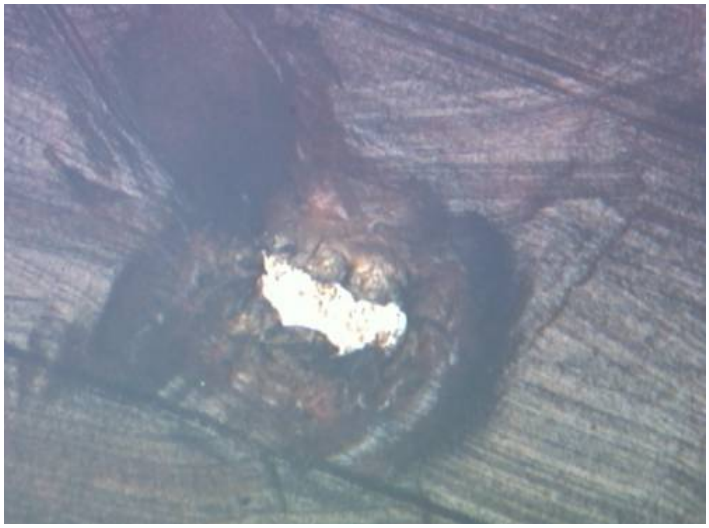

Figure 29. Non-circular hole in the Teflon® film made using a 1/16" drill bit (5x magnification).

A highly polished copper anode was placed on top of the Teflon® spacer, completely covering the hole in the spacer. The anode was polished using 4000 grit SiC sandpaper, along with a metal polish. The surface smoothness was verified using the a Zygo profilometer system, capable of creating a topographical map of micro-scale surface. Figure 30 (a) illustrates an optical microscope image, taken using 150x magnification, of the anode surface. Although under this level of magnification the

surface appears to be highly scratched, the profile given in Figure 30 (b) shows that the largest peak-to-valley displacement is 1.91 μm. To further support the acceptable smoothness of the copper anode, the profile given in Figure 30 (c) shows that the typical scratch on the anode surface is sub-micron, measuring approximately 350 nm. The apparent scratches in the anode can be considered negligible with respect to the anode-to-cathode separation distance, which as intended is dominated by the Teflon® spacer.

The Teflon® spacer must be large enough to cover the entire anode, ensuring that no unexpected field emission paths exist between the copper base and the anode. The positive lead of the high power voltage supply was connected to the top side of the copper anode. In order to secure the copper anode in place, two plastic arms, as shown in Figure 27 (a), clamp down on the anode.

Following fabrication, the components of the sample holding apparatus were thoroughly cleaned by means of an acetone soak, followed by an ultrasonic bath in methanol to remove residual oils and greases, to make the device vacuum ready. The dimensions of the sample holding apparatus can be found in Appendix B.

(a)

(b)

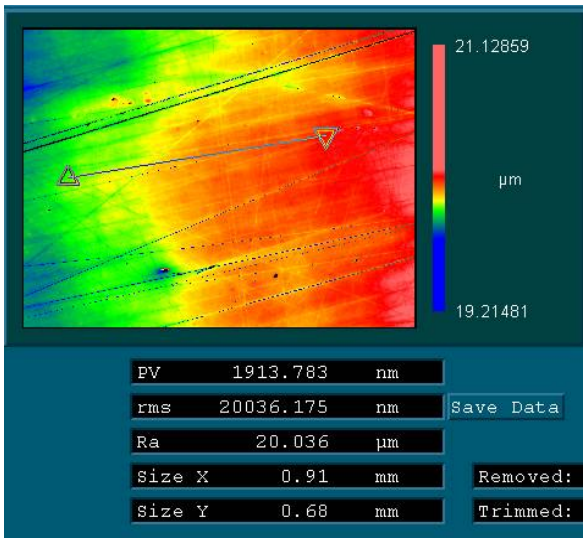

(c)

Figure 30. Images and data describing the surface smoothness of the copper anode: (a) optical microscope image showing minor scratch marks, (b) Zygo image of a portion of the anode showing a maximum peak to valley reading of 1913 nm, and (c) single profile along the area analyzed in (b).

3.4 Overall Vacuum System Setup

The experimental setup was created using various components owned by AFIT/ENG, borrowed from AFIT/ENP and AFRL/MLPS, and purchased from commercial suppliers. The overall vacuum system is shown in Figure 31.

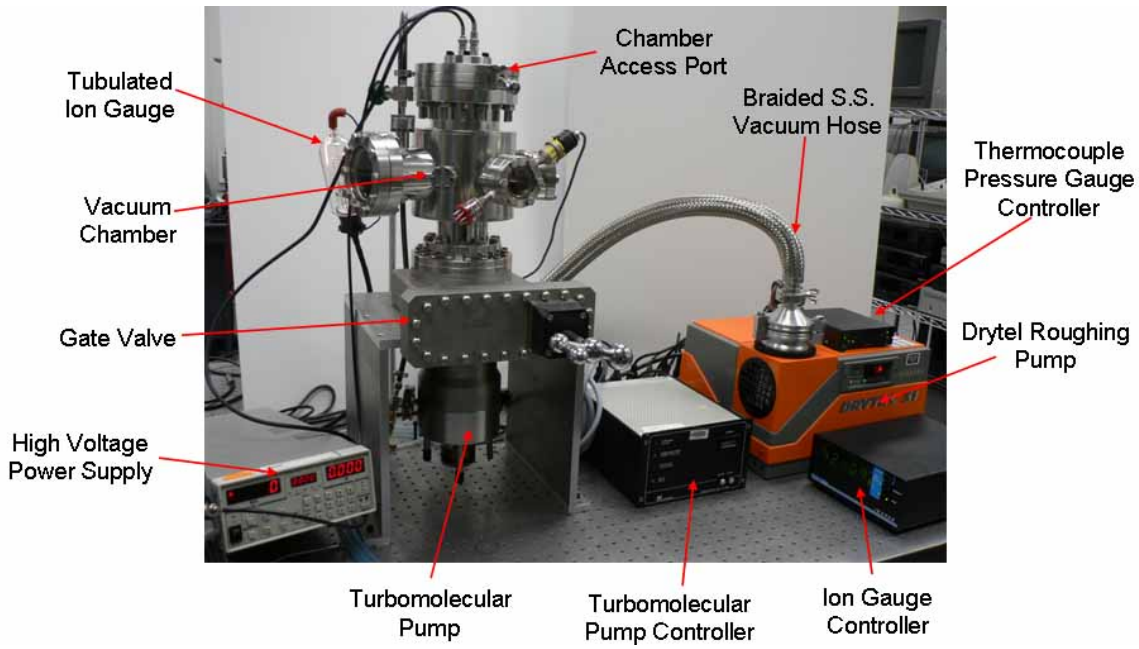

Figure 31. Image of the experimental vacuum system setup.

A Drytel 31 pumping system was used to provide a rough vacuum to the system. The Drytel 31 is a dry pumping unit incorporating an Alcatel molecular drag pump, which is designed to be used as a stand-alone, table top system for easy integration and is capable of reaching 7.5 x 10^{-6} Torr. The vacuum pressure necessary for the field emission test (a minimum of 1.0 x 10^{-6} Torr) was achieved using an oil-lubricated Leybold TURBOVAC 150 CSV turbomolecular pump. The turbomolecular pump was water-cooled using a Neslab RTE 110 chiller/recirculation unit. In order to maximize the effectiveness of the turbomolecular pump, it was situated directly beneath the vacuum

chamber. The initial setup connected the turbomolecular pump to the vacuum chamber with a 24-inch braided stainless steel vacuum hose. A remarkable difference was seen in the ultimate vacuum pressure achieved when the vacuum hose was removed and the chamber was placed directly above the turbomolecular pump (~6.0 x 10^{-6} Torr to ~1 x 10^{-9} Torr).

The high voltage needed for testing was supplied using a Stanford Research Systems, Inc. High Voltage Supply model PS350, capable of supplying up to 5000 VDC. The field emission current was measured using an Agilent 34410A Multi-meter capable of monitoring current to 10 nA accuracy and GPIB (IEEE 488) bus compatible. Electrical connections were passed into the vacuum chamber using a Miniature High Voltage (MHV) coaxial feed-through with a grounded shield, manufactured by the Kurt J. Lesker Company.

More detailed illustrations, and a complete list of the equipment used, are found in Appendix B.

3.5 Data Gathering/Interpretation Methodology

The growth parameters of the samples tested are listed in Table 4. The primary focus of each sample's testing was its turn-on voltage, threshold voltage, maximum current density, and emission current stability. CNT film growth at 10^{-3} Torr vacuum pressure was accomplished by operating the graphite heat resistance furnace with only the roughing pump pulling on the vacuum furnace chamber. The purpose behind this growth variation was to fabricate a rougher CNT film to decrease the electric field screening effects between neighboring CNTs, and thereby improve the films' field

emission properties. The low pressure growth was motivated by a work from Ito *et al.* [29], which stated that CNT films grown through the surface decomposition of SiC under poorer vacuum conditions were rougher than films grown under stronger vacuums.

Table 4. CNT Film Growth Parameters.

Time (hours)	Pressure (Torr)	SiC Face	Temperature (^{o}C)	Post Processing: Anneal Time/Temperature (minutes / ^{o}C)
0.5	10^{-5}	Si	1700	N/A
0.5	10^{-5}	Si	1700	10 / 620
0.5	10^{-3}	Si	1700	N/A
0.5	10^{-3}	Si	1700	10 / 620
3	10^{-5}	Si	1700	N/A
3	10^{-5}	Si	1700	10 / 620
3	10^{-3}	Si	1700	N/A
3	10^{-3}	Si	1700	10 / 620
5	10^{-5}	Si	1700	N/A

Data was gathered in a manner consistent with field emission tests discussed in section 2.2. The applied anode voltage was swept through a range of voltages necessary to achieve emission current densities of 10 μA/cm^2 and 10 mA/cm^2. These current density values were chosen due to their literature reference as figures-of-merit encountered in flat panel display technologies, where 10 μA/cm^2 and 10 mA/cm^2 are regarded as the current densities occurring at the turn-on electric field (E_{to}) and threshold electric field (E_{thr}), respectively [1].

The voltage sweeping process started at 100 VDC (1 V/μm), with 25 VDC (0.25 V/μm) step sizes. After currents in the tens of micro-amp range were measured by the

multi-meter, the step sizes were reduced to 20, or 10 VDC. For each voltage step, the current measured through the system by the multi-meter was recorded over 15-second intervals using the multi-meter's GPIB interface and a PC. From the recorded time-interval data, the average, median, maximum, and minimum current densities were calculated. The current stability over time was analyzed using this time-interval data by calculating the standard deviation of the current values collected.

The applied voltage was increased until the internal protection mechanism of the high voltage power supply sensed a current overload and tripped, causing it to remove the applied voltage and reset itself. The internal protection mechanism of the high voltage supply resets itself when a current of 5.3 amps is drawn. The 5.3 amps necessary to overload the supply is not a DC current, but is a transient value resulting from a momentary overload from the cathode to the anode that causes a large energy transfer between the two. The cause and result of the power supply current overloading (also referred to as tripping) are discussed in section 4.3. After the power supply would trip, the voltage was reapplied starting at 100 VDC (1 V/μm) and the ramping cycle restarted. The procedure was repeated on each sample until current was no longer observed either: prior to the tripping of the power supply; or overall (up to the power supply's maximum of 50 V/μm).

The test results have been normalized into applied electric field values (in V/μm) for comparison with values found in the literature. This normalization was done by dividing the applied voltage by 100 because of the 100 μm thick Teflon® sheet separating the CNT film from the copper anode. The recorded current was manipulated into a

current density by dividing it by the field emission area, yielding a normalized value comparable with values found in the literature as well.

After collecting an adequate number of current density versus applied electric field data points for each sample, the data was analyzed using the F-N model, given by plotting $\ln(I/V^2)$ versus $1/V$. In the F-N plot, V represents the applied voltage (VDC) or applied electric field (V/μm), and I represents the emission current density (A/cm^2). The plotted curve will be linear if the current is the result of field emission.

The numerical analysis approach mirrored the approach taken by both Manohara *et al.* [19] and Li *et al.* [20], which was presented in section 2.2. Equations (3.1) and (3.2) restate equations (2.27) and (2.29), respectively. In equation (3.1), a and b are constants extracted from the F-N plot. In equation (3.2), β represents the field enhancement factor, ϕ represents the emitter's work function in eV, and d is the gap between the anode and CNT tip in μm [19].

$$\ln(\frac{I}{V^2}) = \ln(a) - \frac{b}{V} \tag{3.1}$$

$$b = 6.87 \times 10^9 (\frac{\phi^{3/2} \cdot d}{\beta}) \tag{3.2}$$

By measuring the slope of the F-N plot, the constant b was calculated [19]. Next, knowing the value of b, the field enhancement factor for a given sample was calculated [19]. Lastly, the values of E_{to} and E_{thr} were compared with values given by Bonard *et al.*[1] shown in section 2.2.

In summary, testing focused on measuring E_{to} and E_{thr}, the field enhancement factor, and the current stability over time for each of the samples tested.

3.6 Chapter Summary

This chapter covered the experimental approach taken to characterize the emission properties of a CNT film. The chapter discussed CNT growth and sample preparation procedures, the sample holding apparatus fabricated for testing, and the vacuum system setup used for testing.

Chapter 4: Results and Analysis

The intent of this chapter is to discuss the results collected during the experimental portion of this thesis. First, the results of the Transfer Length Method (TLM) analysis of the tantalum (Ta) ohmic contact deposited on the backside of the SiC wafers are presented. Next, the results of the post-growth annealing used to open the CNTs are presented. Third, an observational analysis of the field emission characteristics of each CNT film type is presented. Lastly, the field emission properties of the CNT films tested are compared with one another, highlighting apparent trends and discussing inadequacies in the data collected and experimental methodology.

4.1 Measuring Contact Resistance Using the Transfer Length Method

The Transfer Length Method (TLM) was used to assess the ohmic contact resistivity between the 200 nm thick Ta layer and SiC wafer. The Ta deposition step was carried out prior to CNT fabrication to avoid post-growth damage to the CNTs during metal deposition and to use the 1700^{o}C CNT growth temperature as the thermal annealing required for ohmic contacts.

TLM involves collecting current versus voltage data at varied ohmic contact pad separation distances on a sample [37]. An example of the TLM pattern used is given in Figure 32, showing Ta pads of the same size spaced at varied distances from one another.

The total resistance between any two pads of the TLM pattern is taken as the series combination of three resistive elements: a metal to semiconductor contact, a channel through the semiconductor connecting the two pads, and a contact from the semiconductor to metal. Because the pad sizes of the TLM pattern are designed to be

equal, and knowing that by definition the ohmic contact resistivity is the same for both polarities (from Ta to SiC and for SiC to Ta), the series combination of the three elements can be reduced to: $2R_{pad} + R_{semi}$ [37]. Although R_{semi} can be calculated both experimentally and theoretically, it will not be discussed further as the focus of the section is on evaluating the ohmic contact's resistivity.

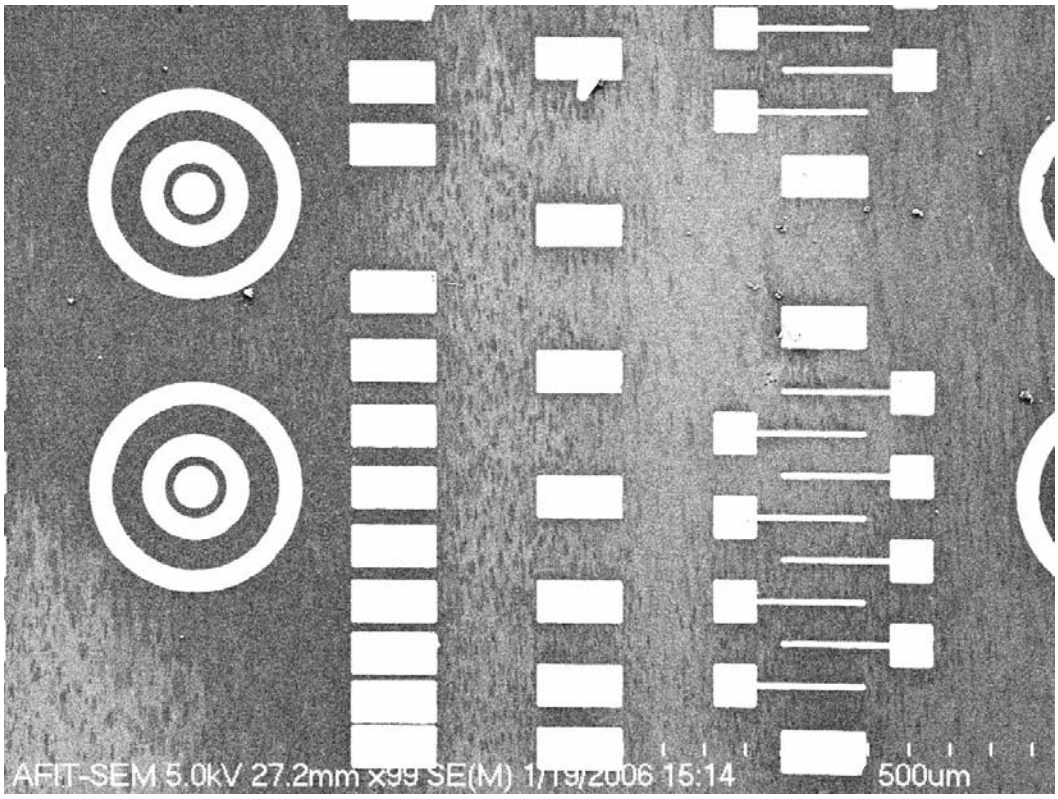

Figure 32. SEM image of the TLM pattern.

Figure 33 illustrates current versus voltage (*I vs. V*) curves for various pad separation distances on a sample that had been annealed at 1700°C during a 5-hour CNT growth. The linearity of the *I vs. V* curves indicates that the contacts are ohmic, and the reciprocal of the slope for each individual curve is the total resistance of the three resistive element circuit at that separation distance. In Figure 33, pairs 1 through 6

correspond to increasing pad separation distances, and their respective decreasing slopes indicate that as the pad separation increases, the resistance between them also increases.

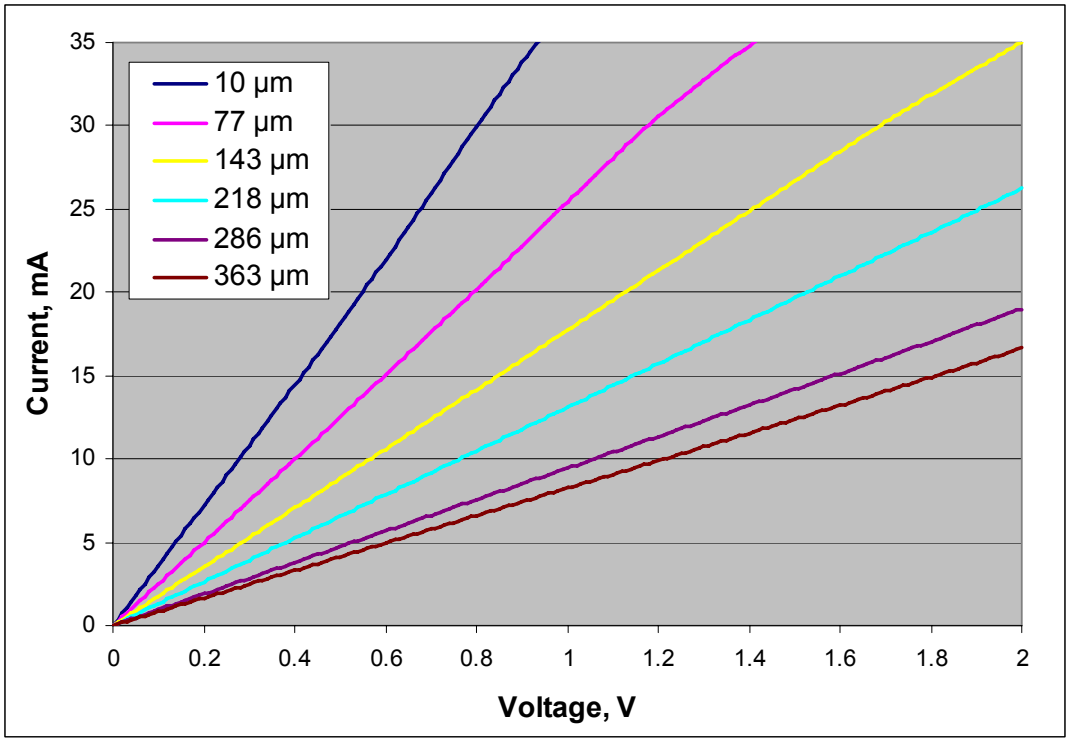

Figure 33. TLM data giving *I vs. V* curves for various pad separation distances (5-hour anneal at 1700°C and 10^{-5} Torr).

By extracting the slopes of the *I vs. V* curves shown in Figure 33, taking their reciprocals, and matching this data with the corresponding pad separation distances, a plot is generated allowing for the calculation of $2R_{pad}$ (Figure 34). $2R_{pad}$ is determined by extrapolating the data such that the pad separation value goes to 0 µm. At this point, R_{semi} is assumed to be removed from the three element system connecting the two pads and the resistance value remaining is entirely due to the metal-to-semiconductor contact resistance [38].

In Figure 34, the six data points and the least squares line fitting the collected data are plotted. From the figure, the $2R_{pad}$ value was determined to be 21.1 Ω by extrapolating the least squares fit line so the pad separation distance equaled zero. R_{pad} was then calculated to be 10.55 Ω, and knowing that the TLM pad area was 5.0×10^{-5} cm^2, the contact resistance per unit area was calculated to be 5.275×10^{-4} Ω-cm^2 [38]. Assuming that the average SiC/CNT test sample is 1 cm^2, then the total resistance between the Ta layer and the SiC substrate is a mere 5.275×10^{-4} Ω. Assuming the peak emission current expected is in the range of 0.20 mADC, the peak voltage drop across the ohmic contact is calculated to be 1.055×10^{-7} VDC. Using the same approach, the peak power dissipation across the ohmic contact can be calculated to be 21.1 pW. Both the peak voltage drop and power dissipation across the ohmic contact are small enough to have little effect on the function of the overall system.

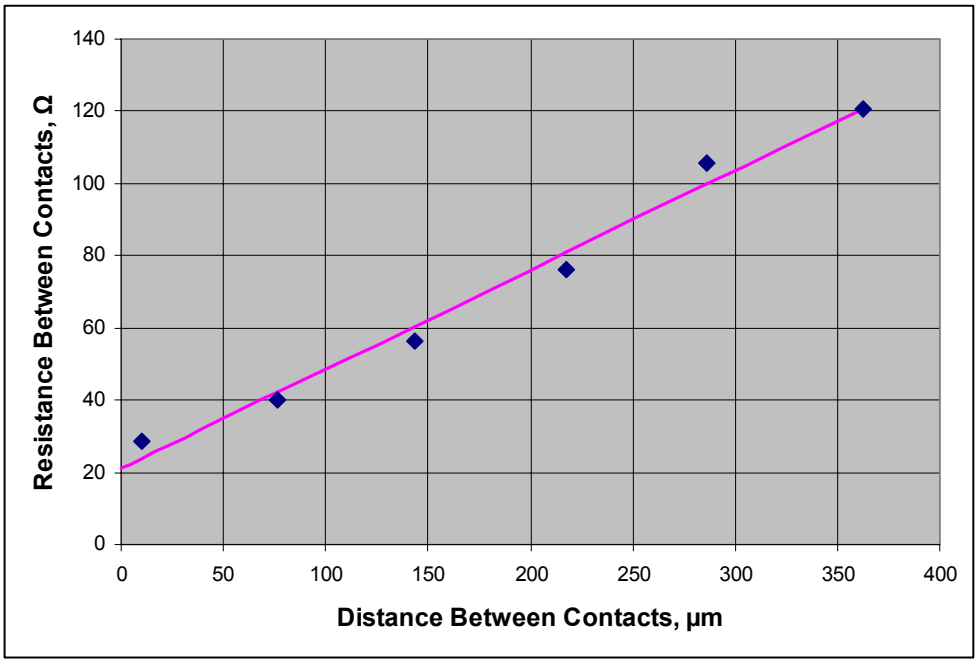

Figure 34. TLM data giving measured resistance between pads versus pad separation and the least squares fit line to the data (5-hour anneal at 1700°C and 10^{-5} Torr).

Proof that the 1700°C CNT fabrication step fulfills the annealing requirement in ohmic contact generation is shown by the *I vs. V* curve taken across two TLM pads on a non-annealed sample in Figure 35. The non-linearity of the curve shows that the contact is not ohmic, as its shape indicates more of a Schottky-type contact.

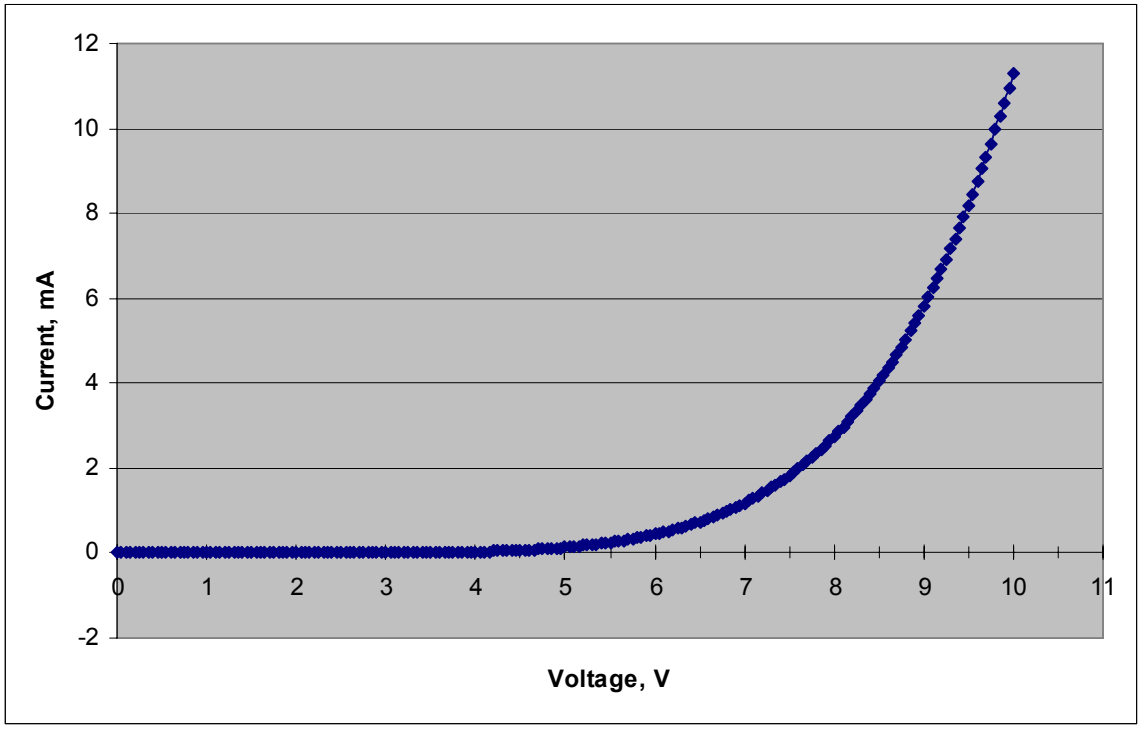

Figure 35. TLM data giving *I vs. V* curve for a non-annealed sample.

To ensure that a 5-hour anneal time was not necessary to form the ohmic contact between the Ta and SiC, a SiC sample with a Ta TLM pattern on its C-face was annealed at 1700°C during a 0.5-hour CNT growth. Figure 36 shows the corresponding *I vs. V* curves for various pad separation distances, with each curve's linearity indicating that the contacts are ohmic. Figure 37 shows the measured resistance between contacts plotted against their respective separation distances, as well as the least squares fit to the data.

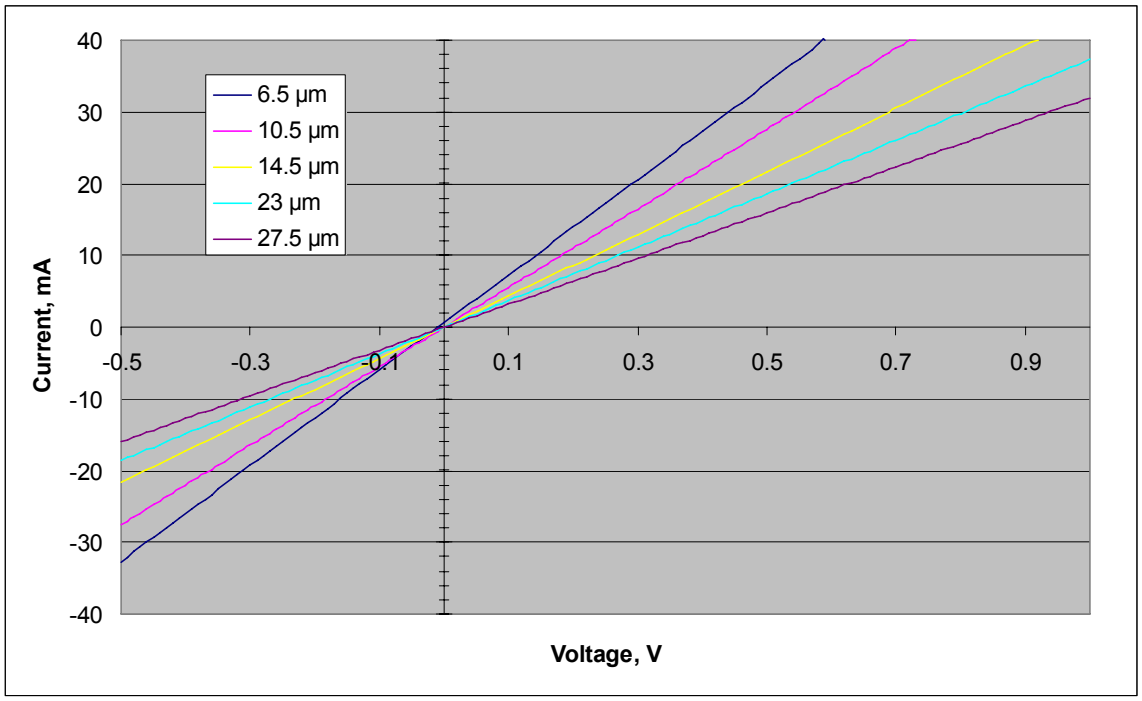

Figure 36. TLM data giving *I vs. V* curves for various pad separation distances (0.5-hour anneal at 1700°C and 10^{-3} Torr).

From Figure 37, showing the data points and the least squares line fitting the collected data, the extrapolated $2R_{pad}$ value was determined to be 10.7 Ω. R_{pad} was then calculated to be 5.35 Ω, and knowing that the TLM pad area was 5.0 x 10^{-5} cm^2, the contact resistance was calculated to be 2.675 x 10^{-4} Ω-cm^2 (compared to 5.275 x 10^{-4} Ω-cm^2 for the 5-hour anneal sample). Therefore, the contact resistance of the 0.5-hour sample is approximately one half that of the 5-hour annealed sample.

The initial assumption was that a longer annealing time would result in a lower contact resistance, as more Ta atoms could diffuse into the semiconductor material. Experimental results disproved this assumption, allowing for the conclusion that the 5-hour anneal is beyond the optimal ohmic contact anneal time. Upon analyzing the post-anneal Ta contact patterns using an optical microscope, the 5-hour anneal sample's

contacts appear very brittle and are easily damaged and cracked-off the substrate by the probe tips used for the *I vs. V* analysis. It is believed that the long anneal time caused the TLM contact pads to separate from the SiC substrate at the edges. The cause for this separation is unknown, as the melting point for Ta is 3290°C, and CNTs did not appear to have formed under the contact pads.

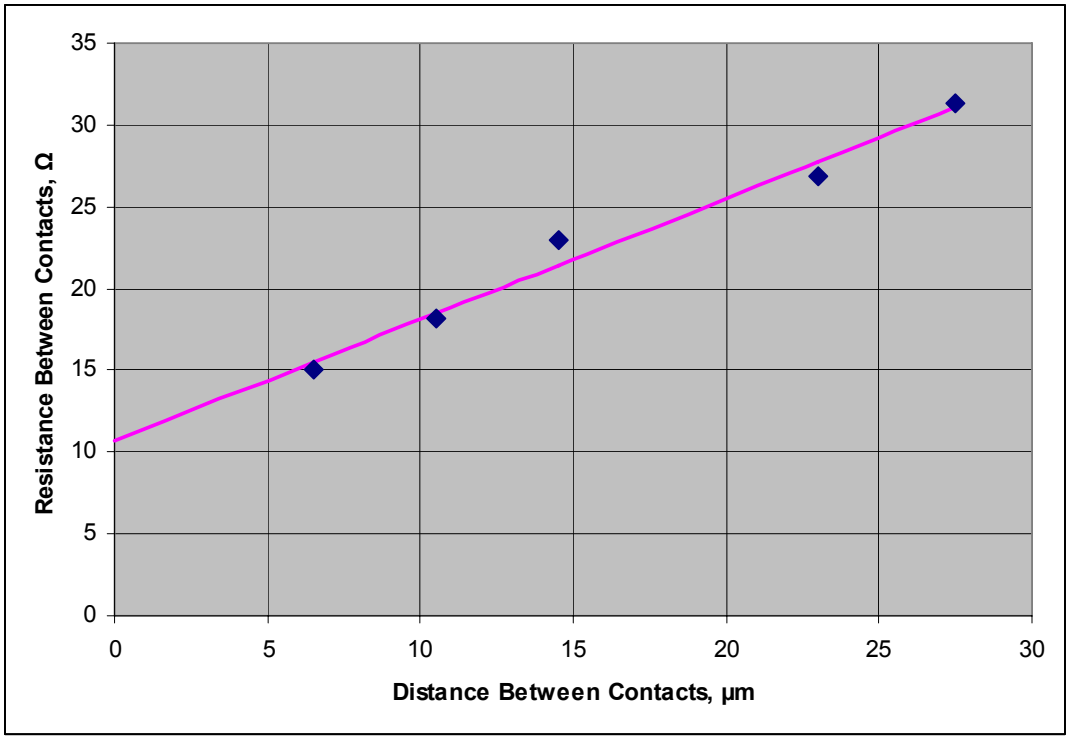

Figure 37. TLM data giving measured resistance between pads versus pad separation and the least squares fit to the measured data (0.5-hour anneal at 1700°C and 10^{-3} Torr).

Figure 38 shows images of a non-annealed, 0.5-hour annealed, and 5-hour annealed sample. The 5-hour annealed sample appears to have the most damage from the annealing, regardless of the fact that the 1700°C anneal temperature is well below the 3290°C melting point of Ta. The non-annealed sample's substrate appears to be out of focus in the image; however, this is because the SiC substrate is semitransparent prior to

CNT growth. Figure 39 shows the damage caused by contacting the TLM pattern pads with the probe tips while taking *I vs. V* curves on the sample. This damage did not occur on either the non-annealed or 0.5-hour annealed samples during *I vs. V* analysis.

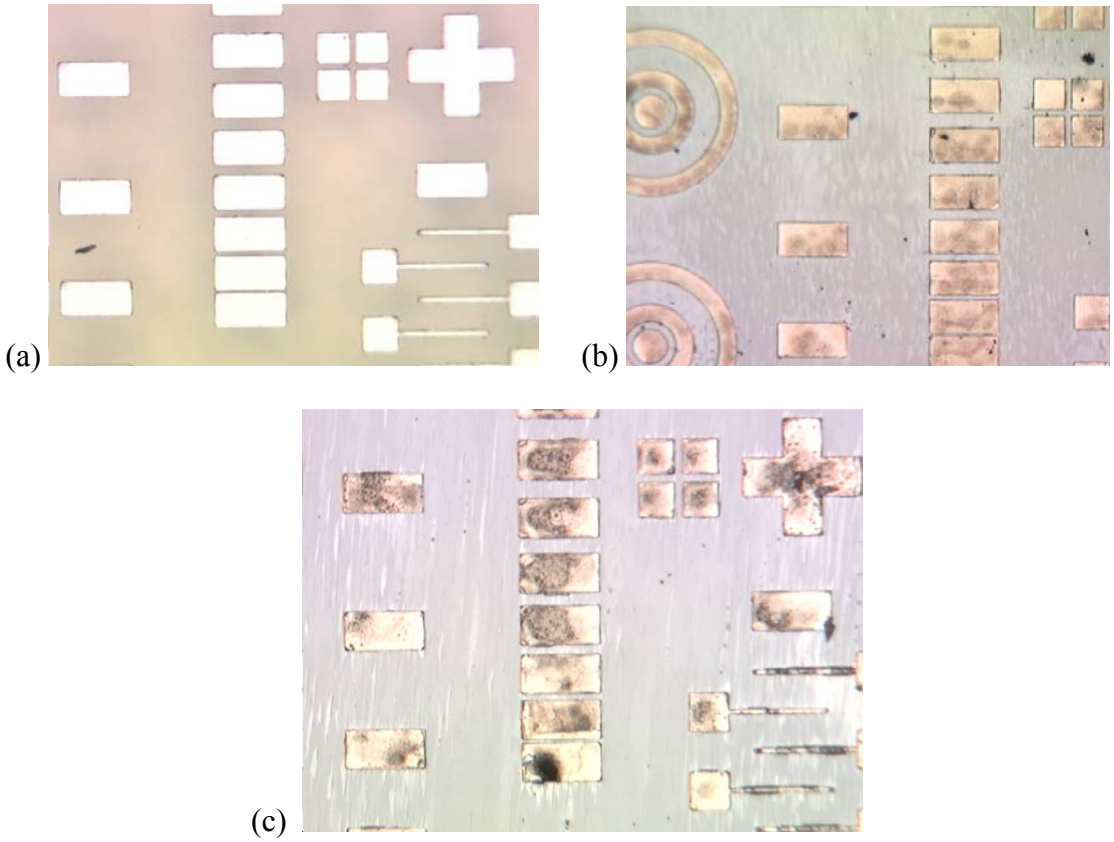

Figure 38. Optical microscope images of the TLM pattern: (a) non-annealed, (b) 0.5-hour anneal at 1700°C and 10^{-3} Torr, and (c) 5-hour anneal at 1700°C and 10^{-5} Torr (10x magnification in each image).

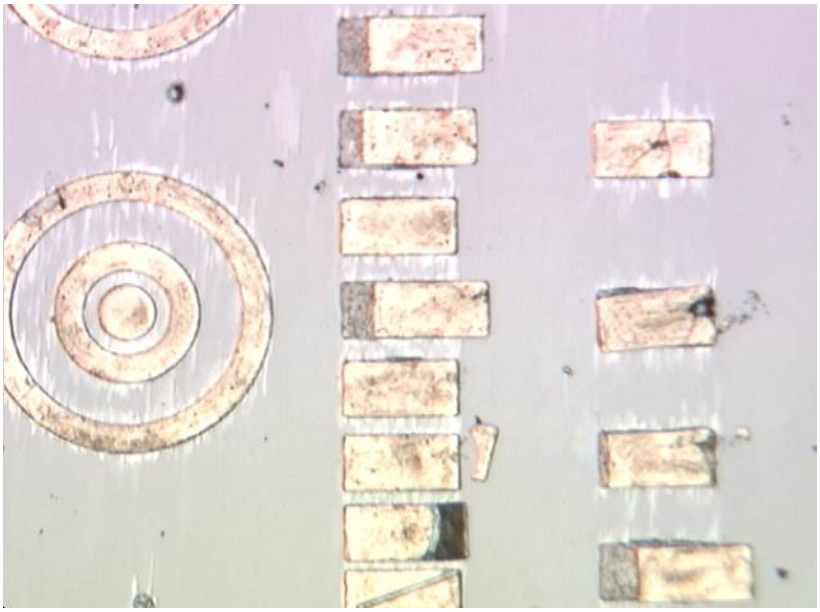

Figure 39. TLM sample after a 5-hour anneal at 1700°C and 10^{-5} Torr showing damage caused by the probe tip (20x magnification).

4.2 Post Fabrication Processing of the Carbon Nanotube Films

According to Kung *et al.* [21] and Ito *et al.* [29], a CNT film's field emission characteristics can be enhanced by opening the ends of the CNTs. Specifically, Kung *et al.* found that by annealing a CNT film at 400°C for 20- and 25-minutes in oxygen (O_2), the turn-on electric field decreased from 0.8 to 0.6 V/μm. TEM work by Kung *et al.* showed that the ends of many CNTs were opened or partially opened after the O_2 annealing process. It was also found by Kung *et al.* that annealing under the presence of O_2 beyond an optimal measure of time causes damage along the CNT walls, resulting in decreased emission currents. Ito *et al.* demonstrated that by annealing CNT films (at 620°C for 20-minutes under the presence of O_2) grown via the decomposition of SiC substrates produced similar tube-opening results that led to improved field emission characteristics.

For the purpose of this thesis, fabricated CNT films were opened using the approach described by Ito *et al*. Initial work involved annealing both Si- and C-face grown CNTs (1-hour growth time in the Oxy-Gon furnace, at 1700^{o}C) for 20-minutes at 620^{o}C in a tube furnace with O_2 flowing. SEM analysis revealed that after annealing the samples, the CNTs were completely removed from their surfaces. Figures 40 through 45 illustrate before and after SEM images of the SiC/CNT surface. From the post-anneal SEM images, it is noted that the surface decomposition process dramatically alters the surface morphology of the SiC substrate. Looking closely at the post-anneal plan-view SEM scans, tightly packed circular rings on the substrate's surface are observed. These circular rings are believed to be the result of the SiC substrate surface decomposition process which forms the CNTs, as they were not observed prior to CNT growth.

Additional trials showed that the CNTs were completely removed from the 1-hour growth sample after annealing for 10-minutes at 620^{o}C. SEM analysis of annealing trails for 1- and 5-minutes at 620^{o}C appeared to not change the CNT surface (corresponding SEM images can be found in Appendix C).

Figure 40. C-face CNTs grown at 1700°C under 10^{-5} Torr vacuum for 1-hour, pre-anneal, 30° tilt, 80,000x magnification.

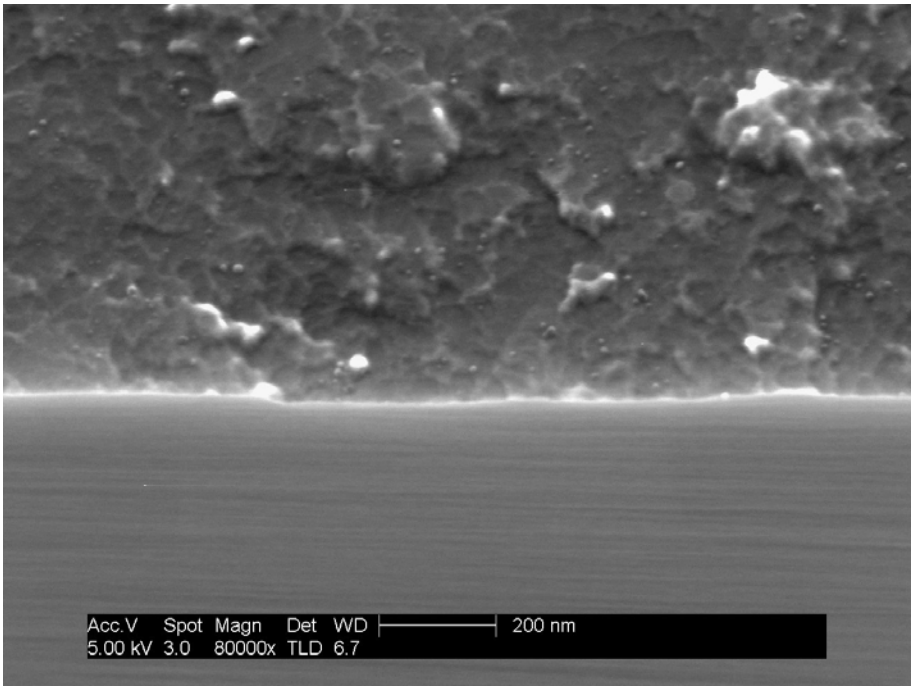

Figure 41. C-face CNTs grown at 1700°C under 10^{-5} Torr vacuum for 1-hour, after a 10-minute anneal at 620°C in flowing O_2, 30° tilt, 80,000x magnification.

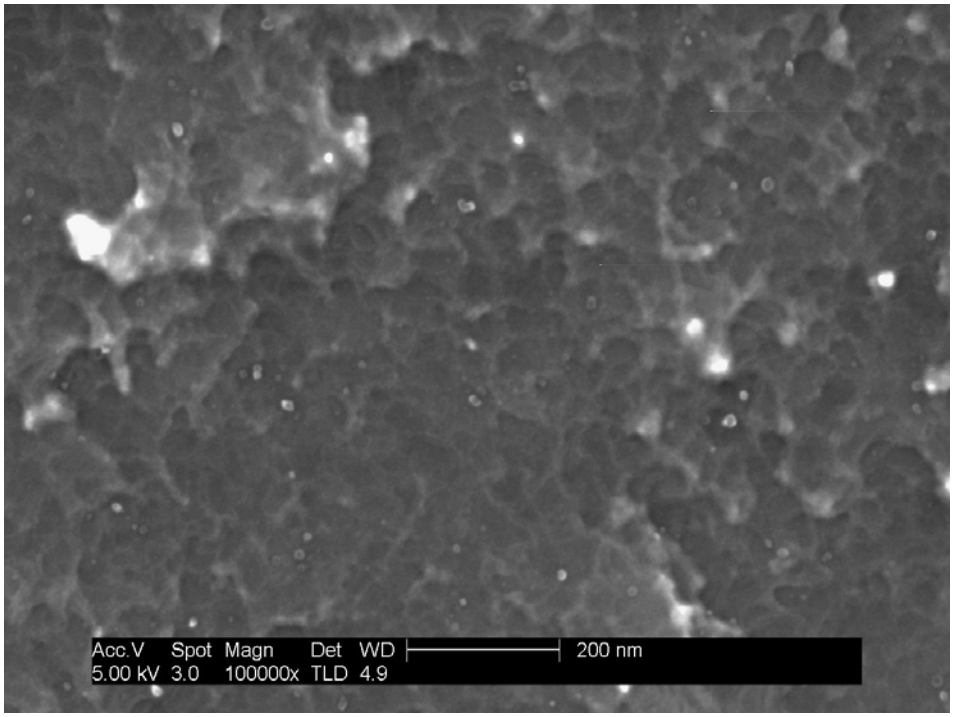

Figure 42. C-face CNTs grown at 1700^{o}C under 10^{-5} Torr vacuum for 1-hour, after a 10-minute anneal at 620^{o}C in flowing O_2, plan-view, 100,000x magnification.

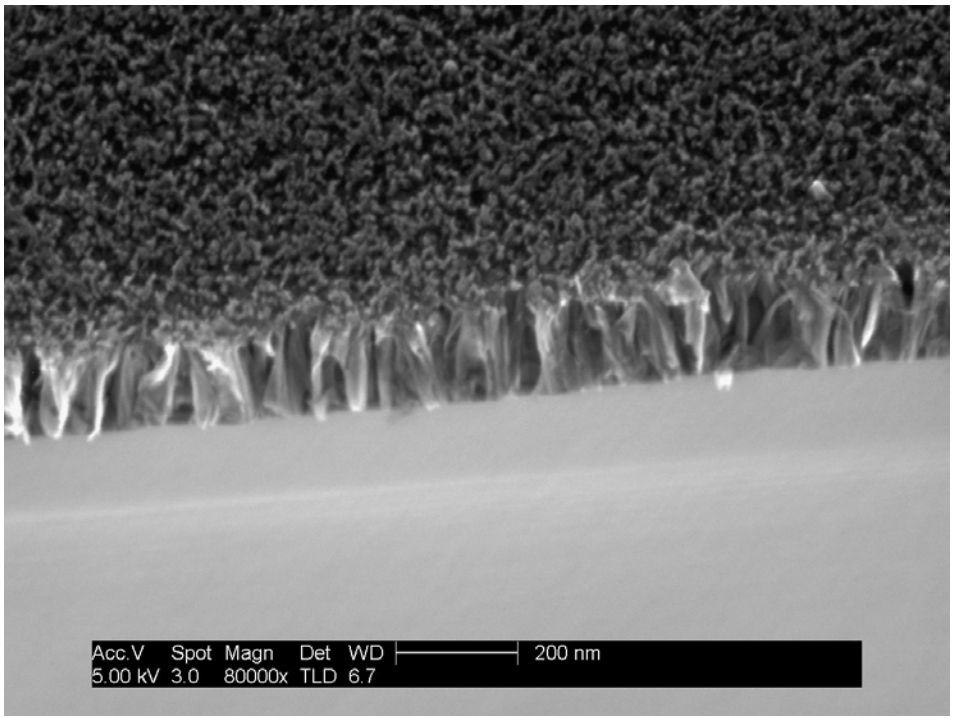

Figure 43. Si-face CNTs grown at 1700^{o}C under 10^{-5} Torr vacuum for 1-hour, pre-anneal, 30^{o} tilt, 80,000x magnification.

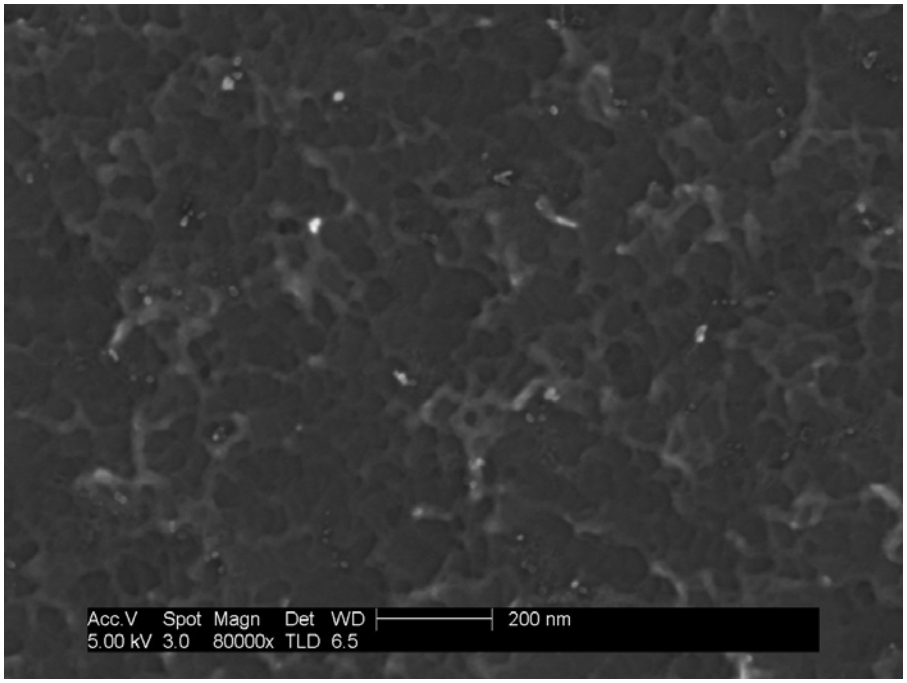

Figure 44. Si-face CNTs grown at 1700^{o}C under 10^{-5} Torr vacuum for 1-hour, after a 10-minute anneal at 620^{o}C in flowing O_2, plan-view, 80,000x magnification.

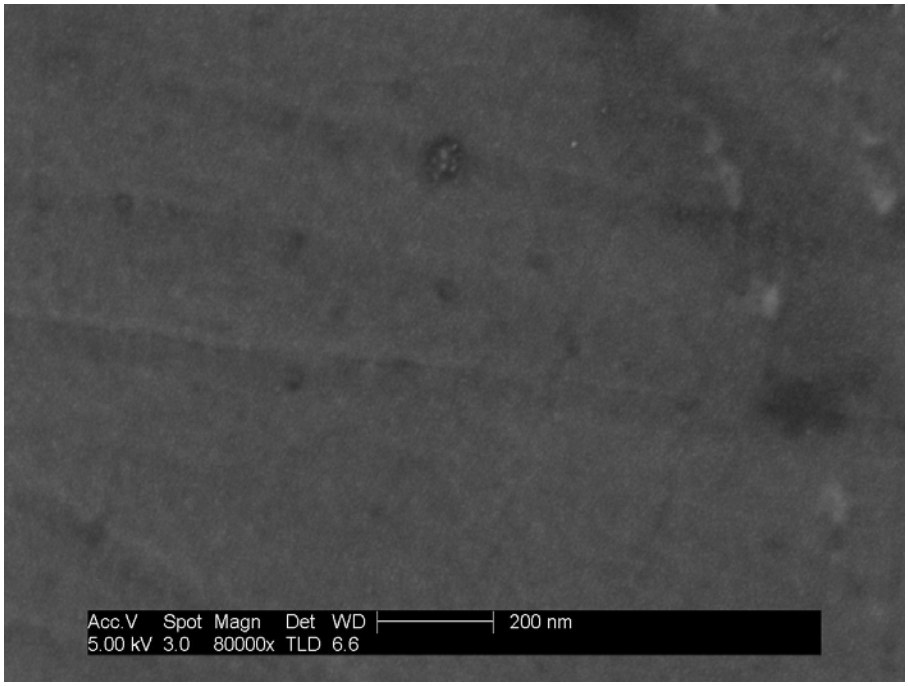

Figure 45. C-face, SiC surface prior to CNT growth, plan-view, 80,000x magnification.

4.3 Field Emission Analysis

This section discusses the field emission characteristics of the samples tested. Testing began by cleaning the samples with an acetone and methanol rinse, and blowing them dry with N_2, before insertion into the sample holding apparatus. Testing involved ramping the applied electric field from 1.00 V/μm to an electric field high enough to cause the power supply to sense a current overload and trip itself off (referred to as electrical breakdown). A primary trip of the high voltage power supply indicates that a current spike reaching 5.3 ADC was registered by the power supply. At electric field steps where the multi-meter registered a current through the device, the current was recorded for a finite time period (typically two data points per second for 15-seconds) using the GPIB interface and Agilent Multi-link software Microsoft Excel plug-in. From the recorded time-interval data, the average, median, maximum, and minimum current densities were calculated. The current stability over time was analyzed using this time-interval data by calculating the standard deviation of the data sets collected.

After electrical breakdown occurred for a sample, the electric field ramping process was repeated in order to determine if the occurrence of electrical breakdown altered the CNT film's field emission properties in any way. The electric field ramping process was repeated for each sample until current was no longer observed either: prior to the tripping of the power supply; or overall (up to the power supply's maximum of 50 V/μm). Successive electric field rampings are referred to as 'runs' and are denoted as 'run 1', 'run 2', 'run 3', etc. Initial electric field rampings that did not result in measurable currents were not included in this nomenclature.

4.3.1 Data from Individual Samples Tested

0.5-Hour Growth, 10^{-5} Torr, 1700°C, No Post-Growth Annealing:

Testing of the CNT film grown at 1700°C under 10^{-5} Torr vacuum pressure for 0.5-hours with no post-growth annealing was performed at a vacuum pressure of 4.7 x 10^{-7} Torr. Initially, no recordable current was observed in the system prior to a trip of the high voltage power supply at 13.0 V/μm. A primary trip of the high voltage power supply indicates a current spike reaching 5.3 ADC was registered by the power supply. Detailed analysis regarding the cause of primary voltage trips will be discussed later.

Following the initial primary trip of the voltage supply, a current was observed in the system beginning at 3.00 V/μm (denoted as run 1). Figure 46 shows the data collected for the six sequential runs that followed the initial trip. The figure shows that after the first run (run 1), increasing the applied electric field had a much smaller impact on the current produced in the system. The first run showed excellent field emission characteristics, with a low turn-on electric field (54.8 μA/cm^2 at 3.0 V/μm) and high maximum current density (4.25 mA/cm^2 at 6.7 V/μm). Refer to section 2.2 to see corresponding field emission characteristics of field emitters found in the literature. How well these values compare with those found in the literature and with other samples tested will be discussed later in this section.

To determine if the current through the system was the result of field emission, the collected data was plotted in F-N format. F-N plot format involves plotting *1/V vs*. *ln(I/V^2)*, and a linear relationship is indicative of field emission, as opposed to thermionic emission or unpredictable pre-breakdown currents stemming from the ionization of

particles from the cathode and their subsequent impacting of the anode. Figure 46 shows the F-N plot of the data collected from runs 1 through 6.

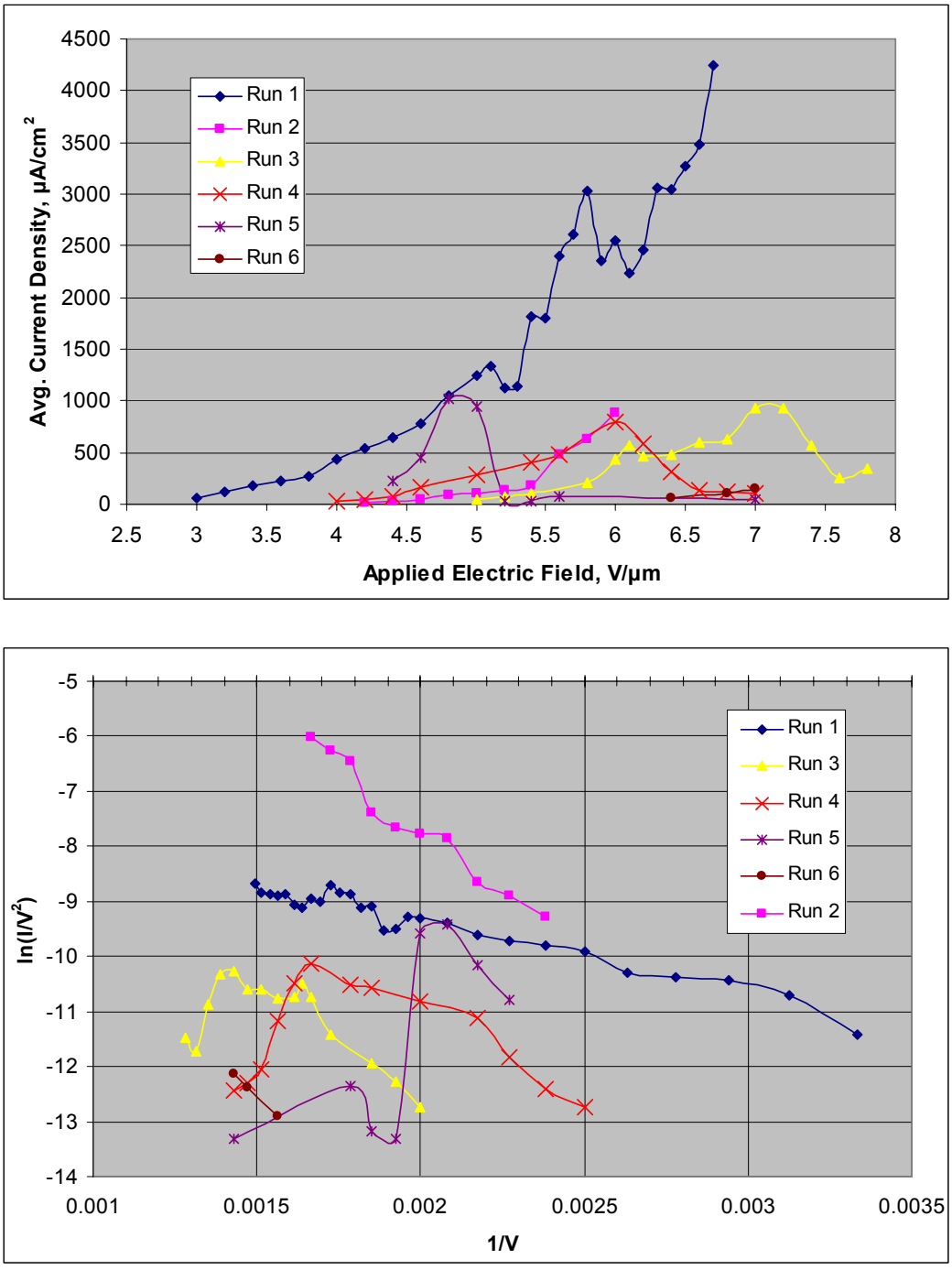

Figure 46. Field emission data for the CNT film grown at 1700°C under 10^{-5} Torr vacuum pressure for 0.5-hours and with no post-growth annealing.

The plotted F-N data for the first two runs appears linear (Figure 46), indicating that the recorded current for these two runs is a result of field emission. Although portions of the F-N plot for runs 3 through 6 appear linear, the non-linear portions indicate that field emission is not the dominant cause of the recorded current. Refer to Figure 14 (page 31) for an F-N plot found in the literature, and note that its discontinuities are similar to those seen in Figure 46 and others plotted later in this section.

Extracting the slopes of each curve using a least squares fit of the data, the field enhancement factor was calculated to be 5091.4, 1428.5, 1651.8, and 2107.2 (unitless) for runs 1 through 4, respectively. The field enhancement factor was not calculated for runs 5 and 6 because the slope calculated using the least squares fit approach that was within reason (the value was positive as opposed to negative). The field enhancement factor dropped significantly after the first run and rose from runs 2 through 4. A high field enhancement factor is desirable, as it amounts to requiring lower applied electric fields for field emission. It is referred to as an enhancement factor because it represents the amplification factor of the electric field due to local 'outcroppings' on the emission surface. The latter portion of section 2.1 (page 20) discusses the field enhancement factor.

Because the field enhancement factor is directly related to the surface topology of a sample, a change in its value reflects a change in the sample's surface topology. The large drop in field enhancement factor (5091 to 2107) indicates that 'outcroppings' were destroyed, leaving a smoother emission surface. One explanation for field enhancement

factor's increase from runs 2 through 4 is that the applied electric field caused the desorption of adsorbed ions, leaving a rougher surface behind.

The stability of the emission current is illustrated in Figure 47, where the measured current density is plotted over a 15-second time span. The standard deviation of this data was 64.62 μA/cm^2, while the average current density was 3,277 μA/cm^2.

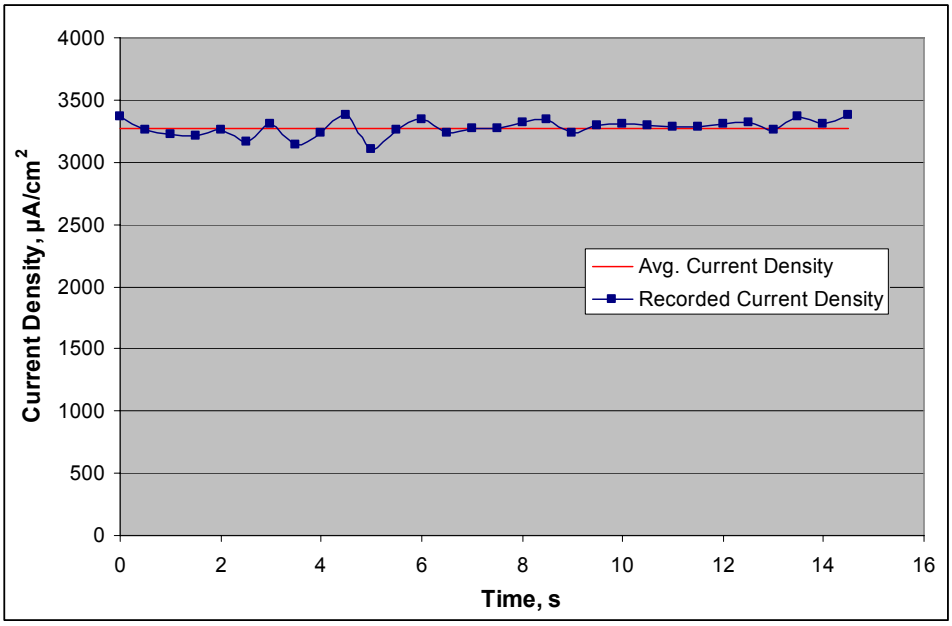

Figure 47. Stability plot for the CNT film grown at 1700°C under 10^{-5} Torr vacuum conditions for 0.5-hours and with no post-growth annealing, 6.5 V/μm applied electric field.

For each voltage step on the CNT film grown at 1700°C under 10^{-5} Torr vacuum for 0.5-hours with no post-growth annealing, the average maximum deviation from the average current measured (for run 1 only) was 20.56%, which is relatively low considering this takes into account errant current spikes. The corresponding maximum deviations from the average current measured for runs 2 through 6 were 28, 32, 38, 61, and 51%, respectively, showing that the currents were much less stable after the initial

run. Likewise, the standard deviation was calculated for each group of data collected at each voltage step. Calculating the percentage the standard deviation (for each voltage step) represented with respect to the average for each voltage step, and averaging these values, it is seen that on average the standard deviation is a mere 12.2% of the mean value for each voltage step. This calculated stability measure is further explained in the *Comparison of Samples Tested* (page 110) portion of this section.

The likely cause of the change in field emission characteristics after the initial run was visually apparent following the removal of the sample from the sample holding apparatus (after the sixth run). Marks on the surfaces of both the CNT film and copper anode were noticeable to the naked eye, and are shown in Figure 48.

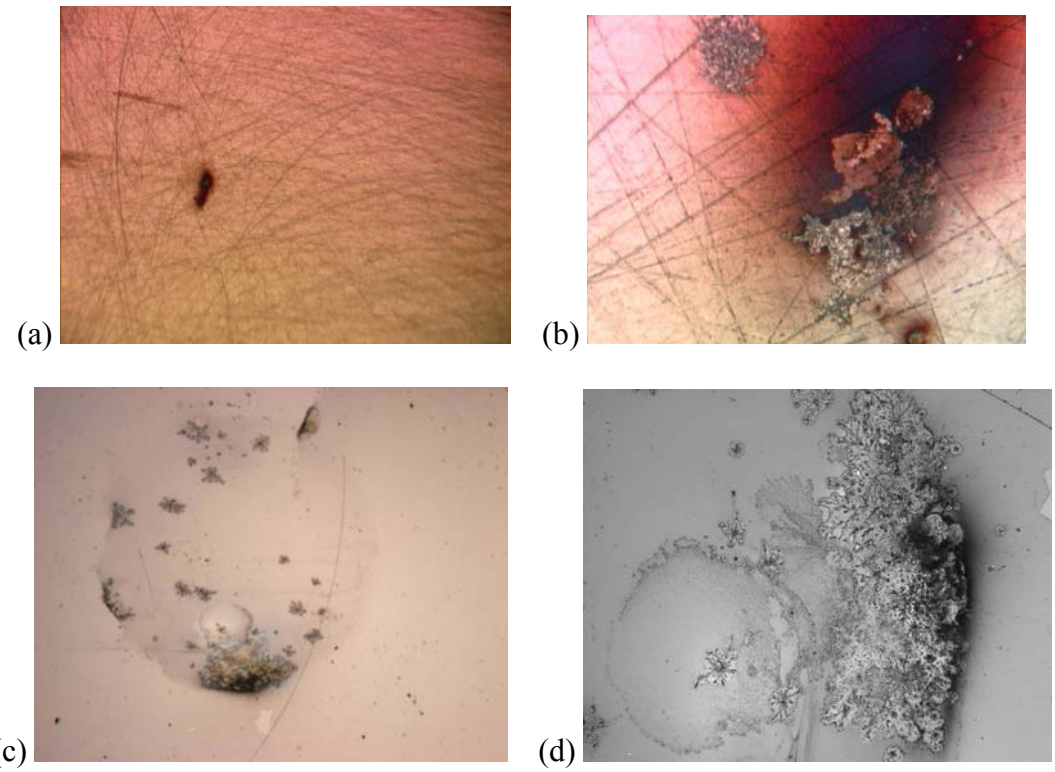

Figure 48. Optical microscope images of burn marks on the copper anode: (a) 5x and (b) 50x magnification. Images of the burn marks on the CNT surface taken using an optical microscope: (c) 5x, and (d) 20x magnification.

The images of the burn marks on the CNT surface resembled those presented by Manohara *et al.*[19] (Figure 15, page 33), where the markings were reported to be caused by arcing at high electric fields and resulted in the removal of CNTs from the substrate. In the case of this thesis, the exact cause of the damage is unclear. One possibility is that ionic impurities are desorbed from the film's surface as its temperature increases due to the emission current. At the point of arcing, either adsorbed ionic impurities on the surface or the CNTs themselves are ionized and destroyed, resulting in the transfer of enough energy to the copper anode to cause the burn marks and trip the high voltage supply. Plan-view SEM analysis of the marks of the CNT film's surface are shown in Figure 49. To remove the marks on the copper anode, it was polished with 4000 grit SiC sandpaper and metal polish, and rinsed in both acetone and methanol before the next sample was tested.

SEM analysis of the marked area on the CNT film's surface showed a loss of substrate height in the field emission area when compared with areas covered by the Teflon® spacer. Figure 50 shows images of an emission area damaged by the application of an electric field (although not from the CNT film grown at 1700^{o}C under 10^{-5} Torr vacuum for 0.5-hours with no post-growth annealing). The images were taken after cleaving the sample across the burn mark, and imaging the CNTs with the sample 45^{o} relative to the electron gun. The images show that CNTs were still discernable within the damaged emission area, and that in some locations the CNTs were completely destroyed.

(a)

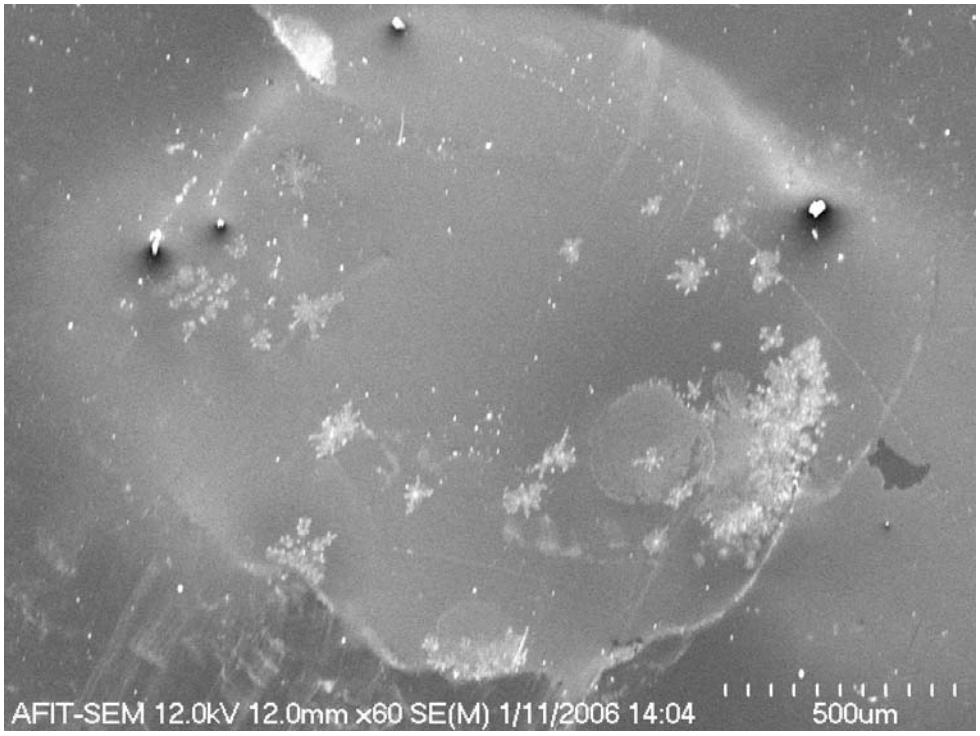

(b)

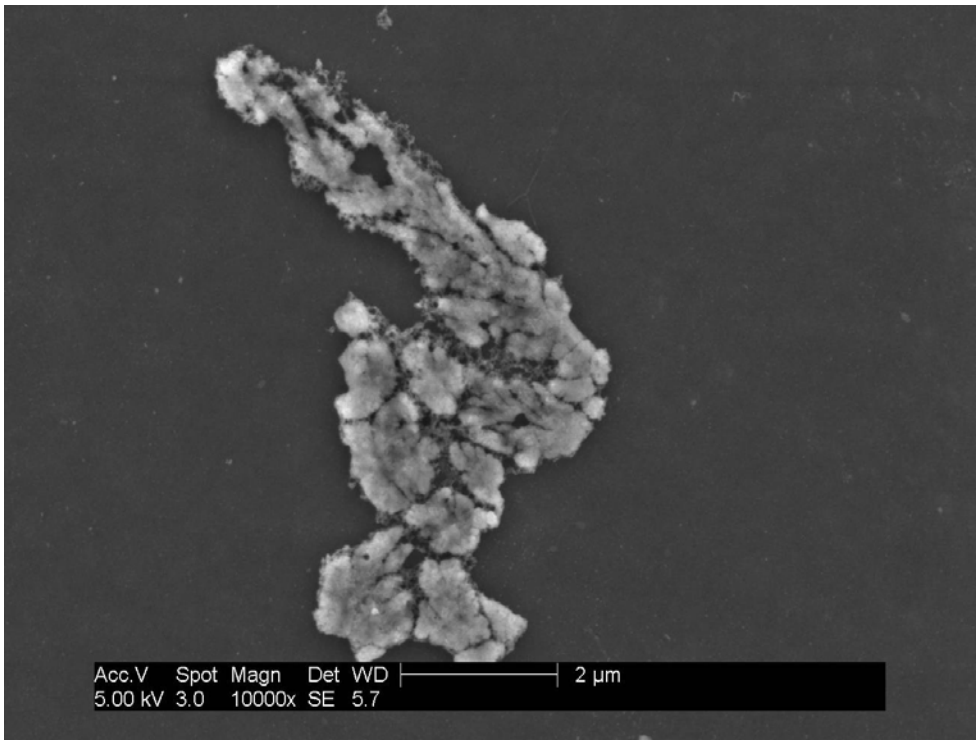

Figure 49. Plan-view SEM images of the burn marks on the CNT surface after six runs: (a) under 60x magnification showing the entire 1/16" emission area, and (b) a burn mark on the surface under 10,000x magnification.

(a)

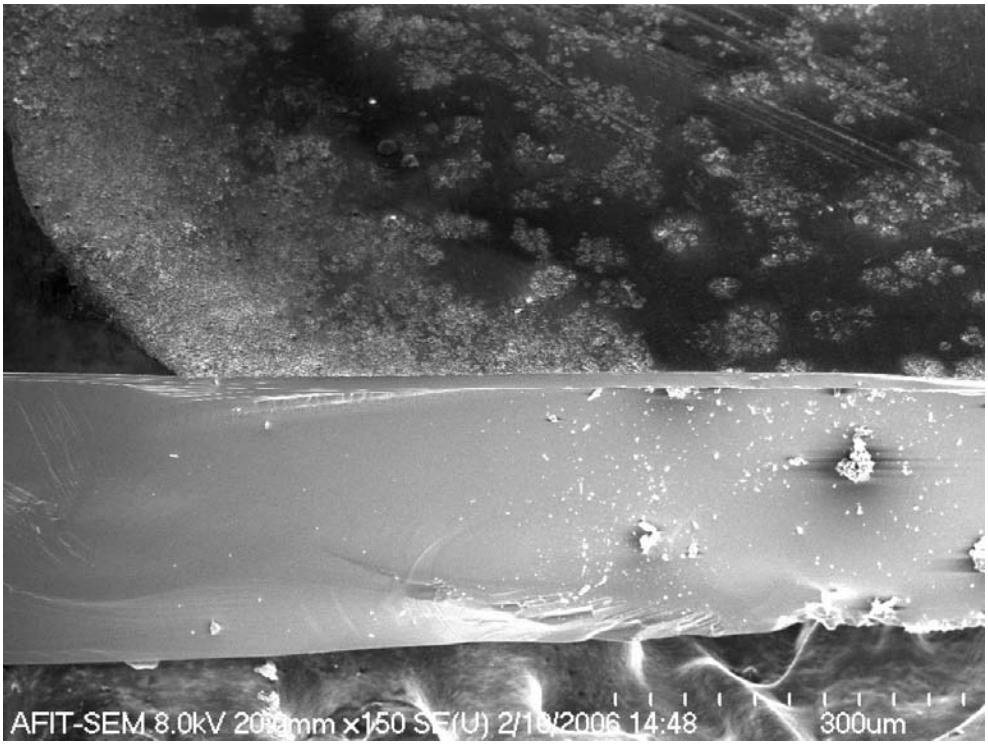

(b)

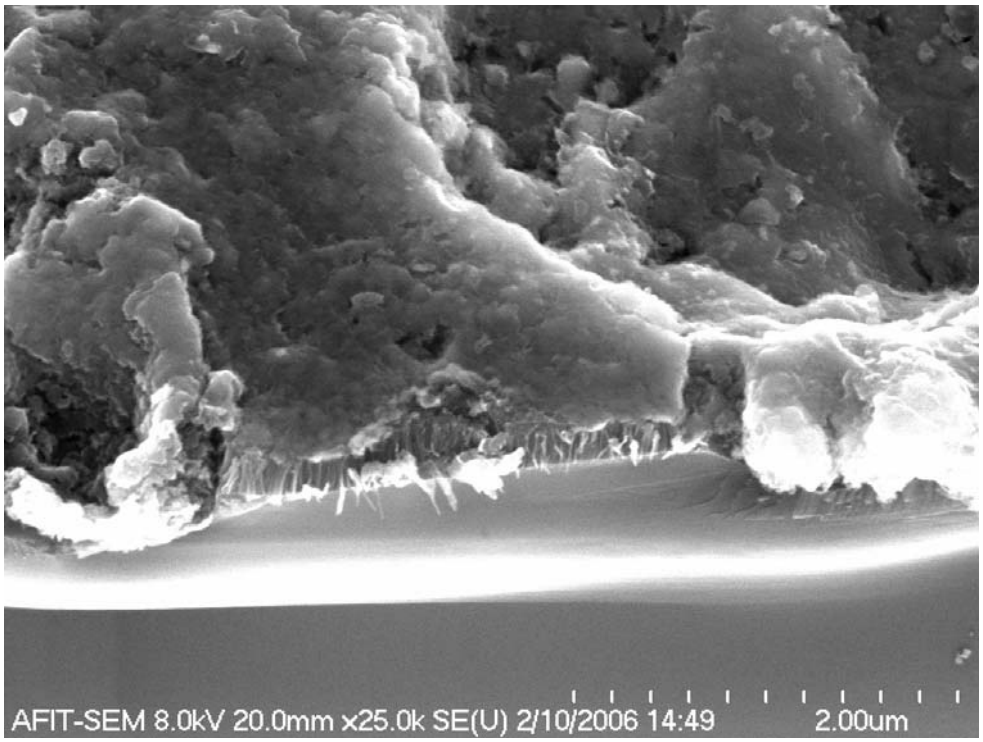

Figure 50. SEM images of burn marks on a CNT surface after multiple runs: (a) under 150x magnification showing a cleaved portion of the 1/16" emission area, and (b) within the damaged emission area under 25,000x magnification (45^{o} stage tilt).

The existence of ionic impurities on the CNT surface may contribute to the inconsistencies noted in the field emission data plotted in Figure 46, where the emission current dropped at several spots while the applied voltage was increased. The adsorbed ionic impurities likely decrease the work function at various spots on the emission surface, causing points with lower threshold fields (higher local emission currents) at some points on the surface. As the ionic impurities are desorbed, the emission current falls until the threshold field of the residual material is reached. Here, the residual material is assumed to be the CNT film, but could be the SiC substrate if the CNTs have been ionized off the sample. Further complicating the situation, the desorption of some impurities may result in reduced field screening effects on nearby CNTs or other surface impurities, resulting in an immediate replacement of the desorbed emission source; i.e. the film surface is dynamic under applied electric fields.

One major question is how much each arcing cycle degrades the emission surface. For this sample, no stable currents were registered in the sample after the sixth run, even though SEM analysis showed that much of the emission area was still intact after all six runs (Figure 49 (b)).

0.5-Hour Growth, 10^{-5} Torr, 1700^{o}C, Annealed for 10-minutes at 620^{o}C in flowing O_2:

Testing of the sample was performed at a vacuum pressure of 3.7×10^{-7} Torr. Due to the post-growth annealing, most of the Ta on the backside of the sample appeared to be gone. The removal of the Ta ohmic contact from the backside of the SiC sample greatly inhibits the ability of current to flow through the sample to the emission surface,

and reduces the likelihood of emission. Additionally, annealing the sample appears to have removed many of the CNTs on the surface.

Figure 51 shows an SEM image of the surface of a CNT film sample grown for 1-hour under 10^{-5} vacuum at 1700°C that had been annealed for 10-minutes at 620°C under flowing O_2, revealing that the entire CNT layer had been removed. Because the CNT film resulting from the 0.5-hour growth time is thinner as compared to the 1-hour growth sample, it likely has an increased vulnerability to the post-growth annealing step and therefore its removal from the SiC surface is not a surprise. The removal of the Ta is unusual, considering the melting point of Ta is far above the 620°C annealing temperature.

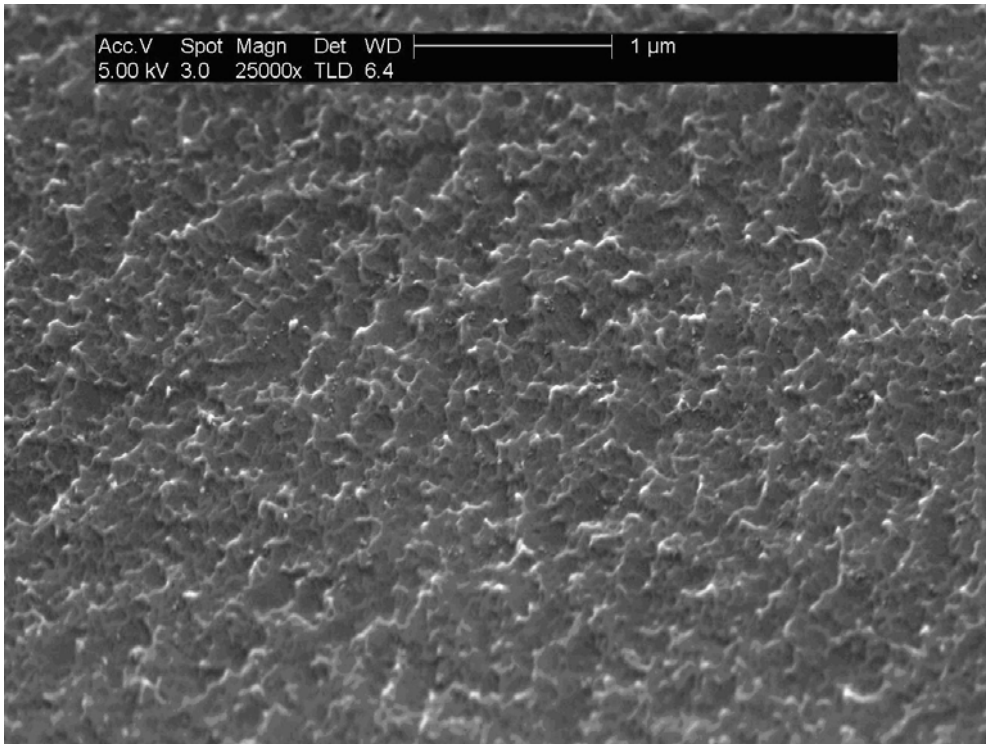

Figure 51. Resultant surface from a 10-minute anneal at 620°C under flowing O_2 on a CNT film grown for 1-hour under 10^{-5} vacuum at 1700°C, 25,000x magnification, SiC face unknown.

The ramping of the applied voltage caused repeated trips of the voltage supply, as trips occurred at 8.50, 8.00, 9.00, 7.50, and 8.20 V/μm. After the five trips of the power supply without observing any current, a current was recorded at 7.50, 7.80, 8.00, and 8.20 V/μm steps (denoted run 1, as it was the first run to provide usable data). The resulting data is plotted in Figure 52, showing a non-linear F-N plot, and a low maximum current density achieved. The collected current data for run 1 was highly unstable over time, with large voltage spikes observed. After the voltage supply registered a primary trip at the 8.20 V/μm level during run 1, no current was observed at any other voltage levels for subsequent runs.

After removing the sample from the sample holding apparatus, burn marks similar to those previously discussed were also noted on its substrate.

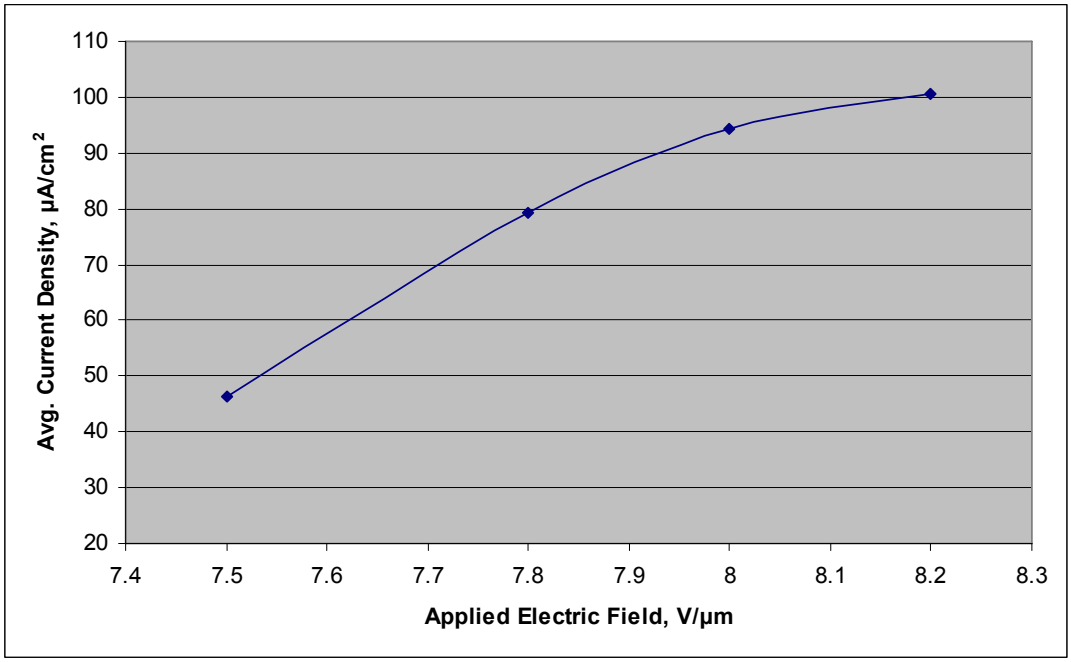

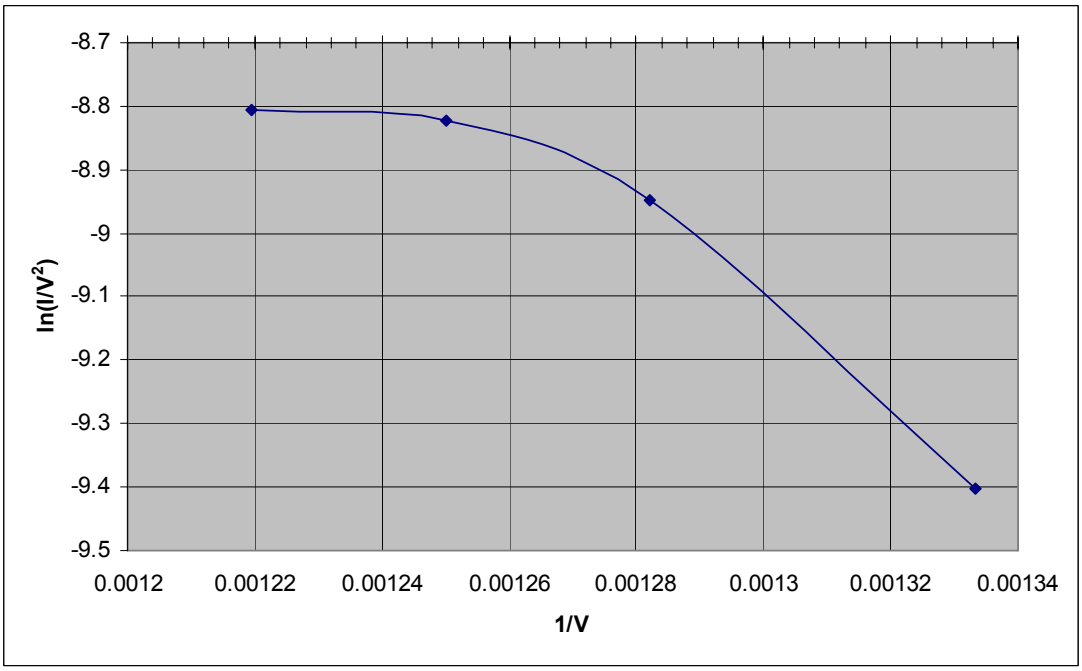

Figure 52. Data collected for 1 run on the CNT film grown at 1700°C under 10^{-5} Torr vacuum for 0.5-hours and annealed for 10-minutes at 620°C in flowing O_2.

0.5-Hour Growth, 10^{-3} Torr, 1700°C, Annealed for 10-minutes at 620°C in flowing O_2:

Testing of the sample was performed at a vacuum pressure of 6.2×10^{-7} Torr. The ramping of the applied voltage caused an initial trip of the voltage supply at 6.00 V/μm before any current was observed through the system. After this initial trip, four consistent runs were observed (denoted as runs 1 through 4, respectively). No current was measured in the system after the fourth run. The resulting data sets for the four runs are plotted in Figure 53.

As shown by the plotted field emission data, the initial run's maximum current density achieved was well below the values achieved for runs 2, 3, and 4. Run 1, and the initial run which did not result in a measurable current before tripping the power supply, are assumed to be conditioning steps resulting in the release of adsorbed impurities from the emission surface. The release of adsorbents alters the surface's field emission properties; however, the result of this release was unpredictable, as both increases and decreases in the maximum current density are observed for runs 1 through 4.

The overall maximum current density achieved with this sample was reasonably low compared to the 4.3 mA/cm^2 at 6.7 V/μm on first sample discussed (run 1), registering 794 μA/cm^2 at an applied electric field of 9.00 V/μm for the second run. The turn-on voltages for each run were: 6.40 V/μm (10.8 μA/cm^2), 6.20 V/μm (18.24 μA/cm^2), 6.00 V/μm (44.4 μA/cm^2), and 5.50 V/μm (36.1 μA/cm^2). Applied electric fields for stimulating the exact turn-on current (10 μA/cm^2) were not determined, as the lowest observed currents were not always low enough to equate to the turn-on current value.

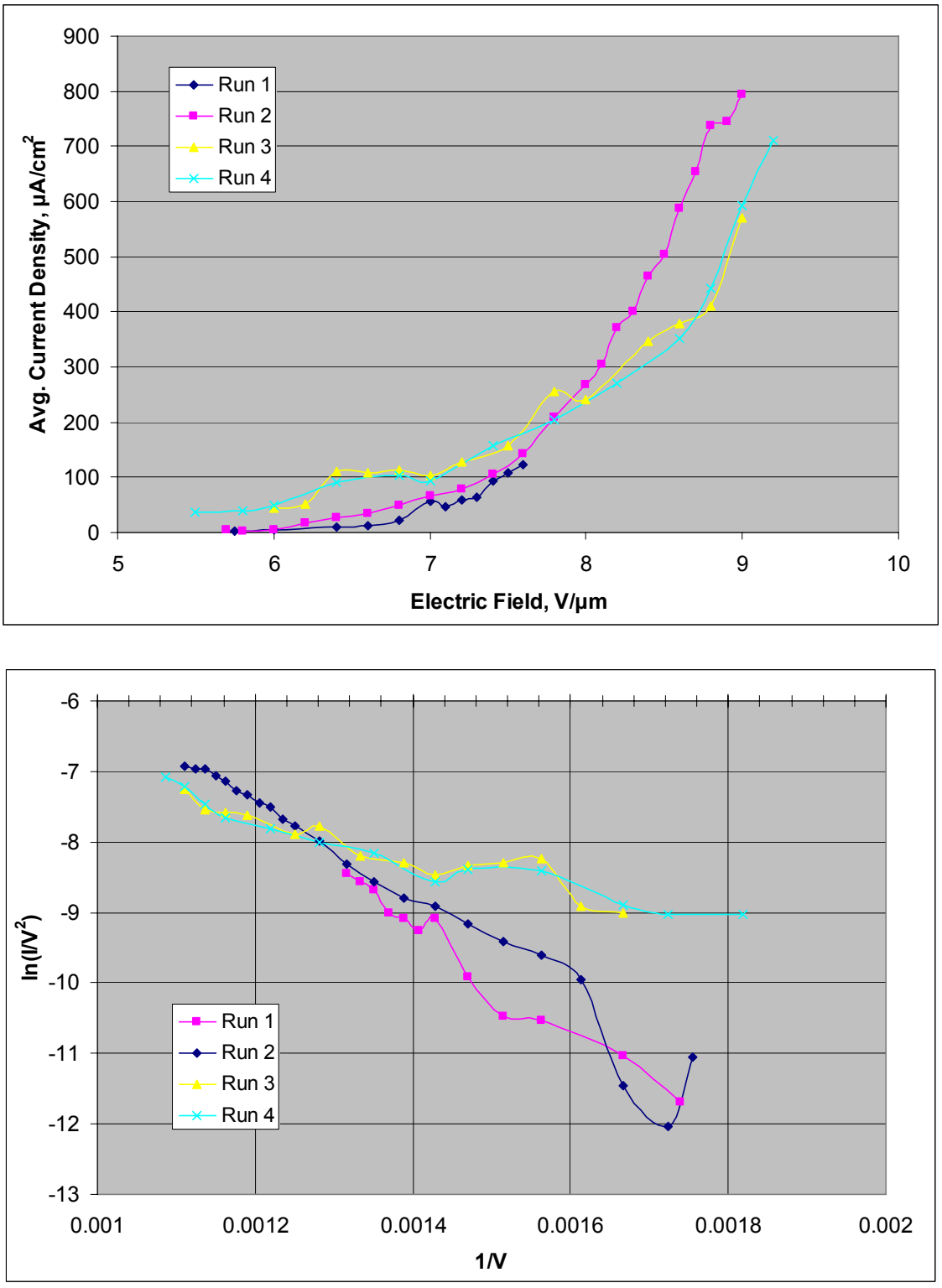

Figure 53. Field emission data for the CNT film grown at 1700°C under 10^{-3} Torr vacuum for 0.5-hours and annealed for 10-minutes at 620°C in flowing O_2.

Taking the slope of the collected data plotted in F-N format using a least squares fit, the field enhancement factor was calculated for each run to be 864.9, 903.1, 2483.4, and 2545.8 for runs 1, 2, 3, and 4, respectively. The field enhancement factor increased with each successive run.

The increasing field enhancement factor and decreasing turn-on voltages indicate that the sample's surface became rougher with each run. The release of adsorbents during each run left 'outcroppings' that experienced decreased field screening effects. With the applied electric field enhanced at the 'outcropping' points, the turn-on electric field level was decreased.

For each voltage step on the CNT film grown at 1700^{o}C under 10^{-3} Torr vacuum for 0.5-hours with a 10-minute anneal at 620^{o}C under flowing O_2, the average maximum deviation from the average current measured (for all recorded runs) was 51.8%. Although this value seems high, it includes errant current spikes. The data showed that the maximum deviations from the average decreased under relatively high (for the sample) applied electric fields. Run 3 showed the best stability using this figure of measure, with the average maximum deviation from the average for each voltage step only 35.8%.

The standard deviation was calculated for each group of data collected at each voltage step. Calculating the percentage the standard deviation (for each voltage step) represented with respect to the average for each voltage step, and averaging these values, it is seen that on average the standard deviation is 25.1% of the mean value for each voltage step. This value is double the value observed for the sample grown for 0.5-hours under 10^{-5} Torr vacuum conditions at 1700^{o} C with no post-growth annealing, which was

only 12.2%. This implies that this sample demonstrated comparably less stable currents. Run 3 proved to be the most stable run, with the corresponding value calculated to be 17.2%.

As with the previous samples discussed, burn marks were noted on both the copper anode and SiC/CNT sample after they were removed from the sample holding apparatus. Unlike all other samples tested, a dark material was noted on the side of the Teflon® sheet that was in contact with the CNT film. This dark material on the Teflon® spacer was accompanied by what appeared to be the removal of the CNTs from the SiC sample. Although SEM images were able to clarify this assumption, the top surface of the SiC sample appeared to be semi-transparent, indicating that the CNTs had been removed.

Figure 54 shows the material on the Teflon® spacer and the corresponding SiC sample from which the contamination originated. The dark tint within the 1/16th inch hole is due to the sheet's shadow on the disposable lab wipe positioned below to ensure a clean working surface.

The cause of the CNT film's adhesion to the Teflon® sheet is not known. One possibility is that the CNT fabrication run did not produce a CNT film as expected, forming a layer of unknown attributes (graphitic or amorphous carbon layers) on the SiC due to abnormalities in the growth procedure. Another possibility is that the annealing process damaged the CNTs enough to result in the film being poorly held to the SiC substrate.

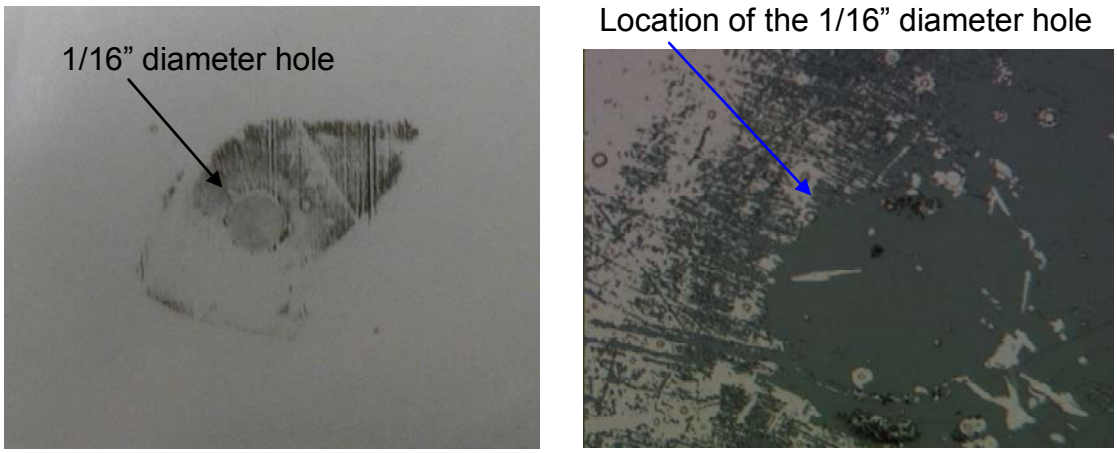

Figure 54. Images of the CNT film residue on the Teflon® spacer taken using a digital camera (left), and the corresponding CNT film taken using the optical microscope at 5x magnification (right).

0.5-Hour Growth, 10^{-3} Torr, 1700°C, No Post-Growth Annealing:

No current data was recorded for this sample. Repeated trips of the high voltage power supply occurred before any data could be collected on the sample. Field emission currents were observed for brief moments prior to the power supply tripping, but they were highly unstable and occurred before the software could be initiated to record the values observed on the multi-meter.

A CNT film grown at 1700°C under 10^{-3} Torr vacuum pressure for 0.5-hours that did not undergo post-growth annealing is shown in Figure 55. The cross-sectional view of the CNT film is achieved by taking a fresh cleave of the CNT/SiC sample. The SEM image shows that the CNT layer did indeed form on the SiC surface, and that the film’s top surface is highly similar to that of films grown under 10^{-5} Torr vacuum conditions. The SEM image did not confirm that the CNT film grown under the poorer vacuum conditions yielded a rougher surface or formed a less dense CNT layer.

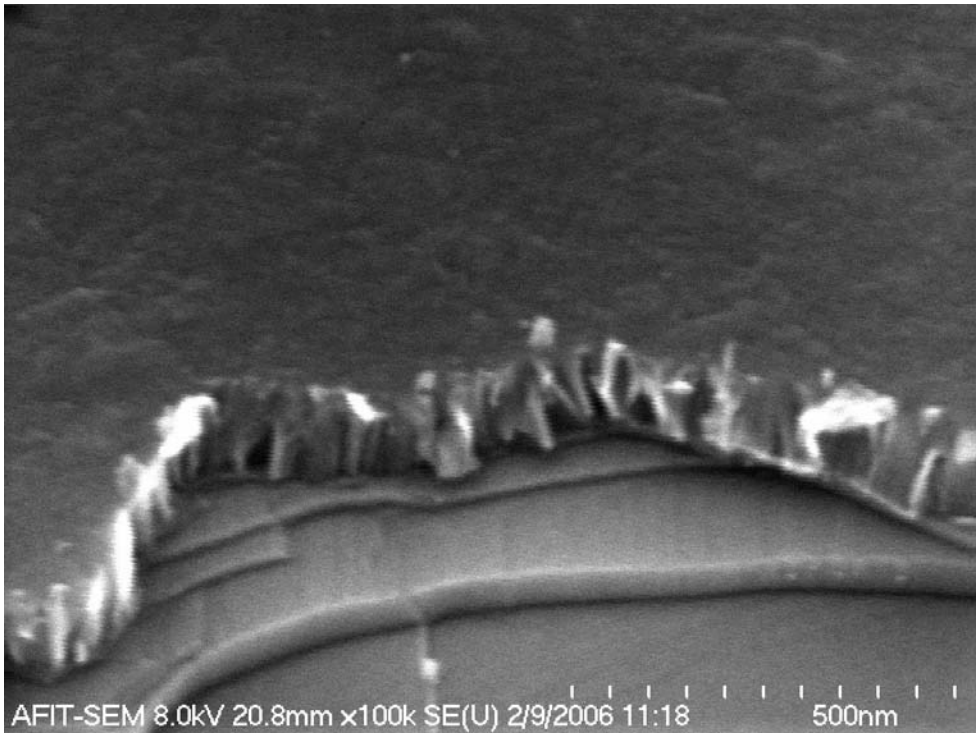

Figure 55. 100,000x magnification SEM image of a CNT film grown at 1700°C under 10^{-3} Torr vacuum pressure for 0.5-hours that did not undergo post-growth annealing (45° stage tilt).

3-Hour Growth, 10^{-5} Torr, 1700°C, No Post-Growth Annealing:

Unlike the previous test results discussed, no conditioning was necessary to achieve recordable emission steps. Four runs were observed and recorded (denoted as runs 1 through 4), and the resulting data is shown in Figure 56.

The current vs. applied electric field plot changed characteristics for each run in Figure 56. From run 1 to 3, the turn-on electric field increased, and the maximum current density decreased. With only two voltage levels recorded for run 4, its results are not discussed, as there is not enough data to ascertain a trend in its performance. The turn-on electric fields were measured as 5.50 V/μm (9.61 μA/cm^2), 7.00 V/μm (8.98 μA/cm^2), and 7.00 V/μm (11.71 μA/cm^2), for runs 1, 2, and 3, respectively. The maximum current

density of runs 1 through 3 were 600 μA/cm^2 (at 9.50 V/μm), 383 μA/cm^2 (at 10.00 V/μm), and 181 μA/cm^2 (at 10.00 V/μm), respectively.

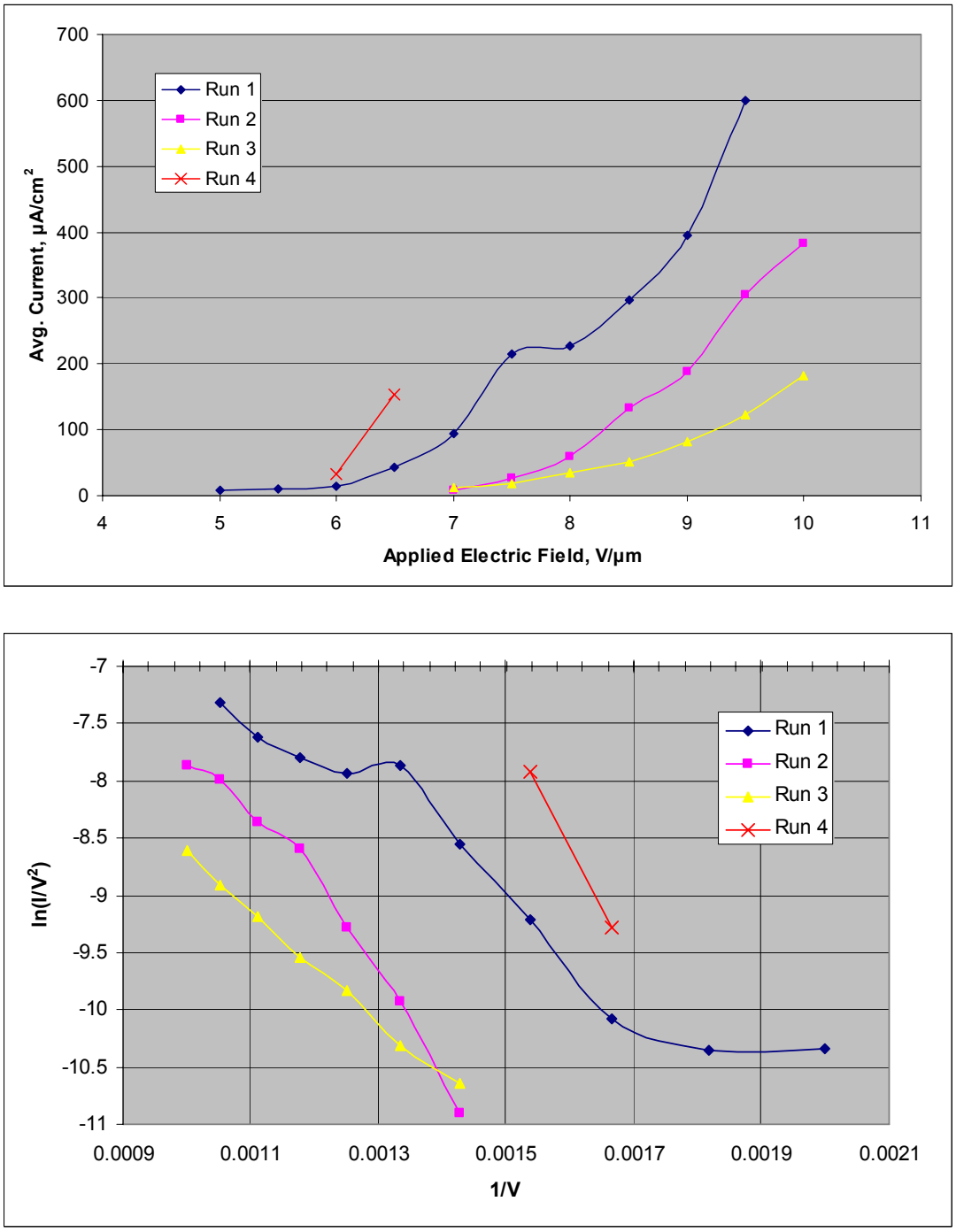

Figure 56. Field emission data for the CNT film grown at 1700°C under 10^{-5} Torr vacuum for 3-hours and with no post-growth annealing.

Extracting the slope of each run plotted in F-N format, the field enhancement factor for runs 1 through 3 was calculated to be 1789.5, 921, and 1374.4, respectively. Thus, the field enhancement factor decreased after the initial run that achieved the highest maximum current density.

For each voltage step on the CNT film grown at 1700^{o}C under 10^{-5} Torr vacuum for 3-hours with a no post-growth annealing, the average maximum deviation from the average current measured (for all recorded runs) was 63.5%. Although this value seems high, it includes errant current spikes. The data showed that the maximum deviations from the average decreased under relatively high (for the sample) electric field steps.

The standard deviation was calculated for each group of data collected at each voltage step. Calculating the percentage the standard deviation (for each voltage step) represented with respect to the average for each voltage step, and averaging these values, it is seen that on average the standard deviation is 21% of the mean value for each step.

As with the previous samples discussed, burn marks were noted on both the copper anode and SiC/CNT sample after they were removed from the sample holding apparatus.

A CNT film grown at 1700^{o}C under 10^{-5} Torr vacuum pressure for 3-hours that did not undergo post-growth annealing is shown in Figure 57. The film pictured in Figure 57 greatly resembles the image pictured in Figure 55, making comparisons between their respective surface topologies and densities difficult. An SEM image of the top surface of the CNT film under the same stage tilt as the image in Figure 57 is shown in Figure 58. In the image, a level of surface roughness can be seen, but not quantified.

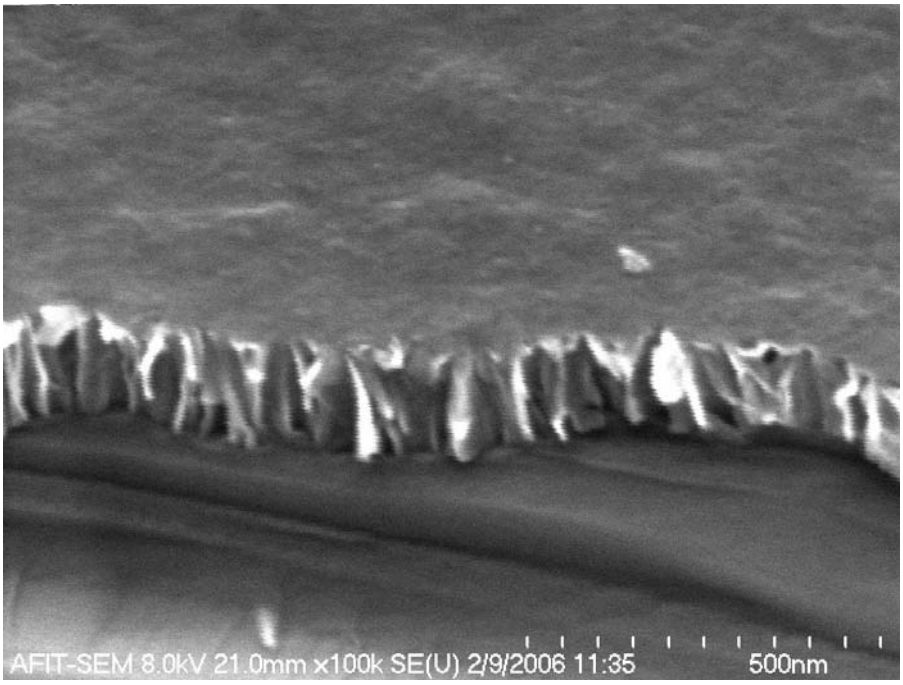

Figure 57. 100,000x magnification SEM image of the cross section of a CNT film grown at 1700°C under 10^{-5} Torr vacuum pressure for 3-hours that did not undergo post-growth annealing (45° stage tilt).

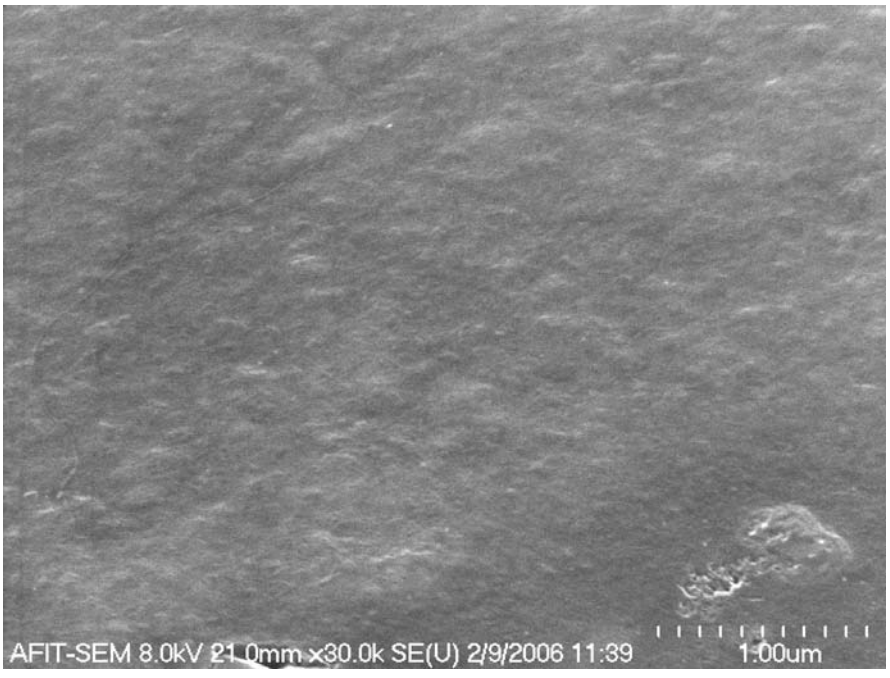

Figure 58. 30,000x magnification SEM image of the top surface of a CNT film grown at 1700°C under 10^{-5} Torr vacuum pressure for 3-hours that did not undergo post-growth annealing (45° stage tilt)

3-Hour Growth, 10^{-5} Torr, 1700°C, Annealed for 10-minutes at 620°C in flowing O_2:

Testing of the sample was performed at a vacuum pressure of 3.4×10^{-7} Torr. Initially, no current was observed in the system prior to a primary trip from the high voltage power supply at 5.00 V/μm. Following the initial primary trip from the voltage supply, a current was observed in the system beginning at 4.60 V/μm. After recording data at 4.60 V/μm, only three more electric field steps were recorded before the power supply tripped at 4.9 V/μm. This run did not result in any well trended or stable data, and thus is not further discussed. After this second tripping of the power supply, four successive runs of solid, well-trended data were collected, and are shown in Figure 59 (denoted as runs 2 through 5, respectively; all performed on the same spot on the sample).

From the plotted data, one sees that by run 5, the turn-on electric field was considerably higher than that of the second run. The turn-on voltage for runs 2 through 5 was 3.20 V/μm (16.7 μA/cm^2), 3.50 V/μm (9.7 μA/cm^2), 3.20 V/μm (20.6 μA/cm^2), and 5.20 V/μm (19.5 μA/cm^2), respectively. The maximum current densities for runs 2 through 5 were 330 μA/cm^2 at 4.70 V/μm, 411 μA/cm^2 at 5.20 V/μm, 1762 μA/cm^2 at 5.90 V/μm, and 2117 μA/cm^2 at 5.90 V/μm respectively. Based on the plots, it is concluded that a form of surface conditioning occurs after each voltage run, which changes the surface topology and film's field emission properties.

By extracting the slopes of F-N curves, the field enhancement factor for runs 2 through 5 was calculated to be 2663, 1645, 2638, and 369, respectively. Thus, the field enhancement factor decreased by the final run compared to that of the initial run. Unlike the previous samples, the maximum current density increased with each successive run.

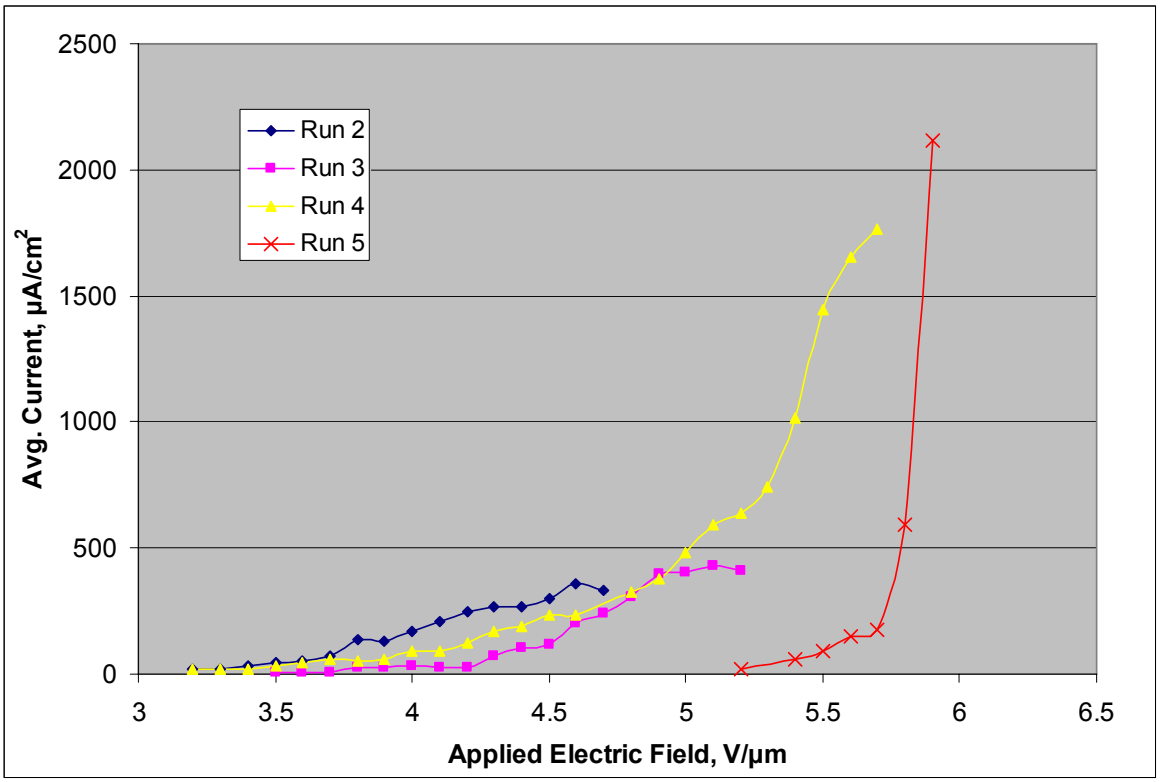

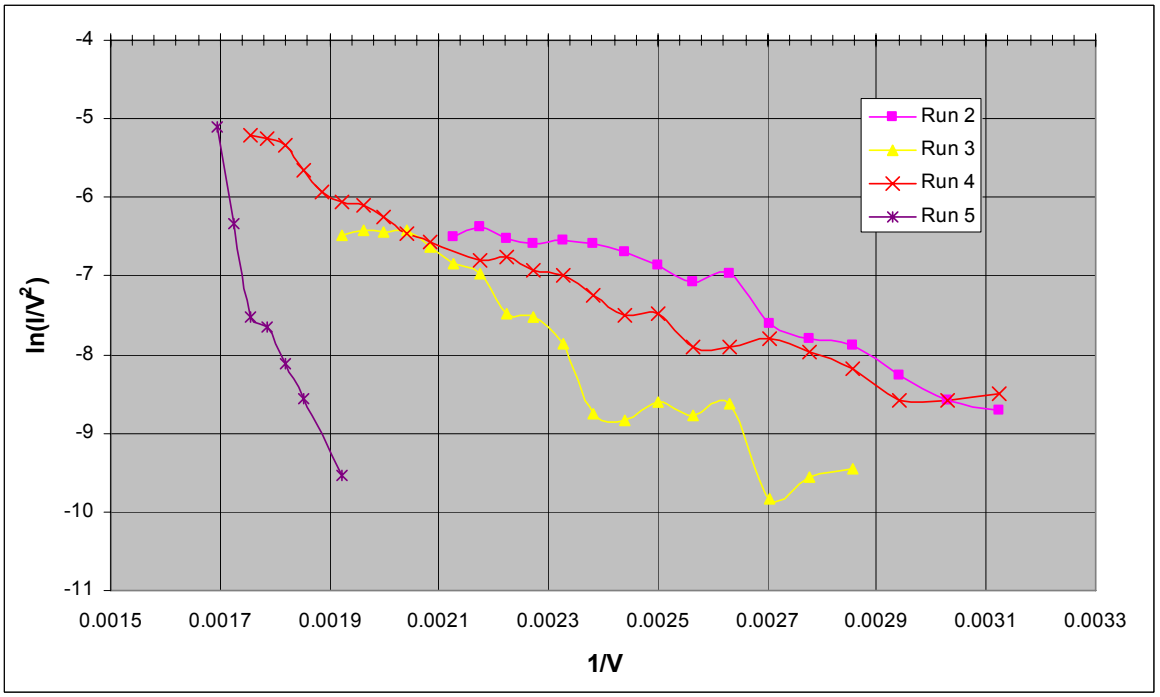

Figure 59. Field emission data for the CNT film grown at 1700°C under 10^{-5} Torr vacuum for 3-hours and annealed for 10-minutes at 620°C in flowing O_2.

For each voltage step on the CNT film grown at 1700°C under 10^{-5} Torr vacuum for 3-hours and annealed for 10-minutes at 620°C in flowing O_2, the average maximum deviation from the average current measured (for all recorded runs) was 49.9%. Run 3 showed the best stability using this figure of measure, with the average maximum deviation from the average for each voltage step only 23.52%.

As was done for the previous samples, the standard deviation was calculated for each group of data collected at each voltage step. Calculating the percentage the standard deviation (for each voltage step) represented with respect to the average for each voltage step, and averaging these values, it is seen that on average the standard deviation is 26.6% of the mean value for each voltage step. Specifically, run 3 was the most stable run, with the corresponding value calculated to be 12%.

One major change in the emission current was recorded and is illustrated in Figure 60. The average of the first portion was calculated to be 1.916 mA/cm^2, while the average of the second portion was calculated to be 0.14 mA/cm^2. The drop in emission current is assumed to be due to the emission surface changing in some manner. Because the alteration occurred during the application of a strong electric field (5.80 V/μm), the change in properties is concluded to be due to the electric field causing either the desorption of surface impurities or damage to the CNTs on the surface. Because the current decreased, another possibility is that the applied electric field caused the destruction of 'outcroppings' on the emission surface, resulting in increased field screening effects between the remaining emission points. Another assumption is that the desorption of surface impurities altered the work function of emission points on the surface, raising the fields necessary for emission and decreasing the emission current.

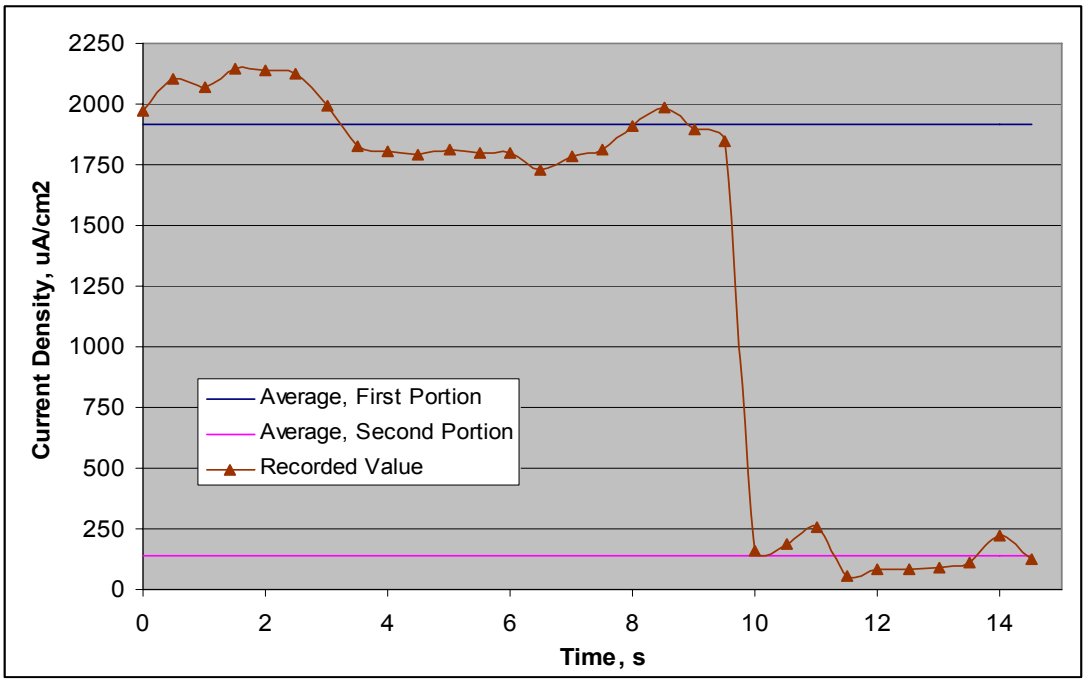

Figure 60. Stability plot, 5.80 V/µm applied to a CNT film grown at 1700°C under 10^{-5} Torr vacuum for 3-hours and annealed for 10-minutes at 620°C in flowing O_2.

As with the previous samples discussed, burn marks were noted on both the copper anode and SiC/CNT sample after they were removed from the sample holding apparatus.

3-Hour Growth, 10^{-3} Torr, 1700°C, No Post-Growth Annealing:

Testing of the sample was performed at a vacuum pressure of 1.0×10^{-6} Torr. Initially, no current was observed in the system prior to a primary trip from the high voltage power supply at 8.00 V/µm. Following the initial primary trip from the voltage supply, six successive runs were recorded (denoted as runs 1 through 6, respectively), after which no current was recorded at additional voltage steps. The data recorded from the final two runs was noisy and showed no trends, and therefore was omitted from further analysis. The data collected from runs 1 through 4 is shown in Figure 61.

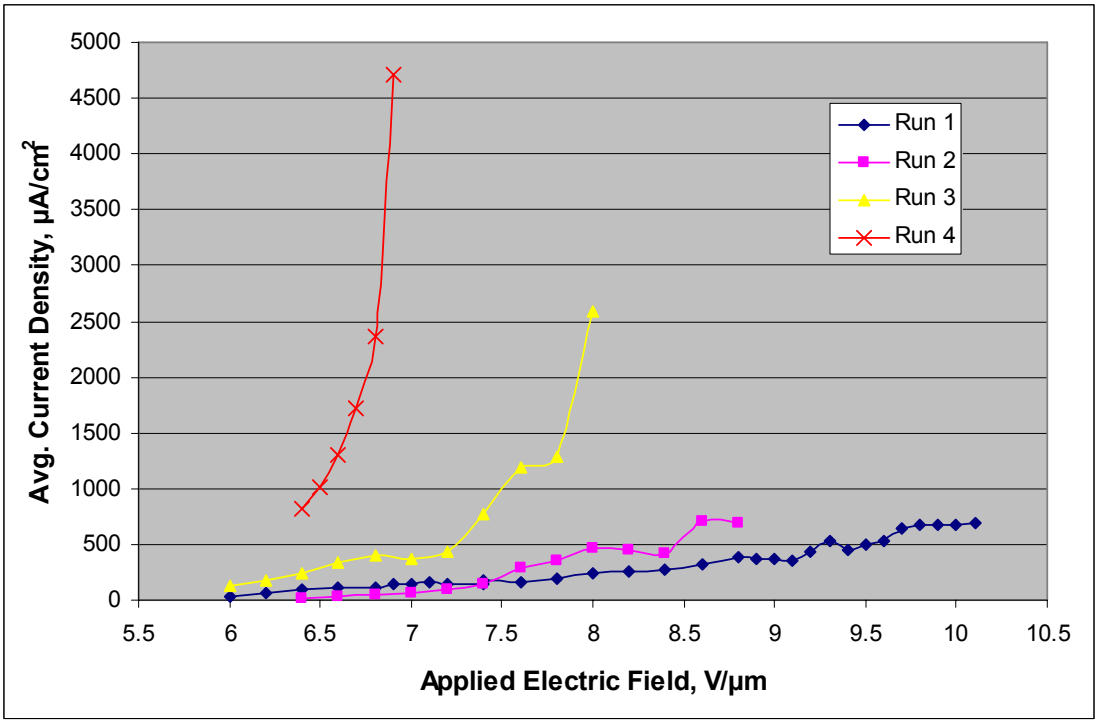

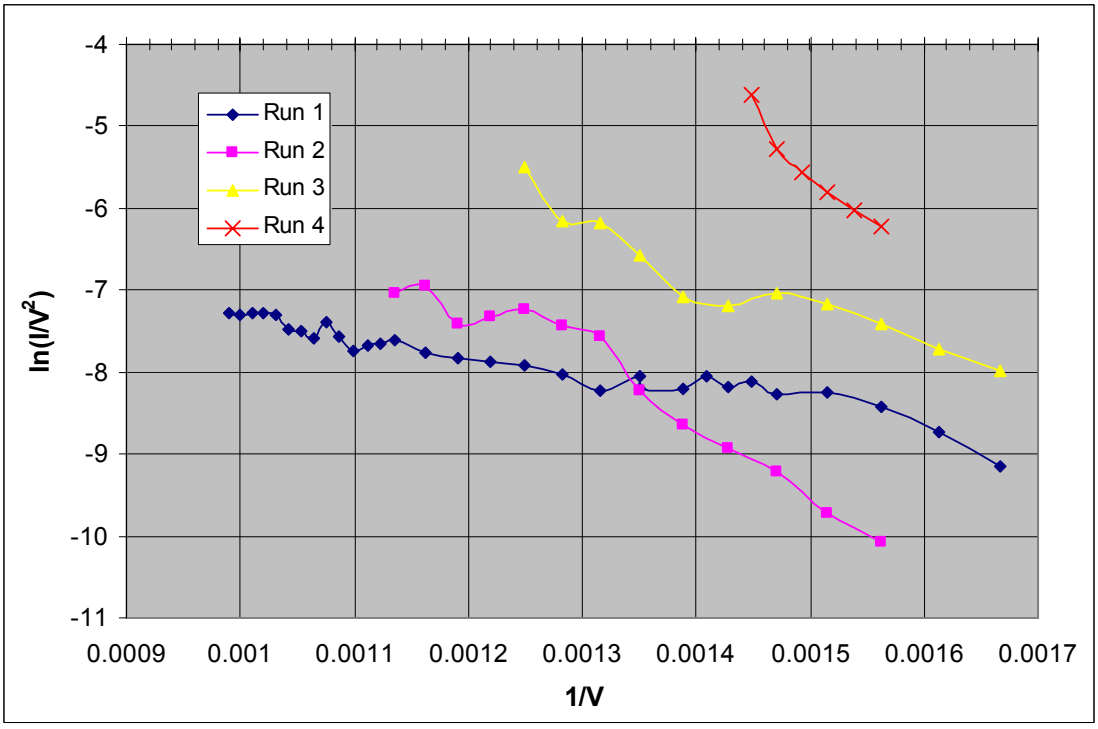

Figure 61. Field emission data for the CNT film grown at 1700°C under 10^{-3} Torr vacuum for 3-hours and with no post-growth annealing.

From the plotted data, one sees that for each consecutive run, the slope of the current vs. applied electric field and the maximum current density increases. Clearly, the sample's surface is improving through what must be assumed to be the desorption of impurities from the emission surface.

The turn-on voltage for runs 1 through 4 was 6.00 V/μm (37.7 μA/cm^2), 6.40 V/μm (17 μA/cm^2), 6.00 V/μm (123 μA/cm^2), and 6.40 V/μm (814 μA/cm^2), respectively. Although the turn-on values for runs 3 and 4 were much higher than the desired 10 μA/cm^2 criteria, interpolation of the collected data was not successful. The maximum current densities for runs 1 through 4 were 690 μA/cm^2 at 10.10 V/μm, 685 μA/cm^2 at 8.80 V/μm, 2595 μA/cm^2 at 8.0 V/μm, and 4709 μA/cm^2 at 6.90 V/μm respectively.

Extracting the slope of each run plotted in F-N format, the field enhancement factor for runs 1 through 4 was calculated to be 3027, 867, 1296, and 496, respectively. The field enhancement factor decreased by the final run as compared to value from the initial run, indicating a decrease in surface roughness.

For each voltage step recorded for this sample, the average maximum deviation from the average current measured (for all recorded runs) was 48.4%. Runs 3 and 4 showed the best stability using this figure of measure, with the average maximum deviation from the average for each voltage step only 23% and 27.2%, respectively.

The standard deviation was calculated for each group of data collected at each voltage step. Calculating the percentage the standard deviation (for each voltage step) represents with respect to the average for each voltage step, and averaging these values, it is seen that on average the standard deviation is 20.5% of the mean value for each voltage

step. Runs three and four were the most stable, with the corresponding values calculated to be 12.6% and 13.1%, respectively.

As with the previous samples discussed, burn marks were noted on both the copper anode and SiC/CNT sample after they were removed from the test apparatus.

A CNT film grown at 1700^{o}C under 10^{-3} Torr vacuum pressure for 3-hours that did not undergo post-growth annealing is shown in Figure 62. The SEM image shows that the CNT layer formed on the SiC surface, and has a top surface that is similar to that of films grown under 10^{-5} Torr vacuum conditions. The SEM image did not confirm that the CNT film grown under the poorer vacuum conditions yielded a rougher surface or that a less dense CNT array formed.

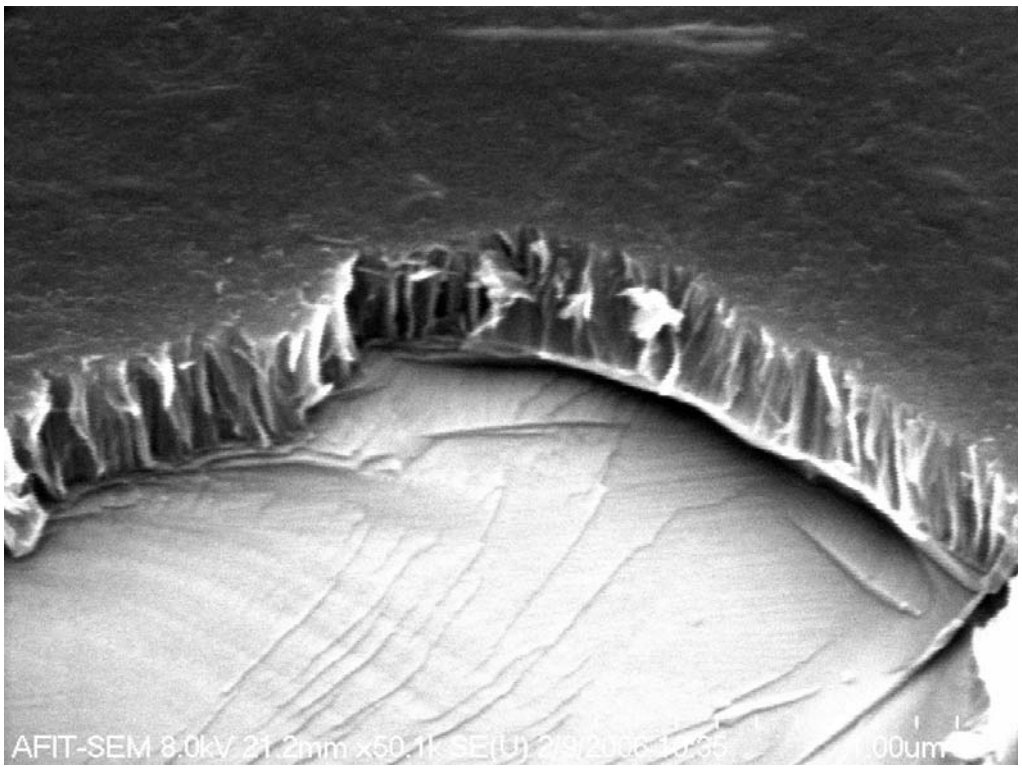

Figure 62. 50,000x magnification SEM image of a CNT film grown at 1700^{o}C under 10^{-3} Torr vacuum pressure for 3-hours that did not undergo post-growth annealing (45^{o} stage tilt).

3-Hour Growth, 10^{-3} Torr, 1700°C, Annealed for 10-minutes at 620°C in flowing O_2:

Testing of the sample was performed at a vacuum pressure of 6.4×10^{-7} Torr. Initially, no current was observed in the system prior to primary trips of the power supply at 30.00 V/μm, 38.00 V/μm, 48.00 V/μm, and 48.00 V/μm. Following the initial trips from the voltage supply, six runs were recorded (denoted as runs 1 through 6, respectively), after which no further currents were recorded. The data collected from runs 1 through 6 are shown in Figure 63.

The turn-on voltage for runs 4 and 6 was 13.00 V/μm (25 $\mu A/cm^2$), and 12.0 V/μm (21 vA/cm^2), respectively. The maximum current density for runs 4 and 6 were 1.633 mA/cm^2 at 18.0 V/μm, and 1.825 mA/cm^2 at 17.0 V/μm, respectively.

Because of the non-linear nature of the F-N plots for runs 4 and 6, only the final portion of the plotted data was used to calculate the field enhancement factor. Figure 64 shows the upper linear portion of the plotted F-N for runs 4 and 6 from Figure 63. Extracting the slope of runs 4 and 6 in Figure 64 using the least squares fit approach, the field enhancement factor was calculated to be 8987, and 977, respectively. Thus, the field enhancement factor decreased from the fourth to sixth run.

For each voltage step on the CNT film grown at 1700°C under 10^{-3} Torr vacuum for 3-hours and annealed for 10-minutes at 620°C in flowing O_2, the average maximum deviation from the average current measured (for all recorded runs) was 50.3%. Run 4 showed the best stability using this figure of measure, with the average maximum deviation from the average for each voltage step only 12.8%.

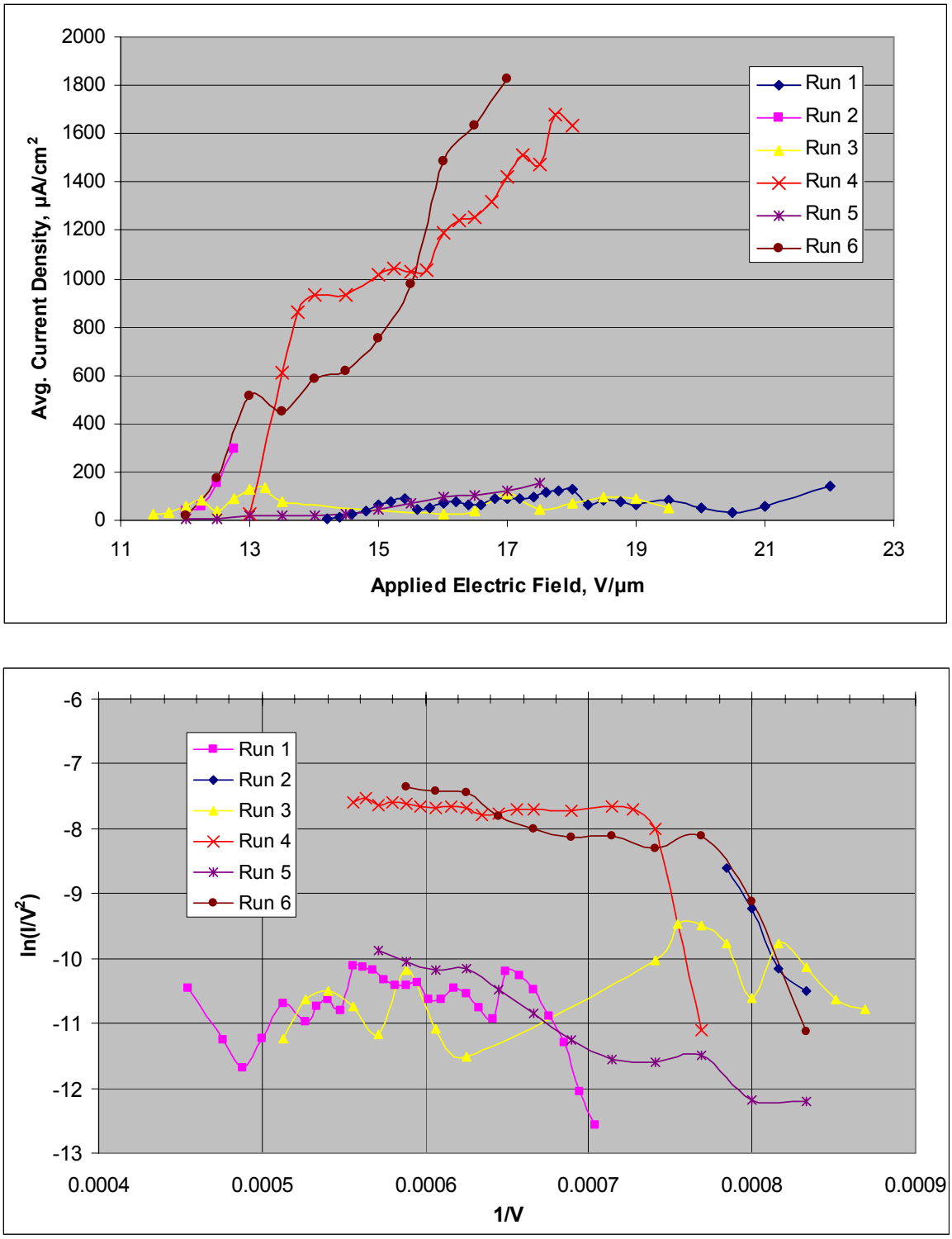

Figure 63. Field emission data for the CNT film grown at 1700°C under 10^{-3} Torr vacuum for 3-hours and annealed for 10-minutes at 620°C in flowing O_2.

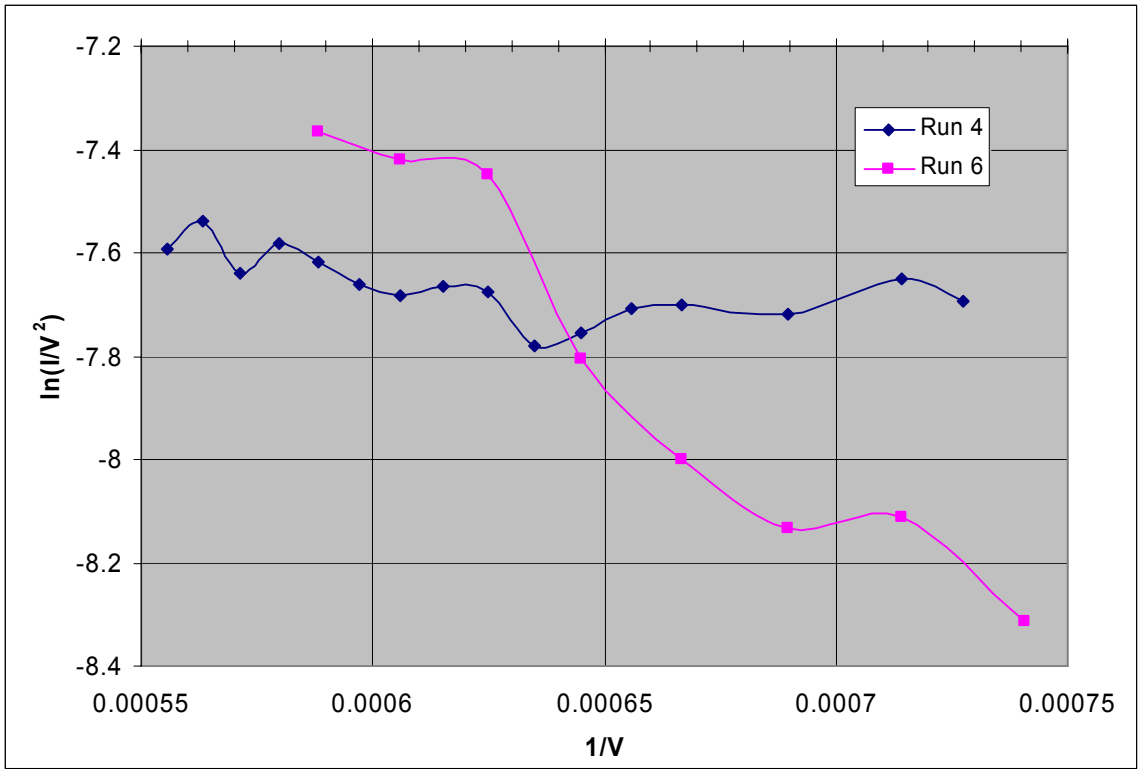

Figure 64. Linear portion of the F-N data plotted in Figure 63 for the CNT film grown at 1700°C under 10^{-3} Torr vacuum for 3-hours and annealed for 10-minutes at 620°C in flowing O_2.

As was done for the previous samples, the standard deviation was calculated for each group of data collected at each voltage step. Calculating the percentage the standard deviation (for each voltage step) represented with respect to the average for each voltage step, and averaging these values, it is seen that on average the standard deviation is 26.4% of the mean value for each voltage step (taking into account all runs). For run 4, this value was only 6.3%.

As with the previous samples discussed, burn marks were noted on both the copper anode and SiC/CNT sample after its removal from the test apparatus.

5-Hour Growth, 10^{-5} Torr, 1700^{o}C, No Post Growth Annealing:

No data was recorded for this sample. Testing resulting in repeated trips of the voltage supply in the 10.0 to 20.0 V/μm range without any stable currents observed on the multi-meter.

4.3.2 Comparison of Samples Tested

Table 5 lists the minimum turn-on electric field, along with a description of any possible trend shown over successive runs, for each of the 9 samples tested. From this data, the sample grown at 1700^{o}C under 10^{-5} Torr vacuum pressure for 0.5-hours with no post-growth annealing showed the lowest turn-on electric field. The table also shows that the predominant trend among all samples was that the turn-on electric field increased with consecutive runs. The increase in turn-on electric fields is likely caused by two reasons: the desorption of ionic impurities possessing lower work functions than the residual CNT surface; or the alteration of the surface topology due to the application of electric fields, such that any 'outcroppings' are destroyed by arc discharge (explosive emission). This 'outcropping' destruction leaves a smoother surface where the remaining 'outcroppings' protrude less above the substrate and therefore suffer from increased field screening effects. The 'outcropping' destruction claim is supported in part by the visible markings on the copper anode and CNT film after testing.

Table 5. Minimum turn-on electric fields.

Growth Time (hours)	Growth Pressure (Torr)	Post Growth Processing: Anneal Time/Temperature (minutes / ^{o}C)	Minimum Turn-On Electric Field (V/μm / μA/cm^2)	Trend Shown Over Successive Runs
0.5	10^{-5}	N/A	3.0 / 54.8	Increased with each run
0.5	10^{-5}	10 / 620	7.5 / 46.5	No trend, only 1 run of data
0.5	10^{-3}	N/A	No data	No data
0.5	10^{-3}	10 / 620	5.5 / 36.1	Decreased with each run
3	10^{-5}	N/A	5.5 / 9.61	Increased with each run
3	10^{-5}	10 / 620	3.20 / 16.7	Increased by the final run
3	10^{-3}	N/A	6.0 / 37.7	Remained stable
3	10^{-3}	10 / 620	13.0 / 25	Remained stable
5	10^{-5}	N/A	No data	No data

Because adsorbents adhering to the top layer of the CNT film may possess lower work functions and therefore possess lower turn-on electric field properties, one would presume they would make the more ideal emission source; this is not the case, however, as the adsorbed molecules do not possess the requisite attributes of an ideal field emitter as discussed in section 2.2. Recall that ideal field emission materials are highly conductive and stable, have a high aspect ratio, and have nano-scale diameters. An emission point without high conductivity and suitable thermal stability properties will be destroyed due to resistive heating during emission.

The data in Table 5 show that the post-growth annealing process does not cause a predictable increase or decrease in the turn-on electric field when compared with the corresponding non-annealed sample. The same post-growth processing recipe will likely have different impacts on the samples grown with different parameters. The 0.5-hour

growth samples, for instance, will be affected differently by the anneal than the thicker CNT layer of the 3-hour growth samples. The damage to the 0.5-hour growth samples, when compared to the 3-hour growth samples, is likely more extensive and goes beyond solely opening the CNT tips. This more extensive damage likely degrades the conductivity of the individual CNTs. The data gathered for the sample grown at 1700^{o}C under 10^{-5} Torr vacuum pressure for 0.5-hours and annealed for 10-minutes at 620^{o}C after growth cannot be used in this discussion, as the Ta ohmic contact was annealed off the sample due to unknown reasons.

The maximum current density achieved by each of the nine samples tested, along with a general description these values observed over successive runs, is listed in Table 6. The data show that the maximum current density was from the sample growth at 1700^{o}C under 10^{-3} Torr vacuum pressure for 3-hours and with no post-growth annealing, which achieved 4.71 mA/cm^2 at 6.9 V/μm. Three of the five samples resulting in noticeable trends between runs showed that the maximum current density increased with successive runs, while two of the five samples showed a decrease with successive runs. The two samples that decreased with successive runs were both samples that did not receive post-growth annealing. This finding contradicts the presumed trend that the samples undergoing the post-growth annealing would be more susceptible to damage from the applied electric fields.

The lack of trends in this data shows that the samples' initial surfaces may have contained different amounts and types of adsorbed ionic impurities, which may have improved or worsened the sample's field emission characteristics. Mitchel *et al.* [13] reported that X-ray photoelectron spectroscopy (XPS) analysis of a CNT film grown on

the C-face of SiC at 1700°C for 0.5-hours showed no Si or SiO_2 in the film, but that graphitic carbon and small amounts of oxygen were found. Further analysis is necessary to characterize the type and amounts of adsorbents on the surfaces of the CNT films.

Table 6. Maximum current densities.

Growth Time (hours)	Growth Pressure (Torr)	Post Growth Processing: Anneal Time/Temperature (minutes / °C)	Maximum current density (μA/cm^2 / V/μm)	Trend Shown Over Successive Runs
0.5	10^{-5}	N/A	4247 / 6.7	Decreased drastically
0.5	10^{-5}	10 / 620	100.7 / 8.20	No trend, only 1 run of data
0.5	10^{-3}	N/A	No data	No data
0.5	10^{-3}	10 / 620	794 / 9.0	No trend -- increased, decreased, and increased
3	10^{-5}	N/A	600 / 9.50	Decreased with each run
3	10^{-5}	10 / 620	2117 / 5.9	Increased drastically
3	10^{-3}	N/A	4709 / 6.9	Increased drastically
3	10^{-3}	10 / 620	1825 / 17.0	Slightly increased
5	10^{-5}	N/A	No data	No data

The electric breakdown that occurs when the power supply registers a current overload may have different effects on the emission surfaces of the different samples tested. Comparing the test data shows that electric breakdown did not occur at identical electric field strengths for each sample, indicating that different field strengths are needed for different types or amounts of adsorbed ionic impurities to be removed from the surface or for CNTs to be destroyed. It is postulated that the sample surfaces undergo unpredictable changes that alter the field emission behavior when electric breakdown (power supply current overload) occurs. The findings of a dynamic field emission

surface corresponds to the findings of Zhirnov *et al.* [34], where the destruction of a non-CNT emission tip was noted during field emission (section 2.5, page 43).

The calculated field enhancement factors for the consecutive runs on the samples tested are shown in Table 7. The table shows that the field enhancement factor decreased over successive runs for all but one sample. A high field enhancement factor is desirable for an emission surface, as it equates to a lower applied electric field necessary for field emission. The field enhancement factor is directly related to the surface topology of a sample, and thus a change in its value reflects a change in the sample's surface topology. In general, an increasing field enhancement factor equates to increasing surface roughness, while a decreasing value indicates a smoothing of the emission surface. The latter portion of section 2.1 (page 20) discusses the definition and calculation of the field enhancement factor.

Table 7. Field enhancement factors (β) for the samples tested over several test runs.

Growth Time (hours)	Growth Pressure (Torr)	Post Growth Processing: Anneal Time/Temperature (minutes / ^{o}C)	Calculated Field Enhancement Factor for Consecutive Runs (unitless)	Trend Shown Over Successive Runs
0.5	10^{-5}	N/A	5091.4, 1428.5, 1651.8, and 2107.2	Decreased
0.5	10^{-5}	10 / 620	No Data	No data
0.5	10^{-3}	N/A	No data	No data
0.5	10^{-3}	10 / 620	864.9, 903.1, 2483.4, and 2545.8	Increased
3	10^{-5}	N/A	1789.5, 921, and 1374.4	Decreased
3	10^{-5}	10 / 620	2663, 1645, 2638, and 369	Decreased
3	10^{-3}	N/A	3027, 867, 1296, and 496	Decreased
3	10^{-3}	10 / 620	8987, and 977	Decreased
5	10^{-5}	N/A	No data	No data

Table 8 lists the maximum current density, turn-on electric field, and calculated field enhancement factor for each sample. The sample grown at 1700^{o}C under 10^{-5} Torr vacuum pressure for 0.5-hours with no post-growth annealing showed the lowest turn-on electric field (lower than 3.0 V/μm), while still exhibiting a high maximum current density (4.25 mA/cm^{2}, at 6.7 V/μm). This sample was drastically altered by the applied electric field and electric breakdown, as only one good voltage sweep run was observed. The sample grown at 1700^{o}C under 10^{-3} Torr vacuum pressure for 3-hours with no post-growth annealing exhibited the highest maximum current density (4.71 mA/cm^{2}, at 6.9 V/μm), while still having a reasonably low turn-on electric field of 6.0 V/μm.

Table 8. E_{to}, maximum currents densities, and β for each sample.

Growth Time (hours)	Growth Pressure (Torr)	Post Growth Processing: Anneal Time/Temperature (minutes / ^{o}C)	Calculated Field Enhancement Factor for Consecutive runs (unitless)	Minimum Turn-On Electric Field (V/μm / μA/cm^2)	Maximum current density (μA/cm^2 / V/μm)
0.5	10^{-5}	N/A	5091.4, 1428.5, 1651.8, and 2107.2	3.0 / 54.8	4247 / 6.7
0.5	10^{-5}	10 / 620	No Data	7.5 / 46.5	100.7 / 8.20
0.5	10^{-3}	N/A	No data	No data	No data
0.5	10^{-3}	10 / 620	864.9, 903.1, 2483.4, and 2545.8	5.5 / 36.1	794 / 9.0
3	10^{-5}	N/A	1789.5, 921, and 1374.4	5.5 / 9.61	600 / 9.50
3	10^{-5}	10 / 620	2663, 1645, 2638, and 369	3.20 / 16.7	2117 / 5.9
3	10^{-3}	N/A	3027, 867, 1296, and 496	6.0 / 37.7	4709 / 6.9
3	10^{-3}	10 / 620	8987, and 977	13.0 / 25	1825 / 17.0
5	10^{-5}	N/A	No data	No data	No data

The collected values compare well with those found in the literature. Table 3 (page 36), which gives a table of field emission data found in published literature, shows that the turn-on electric fields range from 1.6 to 9.8 V/μm. The data collected for this thesis showed turn-on electric fields in the range of less than 3.0 to 13.0 V/μm. Referring back to [20], Li *et al.* reported a turn-on electric field of 4 V/μm, an emission current density of 1 mA/cm^2 at an electric field of 9.5 V/μm, and a field enhancement factor of 4012. Comparatively, the data collected for this thesis is well in-line with previously published data.

The stability of the field emission current for each sample tested is compared in Table 9. From the data, one sees that each sample tested possesses at least one run with promising stability measurements. The values calculated for the average maximum

deviation from the average current measured (for each applied electric field) appear high, but considering this value accounts for voltage spikes in the recorded data, they are quite low. This value indicates that, on average, observed voltage spikes are less than 50% the average value for each voltage step for all but one sample.

The standard deviation is the square root of the average squared deviation from the mean of a data set, giving a measure of the spread of values in a data set. The standard deviation is calculated such that it is always a non-negative number and has the same units as the data set from which it was calculated. In a normal distribution, about 68% of the scores are within one standard deviation of the mean and about 95% of the scores are within two standards deviations of the mean. Standard deviations are useful in comparing sets of data which may have the same mean but a different range.

In order to bring together all the data for a given sample, the standard deviation was calculated for each applied electric field step. Because each applied electric field steps had different means, their standard deviations could not be combined with one another. To account for this, the standard deviation for each voltage step was computed as a percentage of the average for that step, yielding a 'percentage value'. The 'percentage values' for each applied electric field step were then averaged together, yielding an average value for the percent the standard deviations represent of the mean for each applied electric field step. Therefore, given a value of 12.2% in column 5 of Table 9, one can state that on average, the standard deviation for each step is 12.2% of the step's average current. The data given in Table 9, column 5, thus shows that the recorded currents were reasonably stable.

Table 9. Comparison of the stability measures for each sample.

Growth Time (hours)	Growth Pressure (Torr)	Post Growth Processing: Anneal Time/Temperature (minutes / ^{o}C)	Avg. Max Deviation from the Avg. Current Measured (%)	Avg. (over all e-field steps) the Std. Dev. for a Given Voltage Step is from the Avg. (%)	Additional Comments
0.5	10^{-5}	N/A	20.56	12.2	Run 1 only
0.5	10^{-5}	10 / 620	Not enough data	Not enough data	N/A
0.5	10^{-3}	N/A	No data	No data	N/A
0.5	10^{-3}	10 / 620	51.8 (35.8)	25.1 (17.2)	All Runs (run 3 only)
3	10^{-5}	N/A	63.5	21	All Runs
3	10^{-5}	10 / 620	49.9 (23.5)	26.6 (12)	All runs (run 3 only)
3	10^{-3}	N/A	48.4 (23, 27.2)	20.8 (12.6,13.1)	All runs (runs 3 and 4, respectively)
3	10^{-3}	10 / 620	50.3 (12.8)	26.4 (6.3)	All runs (run 4 only)
5	10^{-5}	N/A	No data	No data	N/A

4.3.3 Atomic Force Microscopy Analysis

In order to correlate the surface roughness of each sample to its field emission characteristics, atomic force microscopy (AFM) analysis was performed on each sample. For all samples, a Digital Instruments Dimension 3000 NanoScope III was used in tapping mode with scan lengths of 500 nm and 2 μm. Decreased electric field screening effects are expected from the samples with rougher surfaces, and likewise should exhibit superior field emission characteristics when compared to the samples with smoother surfaces.

Using the atomic force microscope, the surface roughness of a sample can be analyzed using the root mean square roughness (RMS) calculation. The RMS roughness

is the standard deviation of the data points representing the profile of the surface scanned and is calculated using equation (4.1).

$$R_{rms} = \sqrt{\frac{\sum_{n}^{N} \left(z_n - \bar{z} \right)^2}{N}} \tag{4.1}$$

where z_n represents a data point from the scan, $\bar{z}$ represents the average height of the data points from the scan, and N represents the total number of data points in the scan.

Table 10 shows the RMS roughness calculation for the nine samples tested. The RMS roughness was calculated for both 2 μm^2 and 500 nm^2 scans. Although the 2 μm^2 and 500 nm^2 scans were over the same regions on the sample surfaces, the differences in their calculations is likely due to different scan rates used for the two scan sizes. A faster scan rate was used for the larger scan area to reduce the scan time necessary for each sample tested.

The RMS surface roughness values show that for all samples grown, annealing for 10-minutes at 620^{o}C under flowing O_2 increased the surface roughness. For the 0.5-hour growth samples that were not annealed after growth, growth under 10^{-3} Torr yielded rougher surfaces than the samples grown under 10^{-5} Torr based on the RMS roughness. This relationship, however, is reversed for the 3-hour growth samples that were not thermally annealed after growth. For samples grown under 10^{-5} Torr vacuum conditions that did not undergo post-growth thermal annealing, longer growth times yielded rougher surfaces (0.5-, 3-, and 5-hour growth times). This relationship was reversed for samples grown under 10^{-3} Torr vacuum conditions that received no post-growth thermal

annealing, as shorter growth times yielded rougher surfaces based on the RMS surface roughness calculations.

Table 10. Root mean square surface roughness for the samples tested.

Growth Time (hours)	Growth Pressure (Torr)	Post Growth Processing: Anneal Time/Temperature (minutes / ^{o}C)	2 μm^2 surface scan (nm)	500 nm^2 surface scan (nm)
0.5	10^{-5}	N/A	1.958	1.563
0.5	10^{-5}	10 / 620	No data	7.632
0.5	10^{-3}	N/A	5.269	2.197
0.5	10^{-3}	10 / 620	14.537	3.975
3	10^{-5}	N/A	5.279	3.130
3	10^{-5}	10 / 620	5.436	3.195
3	10^{-3}	N/A	3.049	1.331
3	10^{-3}	10 / 620	5.046	3.066
5	10^{-5}	N/A	8.459	3.936

Based on the roughness data given in Table 10, the following three samples have the most ideal field emission surfaces: both of the CNTs films grown at both 10^{-5} and 10^{-3} Torr vacuum pressure and annealed at 620^{o}C for 10-minutes under flowing O_2, and the CNT film grown at 10^{-5} Torr vacuum pressure for 5-hours with no post-growth annealing (all three samples were grown at 1700^{o}C). The field emission data collected on these three samples showed below average field emission performances when compared to the other samples tested. For the CNT film grown at 10^{-5} Torr vacuum pressure and annealed at 620^{o}C for 10-minutes under flowing O_2, characteristic F-N emission was not expected regardless of the surface roughness due to the failure of the sample's Ta ohmic contact. No data was collected from the 5-hour growth sample (at 1700^{o}C under

10^{-5} Torr vacuum pressure), as only repeated trips of the power supply were observed during testing.

One possible cause for the deviation between the collected field emission data and the RMS surface roughness values is that 'outcroppings' on the emission surface are spaced too closely together, resulting in enhanced electric field screening effects. Another possible cause is that although the post-growth anneal treatment opens the tubes of the 0.5-hour growth samples making their surfaces rougher, the annealing also damages the CNTs causing their conductivity properties to deteriorate.

In Figures 65 through 73, AFM images of the surface roughness plot and the 3-D profile for each of the nine samples are shown. Based on the visual analysis of these images, one would preclude that the following three samples would have the most promising field emission surface properties: the sample grown for 5-hours under 10^{-5} Torr vacuum pressure at 1700^{o}C and did not receive post-growth annealing; the sample grown for 3-hours under 10^{-5} Torr vacuum pressure at 1700^{o}C and did not receive post-growth annealing; and the sample grown for 3-hours under 10^{-3} Torr vacuum pressure at 1700^{o}C that was annealed for 10-minutes at 620^{o}C after growth. Likewise, visual analysis would preclude that the following three samples would have the poorest field emission surface properties: the sample grown for 0.5-hours under 10^{-3} Torr vacuum pressure at 1700^{o}C and did not receive post-growth annealing; the sample grown for 3-hours under 10^{-3} Torr vacuum pressure at 1700^{o}C and did not receive post-growth annealing; and the sample grown for 0.5-hours under 10^{-5} Torr vacuum pressure at 1700^{o}C that was annealed for 10-minutes at 620^{o}C after growth. These assumptions are based on the topographical make-up of the nine surfaces, given that surfaces with

‘outcroppings’ will have promising field emission characteristics and relatively flat samples will not.

As in the deviations between the collected field emission data and the RMS surface roughness values, there are large discrepancies between the collected FE data and visual findings. The first conclusion drawn here is that the areas examined by the AFM probe did not give an adequate representation of the entire surface’s profile. Samples may have surfaces that are not consistent across their entirety. The next conclusion is that any ‘outcroppings’ on sample surfaces are easily destroyed under the application of electric fields.

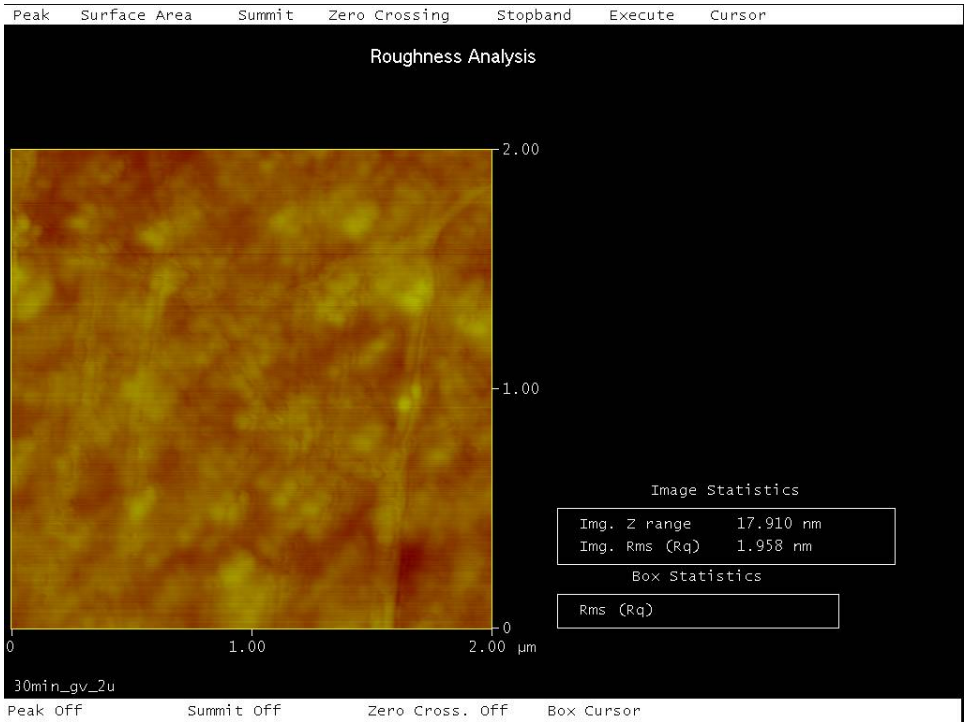

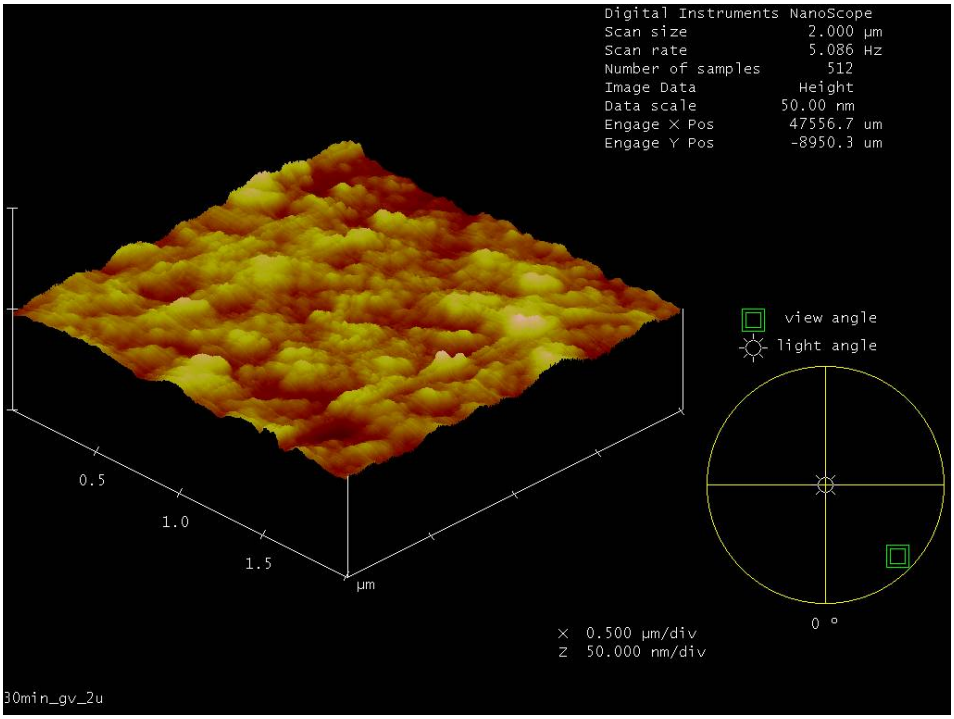

Figure 65. Atomic Force Microscopy surface roughness and 3-D profile for the CNT film grown at 1700°C under 10^{-5} Torr vacuum for 0.5-hours and with no post-growth annealing.

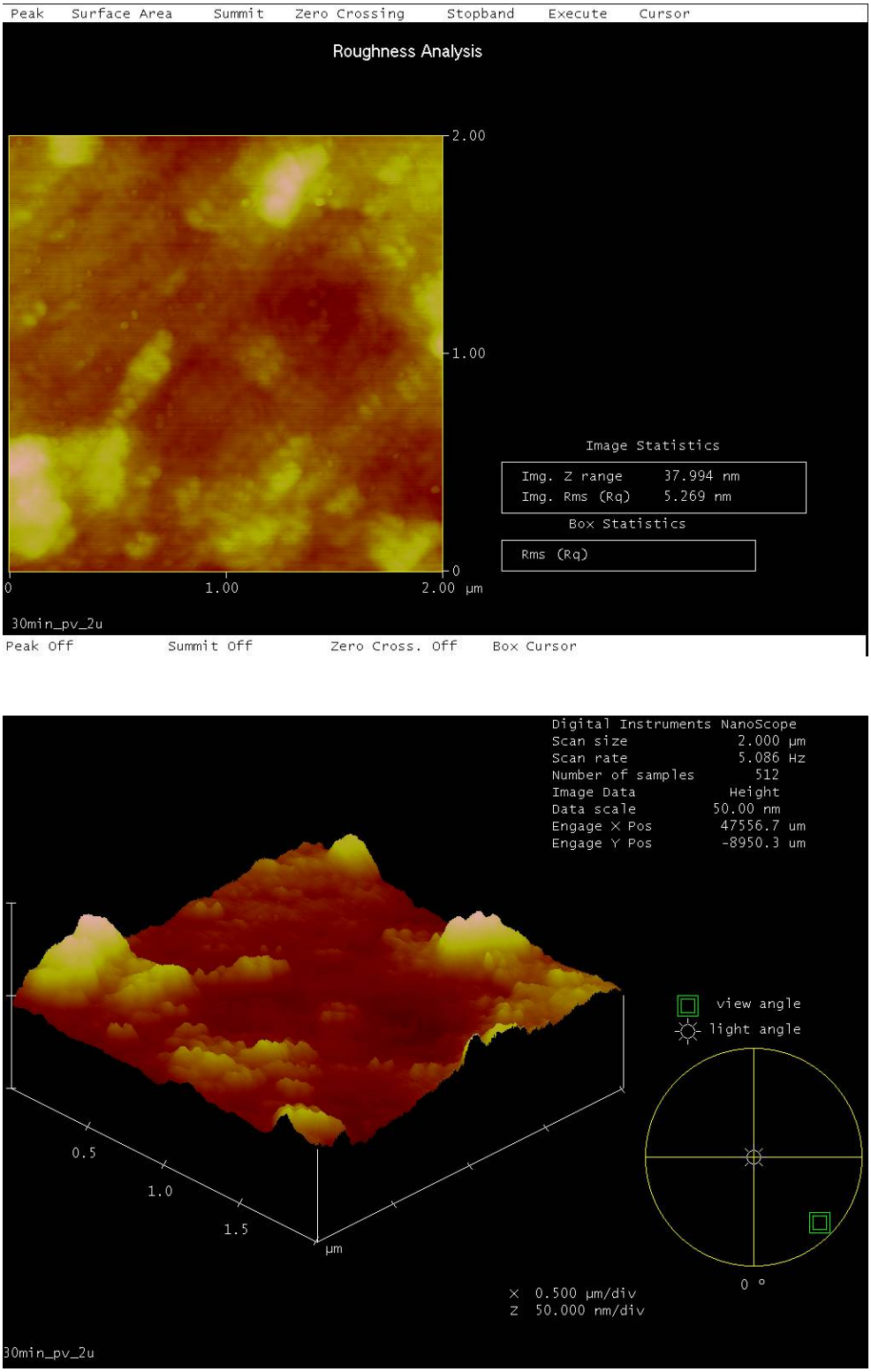

Figure 66. Atomic Force Microscopy surface roughness and 3-D profile for the CNT film grown at 1700°C under 10^{-3} Torr vacuum for 0.5-hours and with no post-growth annealing.

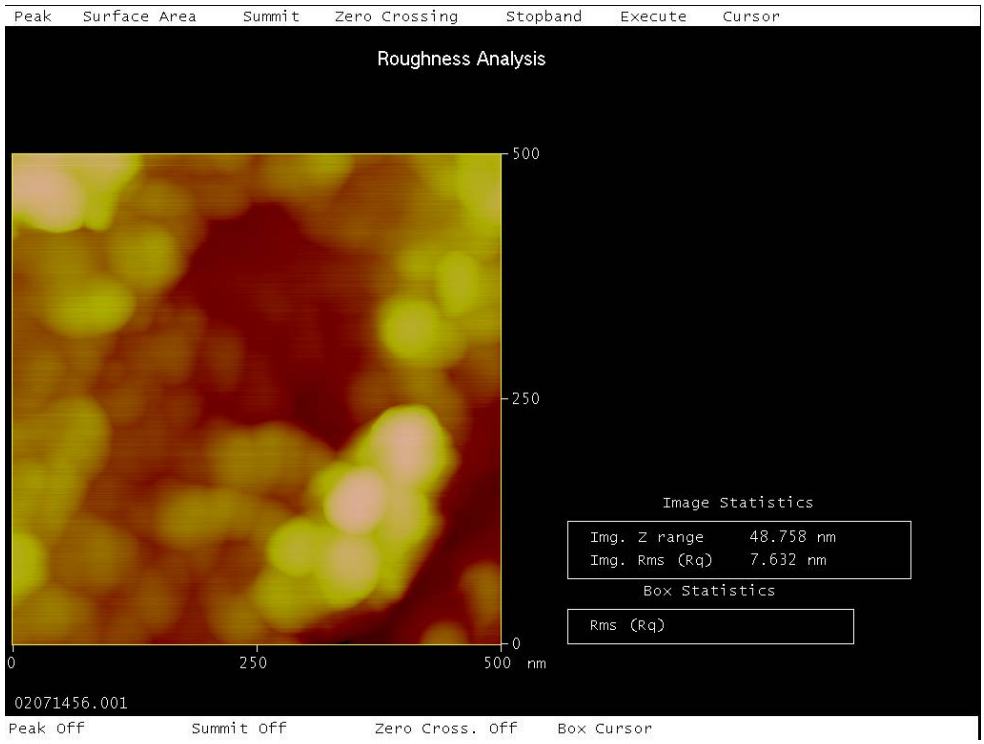

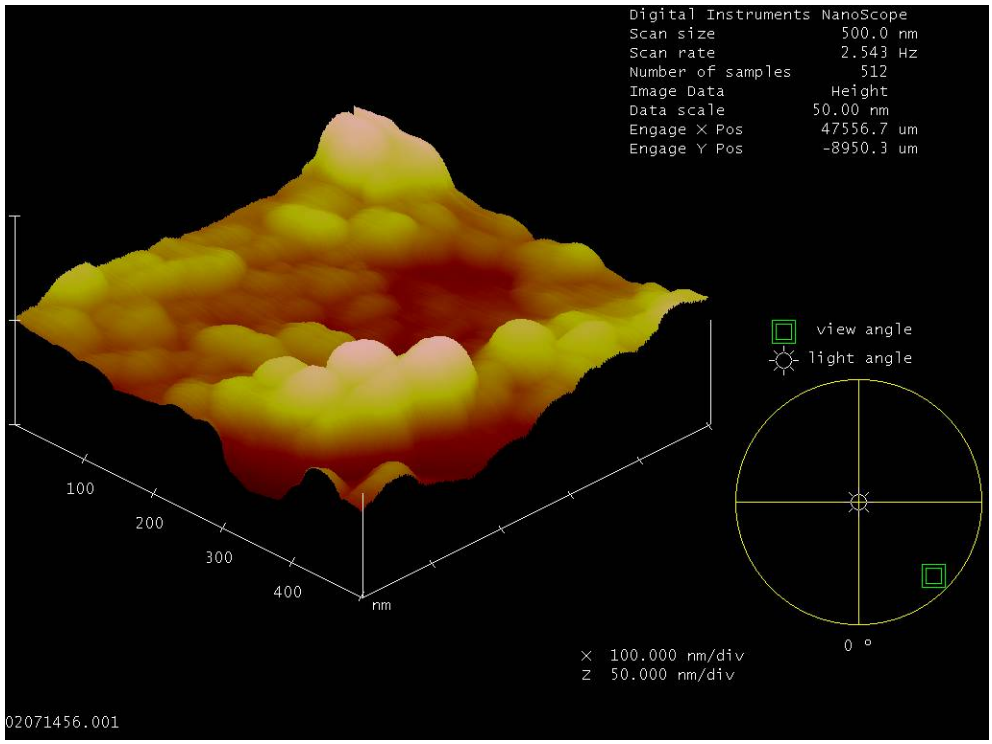

Figure 67. Atomic Force Microscopy surface roughness and 3-D profile for the CNT film grown at 1700°C under 10^{-5} Torr vacuum for 0.5-hours and annealed for 10-minutes at 620°C in flowing O_2.

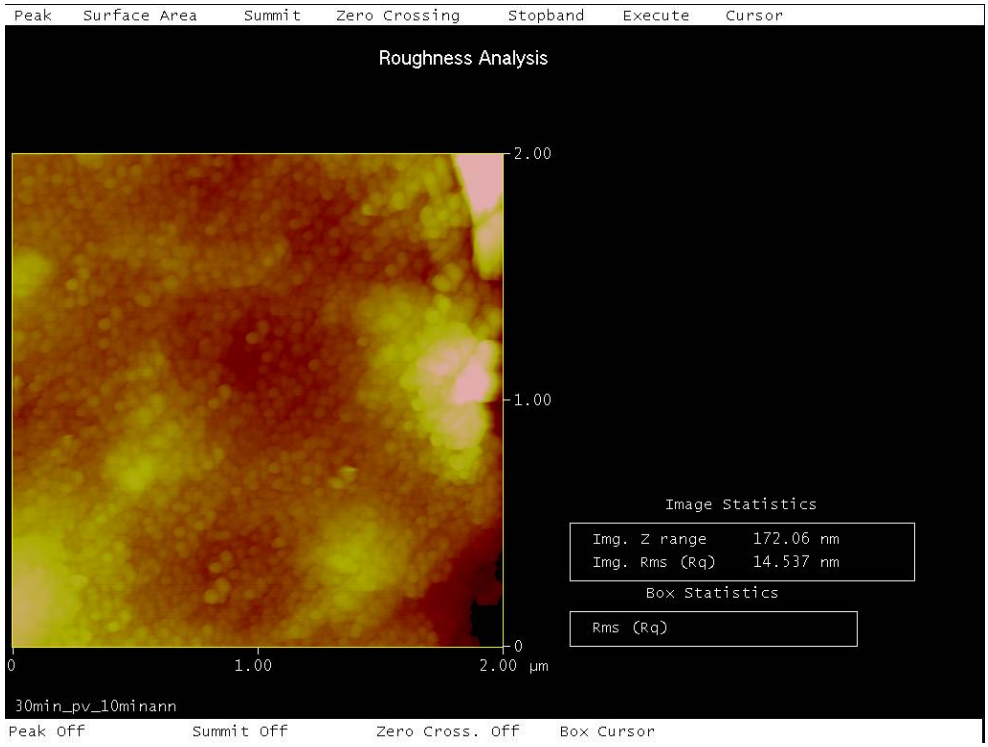

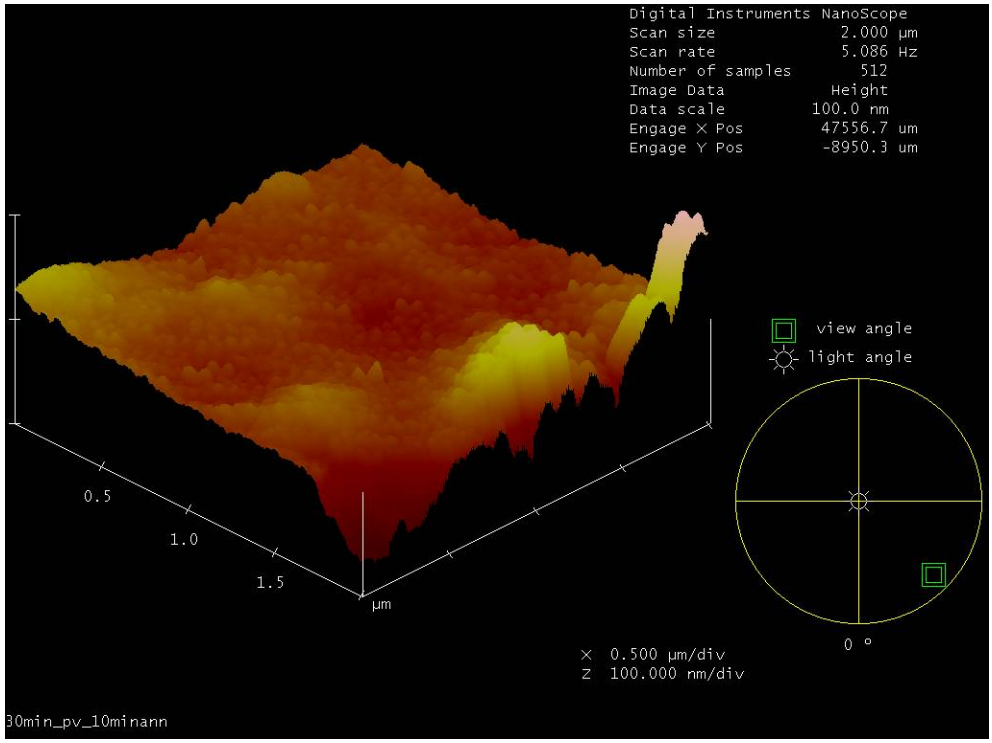

Figure 68. Atomic Force Microscopy surface roughness and 3-D profile for the CNT film grown at 1700°C under 10^{-3} Torr vacuum for 0.5-hours and annealed for 10-minutes at 620°C in flowing O_2.

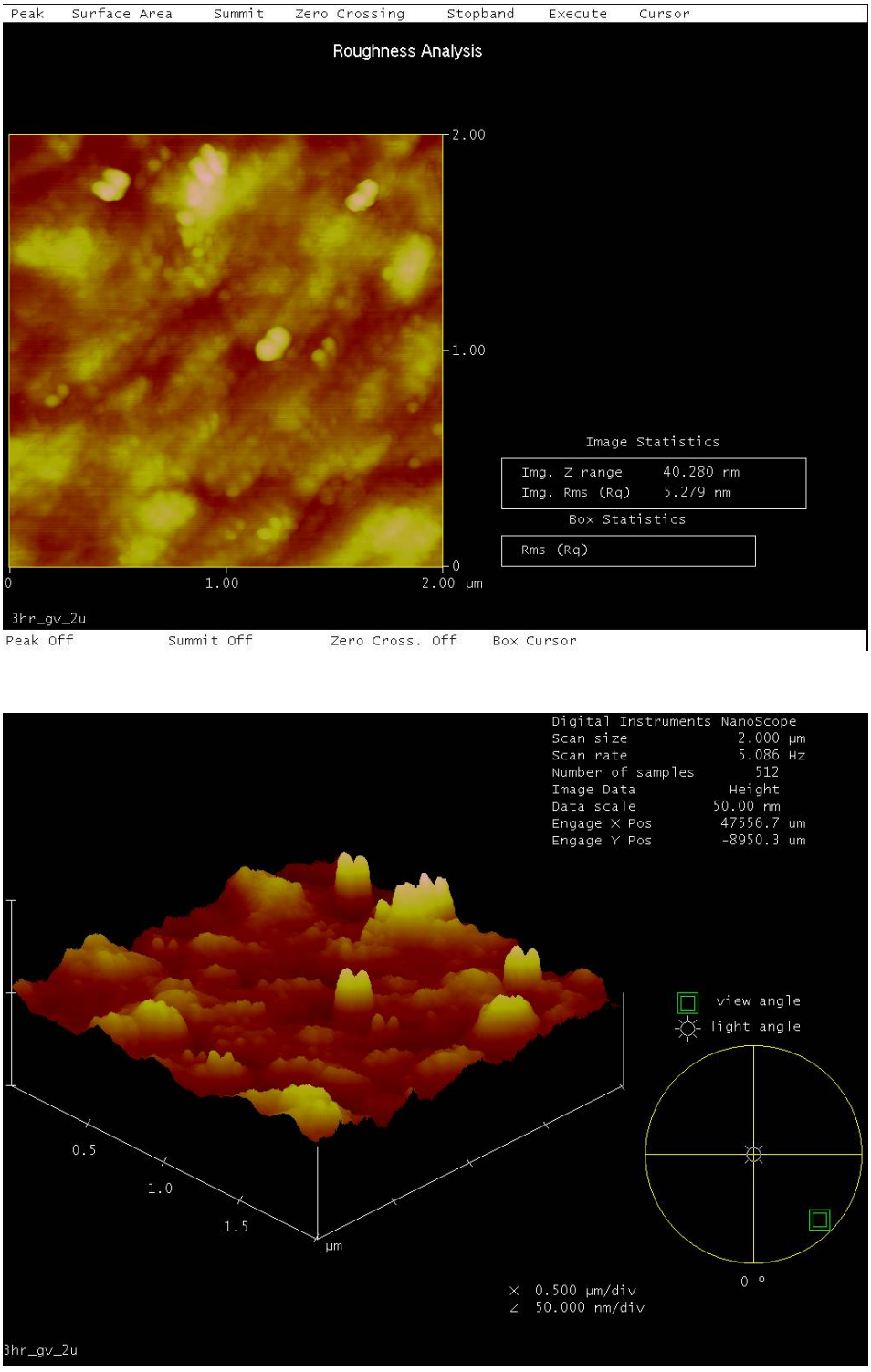

Figure 69. Atomic Force Microscopy surface roughness and 3-D profile for the CNT film grown at 1700°C under 10^{-5} Torr vacuum for 3-hours and with no post-growth annealing.

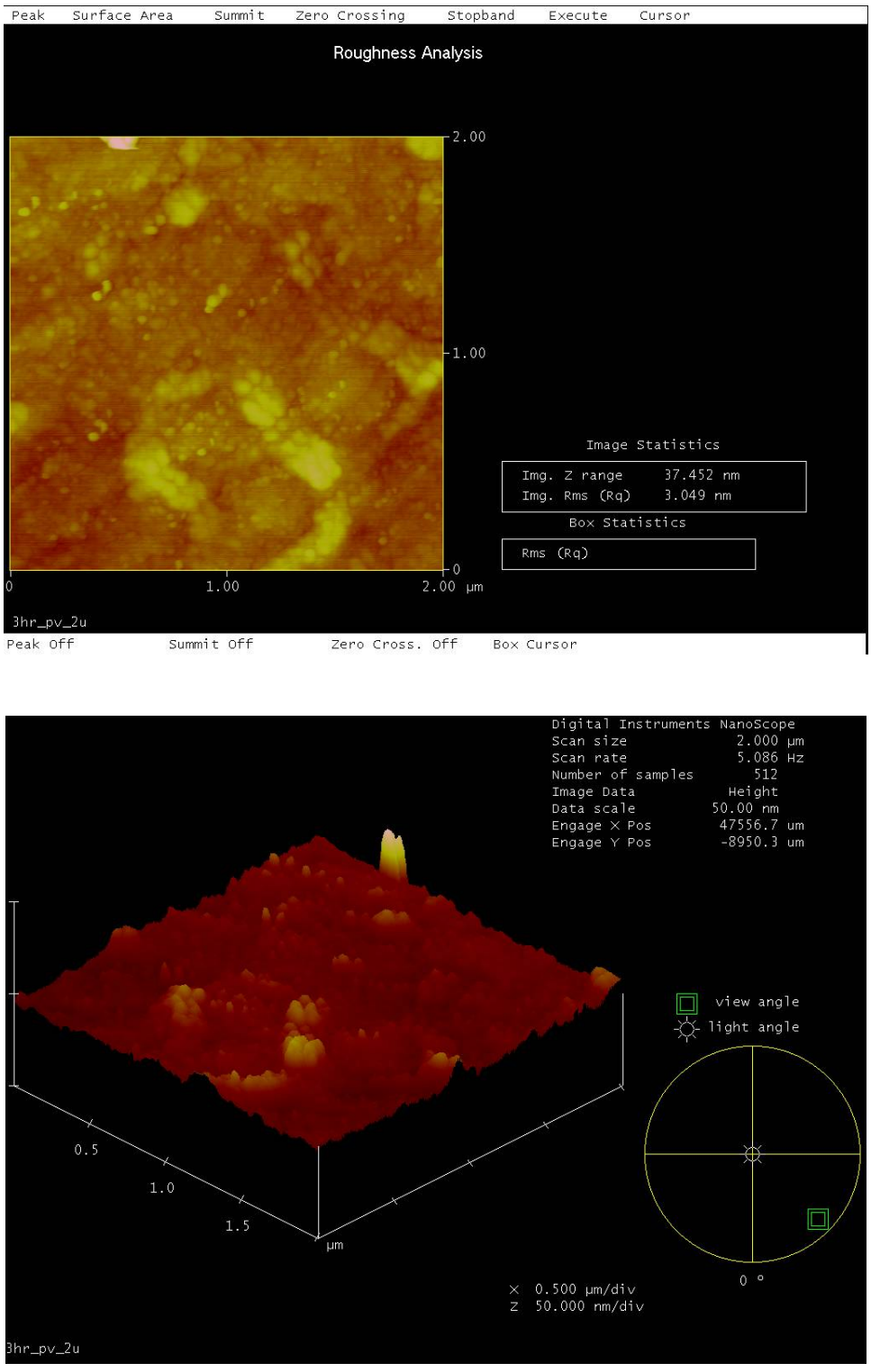

Figure 70. Atomic Force Microscopy surface roughness and 3-D profile for the CNT film grown at 1700°C under 10^{-3} Torr vacuum for 3-hours and with no post-growth annealing.

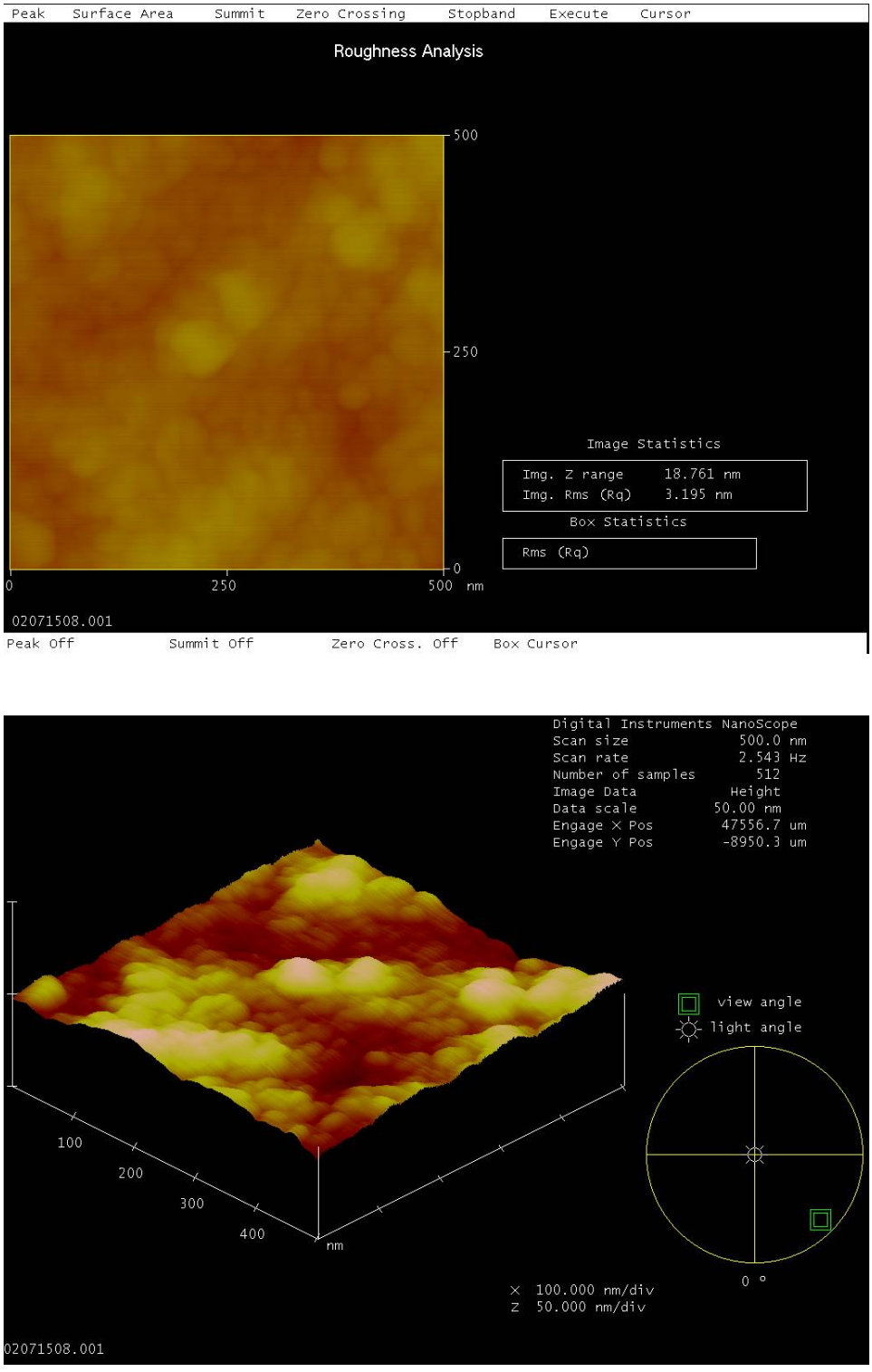

Figure 71. Atomic Force Microscopy surface roughness and 3-D profile for the CNT film grown at 1700°C under 10^{-5} Torr vacuum for 3-hours and annealed for 10-minutes at 620°C in flowing O_2.

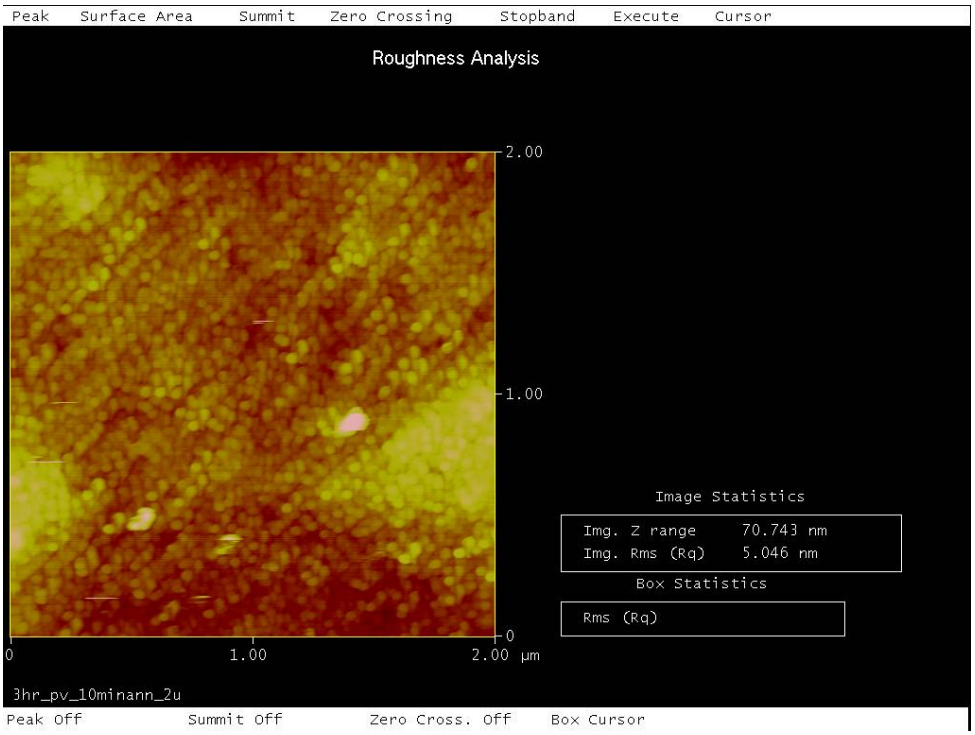

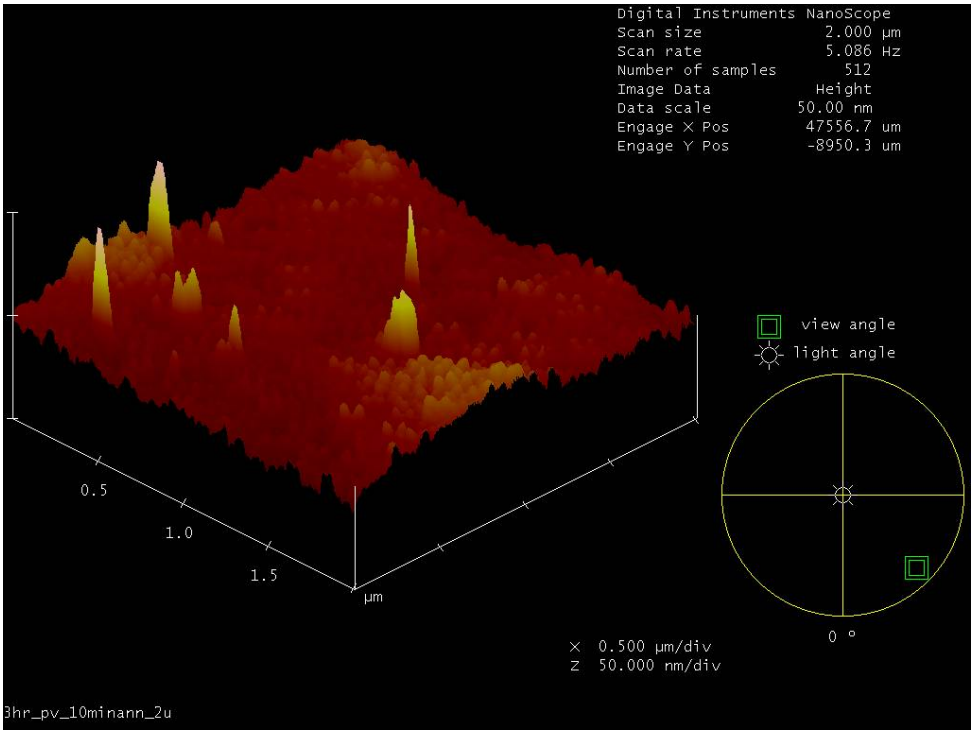

Figure 72. Atomic Force Microscopy surface roughness and 3-D profile for the CNT film grown at 1700°C under 10^{-3} Torr vacuum for 3-hours and annealed for 10-minutes at 620°C in flowing O_2.

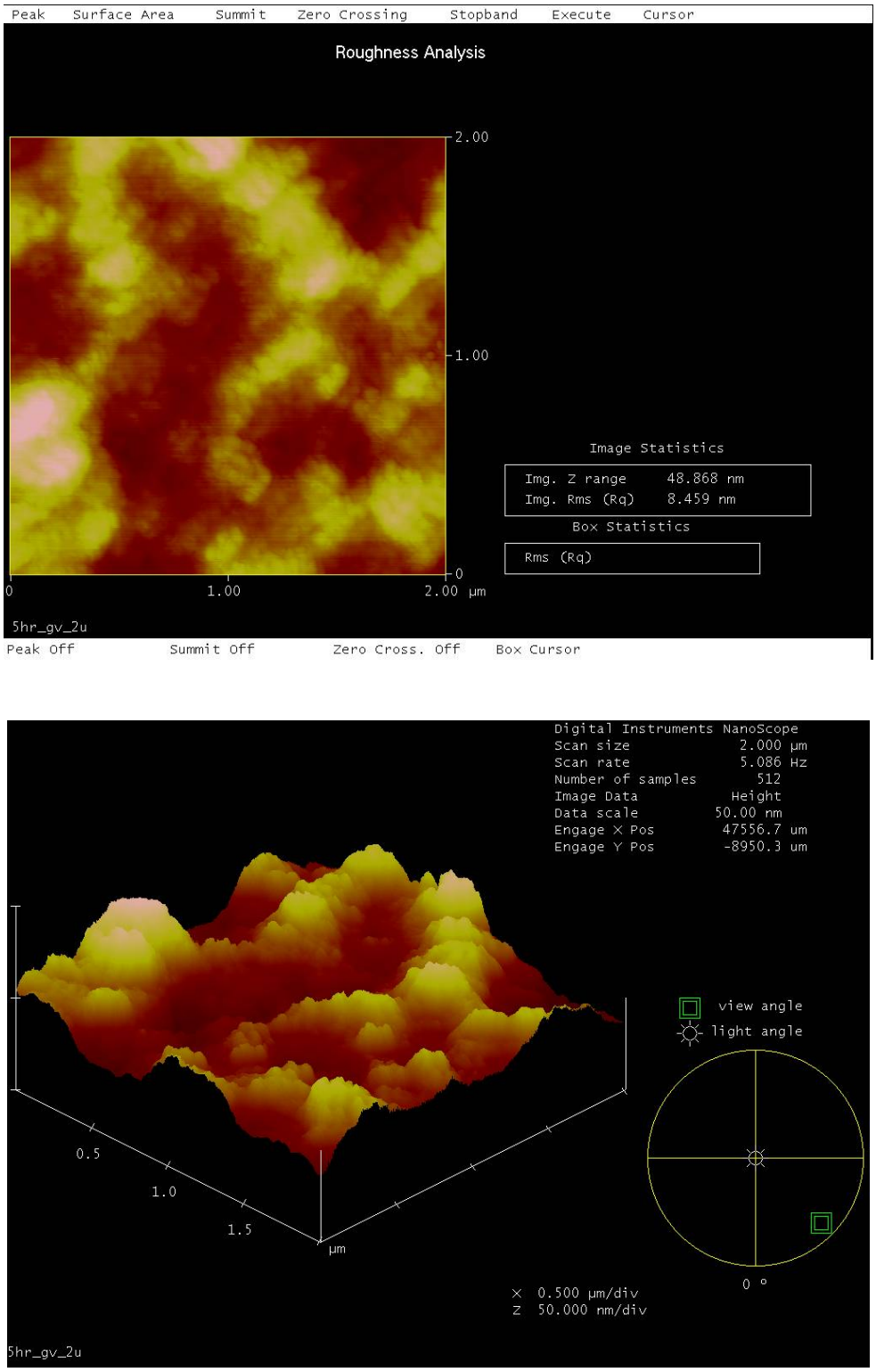

Figure 73. Atomic Force Microscopy surface roughness and 3-D profile for the CNT film grown at 1700°C under 10^{-5} Torr vacuum for 5-hours and with no post-growth annealing.

4.4 Chapter Summary

This chapter discussed the results collected during the experimental portion of the thesis. The results of the Transfer Length Method analysis of the Ta ohmic contact deposited on the backside of the SiC wafers were given, followed by the results of the post-growth annealing approach to open the CNTs. Lastly, the field emission properties of the CNT films tested were compared with one another, highlighting apparent trends and discussing inadequacies in the data collected and experimental methodology

Chapter 5: Conclusions and Recommendations

The research presented in this thesis is an investigation of the field emission properties of CNT films grown through the surface decomposition of silicon carbide substrates. This chapter contains a summary of the experimental findings, along with suggestions for future research.

5.1 Thesis Summary

The objective of this research was to fabricate CNT films using various growth parameters on silicon carbide substrates and then to measure the films' associated turn-on voltage, threshold voltage, and maximum current density exhibited. The data collected were compared with test data found in the literature associated with field emission tests performed on CNT films grown using catalyst metals and non-CNT film emitters (Tables 1 – 3). Additionally, the stability and ability of the CNT films grown by surface decomposition to withstand prolonged high field conditions was evaluated.

The most notable characteristic of the CNT films grown using AFRL/MLPS's method is that growth occurs without the use of catalyst metals, yielding CNTs that are potentially of greater purity than CNTs grown through the use of catalyst metals. The research performed for this thesis aimed to demonstrate whether use of CNT films grown in this unique manner would show improvement over catalyst-grown CNT films.

Although the samples fabricated and tested did not demonstrate improved field emission characteristics when compared to values found in the literature, the data collected show that further investigation is warranted regarding the CNTs' emission capabilities. From the collected data, the lowest turn-on electric field was found to be

lower than 3.0 V/μm, while exhibiting a high maximum current density of 4.25 mA/cm^2 at 6.7 V/μm.

The application of electric fields had notable effects on the samples tested. In some instances, the application of an electric field resulted in improved field emission characteristics in regards to lowered turn-on electric fields and increased maximum current densities; while in other cases, the field emission performances drastically deteriorated. This conflicting trend was concluded to be the result of different strength electric fields having different effects on the samples tested. This claim is substantiated by the highly different current versus applied electric field curves for successive runs for a given sample. Second, the CNT film is concluded to be not as stable as anticipated, as proven by the markings on the CNT film and copper anode after testing.

It is also concluded that the samples had different types and amounts of adsorbed molecules on their surfaces. The presence of adsorbents on the CNT films was verified by Mitchel and coworkers [13], whom reported that X-ray photoelectron spectroscopy (XPS) analysis showed that graphitic carbon and small amounts of oxygen were found in the film. Based on this knowledge, it is assumed that the adsorbed ionic impurities contributed to the instability of the films' field emission properties. The adsorbed impurities likely decreased the work function at various spots on the emission surface, causing points with lowered threshold fields on the surface. As the ionic impurities were desorbed, the emission current fell until the threshold field of the residual material – in this case the CNT film – was reached. This conclusion was drawn in part from other works found in the literature, and is supported by the saw-tooth nature of the current versus applied electric field curves given in Figures 46 and 63.

The presence of adsorbed molecules altered the field emission performance of the samples in different manners, and required the application of an electric field to condition the emission surface. The conditioning phase was not fully understood, as no consistency between samples was evident.

Electric breakdown (power supply current overload) occurred if strong electric fields were applied for prolonged periods of time between the cathode and anode. In addition, after electric breakdown occurred, marks were visible on the SiC surface within the field emission area of all samples tested. SEM analysis of the marks showed that the emission surface had been etched, appearing as though the CNTs were sublimated off of the SiC substrate in some spots. Markings noticeable to the naked eye were also apparent on the copper anode. This suggests that the CNT material evaporated off of the emission surface and impacted the anode, which likely resulted in the observed electric breakdown or perception of electric breakdown by the power supply.

Although AFM analysis showed that the annealed samples possessed rougher surfaces when compared to their corresponding non-annealed samples, the field emission results did not correspond to this finding. One conclusion is that the annealing damaged the tube walls and deteriorated their favorable conductive properties, as either the 620^{o}C anneal temperature was too hot, or the 10-minute anneal time was too long to open the CNTs in a controlled manner. AFM analysis failed to show that growth in 10^{-3} Torr vacuum conditions resulted in CNT films that were less dense than films grown in 10^{-5} Torr vacuum conditions. A comparison of the root-mean-square surface roughness values of the 0.5-hour growth runs from the two growth pressures with each other, and

likewise between the two 3-hour growth runs, showed no trend in surface roughness as a function of growth pressure.

5.2 Recommendations for Continued Work

Knowledge gained from this thesis has opened the door for future efforts to further investigate the field emission characteristics of CNT films fabricated through the surface decomposition of SiC substrates. Although the fabricated samples produced currents that were indicative of F-N field emission, more work needs to be done to characterize the effects of various growth parameters and post-growth annealing to open the CNTs.

While CNTs grown using the SiC surface decomposition method were investigated because they were perceived to require less post-growth processing, one major recommendation of this thesis is to more thoroughly understand post-growth steps to condition the field emission surface. TEM analysis of the opened CNT samples would yield information on the structural make-up of the CNTs after post-growth thermal annealing. The post-growth thermal annealing process is presumed to do more than simply remove the CNT tips. The effects of varied annealing times and temperatures is an area of study deserving of further investigation. More distinctive characterization of the surface effects caused by different annealing times on samples with different CNT growth times will allow for the optimization of the surface topology for field emission.

The use of indium-tin-oxide (ITO) coated glass is recommended to visually monitor the distribution of the emission points within the emission area. The fabrication

of numerous ITO anodes is suggested due to the strong likelihood of damage being caused to the anode due to electric breakdown at strong electric fields.

Different thicknesses of Teflon® spacers, along with the means to create smaller holes in the Teflon® are recommended. The use of thinner Teflon® spacers will require less voltage to be applied to achieve equivalent electric field strengths. Patterning of the CNT films is recommended in a manner such that small clusters of vertically aligned CNTs can be produced to minimize electric field screening effects between emission sites. Moreover, further work is necessary to characterize the density of CNT films grown at varied vacuum pressures.

The search for a sample with known field emission characteristics continued throughout this research. This search should be continued so that data collected from CNT test samples can be compared to known field emission samples' data. It is noted that no works cited in this thesis were found to have verified their test setup with baseline samples. This non-existence of baseline test samples makes it difficult to compare field emission data found in the literature.

Lastly, the use of different power supply and multi-meter equipment is advised. Specifically, a Keithley 237 High-Voltage Source-Measurement Unit, capable of supplying up to 1100 VDC and reading current with 10 fA sensitivity, is recommended for purchase. Although having a lower maximum voltage which requires the use of thinner Teflon® spacers (in the range of 25 μm), the increased current sensitivity of the voltage source will eliminate the need for a stand-alone multi-meter.

Appendix A: Carbon Nanotube Properties

Since their discovery by Iijima in 1991 [3], CNTs have been extensively studied for their electrical and mechanical properties. This appendix discusses the background of CNT electrical and mechanical properties, along with the growth methods of CNTs.

A.1 Background on CNT Properties

CNT types are distinctively described by the number of hollow concentric cylinders of carbon atoms they comprise of, ranging from one to many layers, and likewise are referred to as either single-walled or multi-walled CNTs. The single-walled CNT's structure can be described as a single sheet of graphite rolled into a tube [4], and is illustrated in Figure 74.

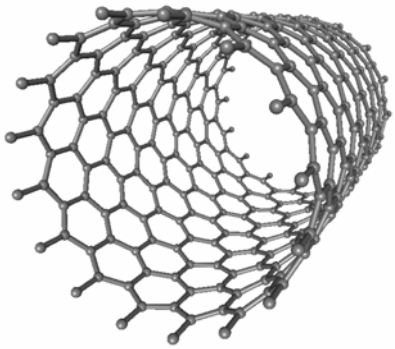

Figure 74. Illustration of the single-walled CNT structure [14].

The most prominent characteristic of CNTs is simply their size, as they typically have diameters ranging from 1 to 50 nm and lengths of several micrometers [4]. This large length to radius ratio makes CNTs nearly one dimensional, where operating characteristics are driven heavily by quantum mechanics. Additionally, because CNTs are held together by strong carbon-to-carbon bonds, they possess extremely high

mechanical stability and chemical inertness. One source notes that CNTs have a Young's modulus about ten times higher than that of steel [40].[1] The electrical properties of CNTs are even more promising, as theoretical predictions show that electrons can 'shoot' up and down the tube, conducting electricity with virtually no resistance. Additionally, CNTs can behave as metals or semiconductors. Table 11 summarizes several key properties of CNTs [5].

Table 11. Summary of CNT Properties, after [41].

Property	Feature
Mechanical	Young's modulus of 1 TPa (5x that of steel); tensile strength 45 GPa (20x that of steel); density of 1.4 g/cm^3 (Steel: ranges from 7.7 to 8.03 g/cm^3); and a strength/weight ratio 500x greater than Al, steel, and Ti.
Chemical	Stable in solvent, acids, and bases. All carbon-to-carbon chemical bonds of are filled, leaving them chemically inert.
Thermal	Higher thermal stability than graphite and amorphous carbons. Theory predicts their thermal conduction is 600 W/m-K (Copper is 400) to 3kW/m-K (Diamond is 2 kW/m-K).
Electrical	Suitable for microelectronics, as they can be semiconducting or metallic depending on their structure. CNTs are capable of carrying a current density of 10^9 A/cm^2 [41]. Carrier transport is one dimensional, implying reduced phase space for scattering of carriers.

A.2 CNT Physical Structure and Associated Electrical Properties

Studies exploring the structure of CNTs using high-resolution microscopy techniques show that they are cylindrical structures based on the hexagonal lattice of carbon atoms formed of crystalline graphite [4]. Depending on how the two-dimensional graphite sheet is 'rolled up,' three types of CNTs are possible: armchair, zigzag, and chiral. The different types are explained in terms of the unit cell of a CNT, which is

[1] Young's modulus is the elastic modulus for tension, and is the force per unit cross section of the material divided by the fractional increase in length.

described by a vector known as the *chiral vector (*C_h), and is illustrated in Figure 75 [14]. The *chiral vector* of the CNT, C_h, is defined by $C_h = n\hat{a}_1 + m\hat{a}_2$, where $\hat{a}_1$ and $\hat{a}_2$ are unit vectors in the basal plane of two-dimensional hexagonal lattice, and *n* and *m* are integers. The three types of CNTs are illustrated in Figure 76 [42]. When the graphite sheet is rolled up to form the CNT, the ends of the *chiral vector* meet. The *chiral vector* thus forms the circumference of the CNT's circular cross-section, and different values of *n* and *m* lead to different CNT structures. With the values *n* and *m* (often denoted as (*n, m*)), the diameter of the tube formed (D) can be determined using [41]:

$$D = (3^{1/2})a_{cc}(n^2 + m^2 + nm)^{1/2} \quad (\text{Å}) \qquad (A.1)$$

where $a_{c\text{-}c}$ is the distance between neighboring carbon atoms in a flat graphite sheet and is approximately 1.42 Å.

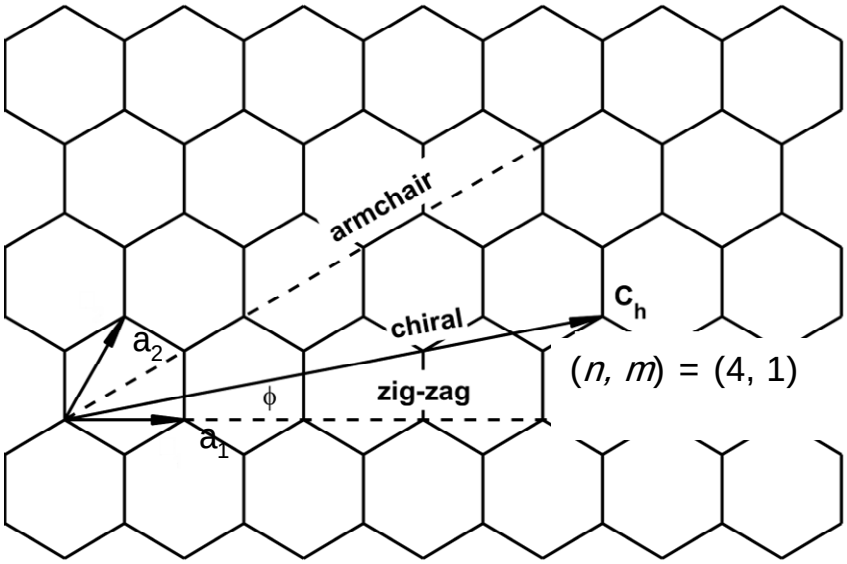

Figure 75. Depiction of the CNT chiral vector, after [14].

The electrical properties of a CNT depend on the values of *n* and *m.* A variation in the *chiral vector* can cause a CNT to change behavior electrically from that of a metal

to that of a large bandgap semiconductor [41]. Calculations show that the electrical characterization of a CNT is metallic provided that $n - m = 3i$, where i is zero or an integer; and semiconducting otherwise.

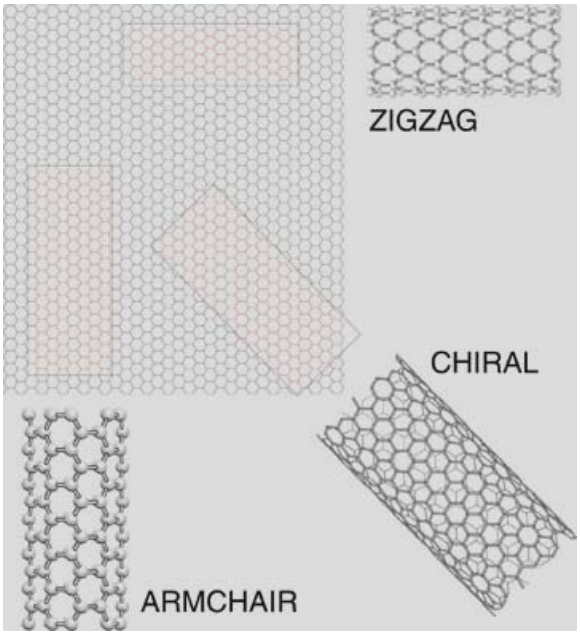

Figure 76. Depiction of chiral, zigzag, and armchair CNTs [42].

The band structure of single-walled CNTs is derived from the band structure of graphene. Graphene, simply a single atomic layer of graphite, consists of a two-dimensional honeycomb structure with each carbon atom bound to three other carbon atoms by covalent sp^2 bonds [43]. Graphene's band structure has states crossing the Fermi level at six points in k-space, as shown in Figure 77. It is called a zero-bandgap semiconductor because it exhibits metallic characteristics in some directions and semiconducting in others.

In a single-walled CNT, the momentum of the electrons moving around the circumference of the tube is quantized, reducing the available states to slices through the

two-dimensional band structure. The quantization is induced by the folding of the graphene layer to create a CNT, and causes a confinement of electrons around the circumference of the CNT.

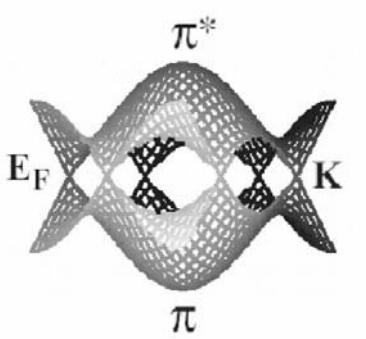

Figure 77. Illustration of the band structure of graphene [5].

With a CNT's *chiral* characteristics, the bandgap, E_g, can be calculated. E_g varies inversely with tube diameter, under the condition [41]:

$$E_g = \frac{2y_o a_{cc}}{D} \quad (eV) \qquad (A.2)$$

where y_o is the carbon to carbon bond energy in eV, D is the tube's diameter given by equation (A.1), and a_{cc} is the nearest neighbor atomic distance (bond length). The carbon-carbon bond energy is approximately 2.5 eV [41]. Typical CNT bandgaps vary from 10 meV to 1 eV [41].

Typically, theoretical focus is placed on single-walled CNTs, as opposed to multi-walled CNT's due to the multi-walled CNT's complex structure, where each outer shell can possess different electronic character. Also, multi-walled CNTs have complex shell-to-shell interactions that are difficult to model. Multi-walled CNTs show 1-D or 2-D characteristics, depending on their diameter and the property under investigation [5].

A.3 Carbon Nanotube Growth Methods

There are several methods to grow CNTs, each resulting in different purity, size, shape, and number of 'walls.' During the past decade, many studies have characterized various preparation methods. The three primary methods used in preparing CNTs include (a) electric arc discharge, (b) laser ablation, (c) chemical vapor deposition (CVD). In most all of the derivatives of these three techniques, a metal catalyst (typically Co, Fe, and/or Ni) in the form of nano-particles (particle radii ~10 nm) is used [40].

In laser ablation, a quartz tube containing argon gas and a graphite target are heated to 1200^{o}C [40]. Contained in the tube, but somewhat outside the furnace, is a water-cooled copper collector. The graphite target contains small amounts of cobalt and nickel that act as catalysts for the formation of the tubes. A pulsed laser incident on the target evaporates carbon from the graphite, and the argon gas sweeps the evaporated carbon atoms from the higher temperature zone to the cooler copper collector where the carbon atoms condense to form CNTs [40]. CNTs 10 - 20 nm in diameter and 100 μm long can be made by this method [40].

In the electric arc discharge method, a potential of 20 - 25 V is applied across cylindrical carbon electrodes of 5 - 20 μm diameter and separated by 1 mm at a 500 Torr pressure of flowing helium gas [40]. Carbon atoms are ejected from the positive electrode and form CNTs on the negative electrode. As the CNTs form, the length of the positive electrode decreases, and a carbon deposit forms on the negative electrode. To produce single-walled CNTs, a small amount of cobalt, nickel, or iron is used as a catalyst. If no catalysts are used, the fabricated CNTs are multi-walled [40]. The electric arc method produces single-walled CNTs 1 – 5 nm in diameter and lengths up to 1 μm.

Chemical vapor deposition (CVD), currently the most widely used method, involves decomposing a hydrocarbon gas (such as methane (CH_4)) at 550-900^{o}C. As the hydrocarbon gas decomposes, carbon atoms are produced/freed that condense on a cooler substrate containing metal catalysts.

One typical problem encountered during synthesis methods involving catalyst metals is that there is an unwanted presence of the metal catalyst particles in the CNT product. The removal of these unwanted particles from the CNT is difficult and usually damages the CNTs [5].

Similar to semiconductor device processing, where the growth materials and device fabrication is two distinct steps, CNT device fabrication consists of two steps as well. Because CNT growth procedures (even those termed 'selective growth') often result in large bundles of CNTs where there is little control over the type of CNTs grown (semiconducting or metallic) and their orientation, post growth methods for fabricating CNT-based devices have been developed. Figure 78 shows the random orientation and entanglement of CNTs grown using thermal CVD.

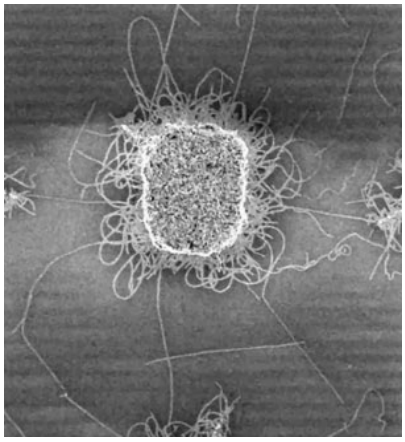

Figure 78. SEM image of CNTs grown from a catalytic island using thermal CVD, scale unknown [44].

The mechanisms for CNT growth are not fully understood. A critical area of improvement lays in the development of self-assembly growth procedures. The ability to fabricate uniform CNT arrays, with precise control of their chirality characteristics, and to position them precisely and controllably onto other nanostructures, is essential for CNT devices to be marketed commercially.

Appendix B: Experimental Setup Details and Operating Procedures

B.1 Sample Holding Apparatus:

The dimensions of the sample holding apparatus are as follows (all dimensions are given in length x width x height):

Acrylic plastic base:	7.6 cm x 5 cm x 0.5 cm
Copper base:	2.5 cm x 2.5 cm x 0.6 cm
Copper anode:	1.4 cm x 1.4 cm x 0.6 cm
Holding arms:	2.5 cm x 0.6 cm x 0.4 cm

Actual fabrication of the sample holder was carried out with the support of the AFIT model shop.

B.2 SiC Decomposition Procedure:

The following steps are performed using AFRL/MLPS's Oxy-Gon graphite resistance heating furnace to decompose the SiC samples to form CNTs (courtesy of Dr. John Boeckl, AFRL/MLPS).

System Start-up (process selection switch in STANDBY):

1. Turn ON the 80 psi house air (the vent and vacuum valves are air pressure activated).
2. Turn ON the Main Power switch (the handle is on the lower front of the main panel).
3. Turn the Roughing Pump ON (green button). The Roughing Pump will pull on the turbo-molecular pump -- to ~10^{-3} Torr on TC1 (this will take ~15 minutes).
4. Turn ON the ion gauge controller to read TC1 (it is the left switch on the gauge panel).
5. Turn the turbo-molecular pump ON (green button); it will pull on itself.
6. If the chamber is under vacuum, turn the process selection switch to VENT GAS, otherwise go to step 8.
7. Turn ON the low-O_2, N_2, or Ar at the tank and regulator; open the ball valve on the furnace to 25 (this step vents the chamber, allowing it to open).
8. When the chamber vents, turn OFF the low-O_2, N_2, or Ar ball valve, tank, and regulator.
9. OPEN the chamber, load the samples on the graphite cylinder, and SECURE the chamber door.

Soft Bake:

10. Turn the process selection switch to STANDBY; then to ROUGH.

11. Run the roughing pump until chamber is in the mid 10^{-2} Torr range (read TC2); this will take several minutes, and the pressure will slightly increase at TC1 (~15 minutes).
12. Turn process selection switch to HI VACUUM (turbo-molecular pump will pull on the chamber, roughing pump pulls on the turbo-molecular pump; TC2 will drop quickly; TC1 increases, then drops more slowly.
13. Turn ON the ion gauge filament when TC2 is in the 10^{-3} Torr range. Continue pumping until it is in the ~1 x 10^{-4} Torr range (note: ion gauge will not light if the pressure is too high).
14. OPEN the H_2O inlet and outlet hand valves (note: do this only if the chamber is under vacuum or filled with an inert gas).
15. Ensure the yellow H_2O handles are open and that the flow meters are turning.
16. RESET the over temperature controller for soft bake (red button on top right voltage meter).
17. Ensure the Vacuum Interlock Bypass is OFF. Turn the heat zone ON.
18. Ramp up AUTO/MAN power controller to 20% for soft bake (press AUTO/MAN key and one of the arrow keys simultaneously to change value).
19. Soft Bake chamber until the pressure reaches approximately 1.5 x 10^{-4} Torr range (bake for approximately 15 minutes once above 200^{o}C).

<u>Decomposition Process:</u>

20. Ramp up AUTO/MAN power controller to obtain target temperature (for graphite elements, limit A to 55% for T < 1150^{o}C; then adjust A to 69%, reduce A when ~ 25^{o}C below target value).

21. Decompose the sample (i.e. run heat) for desired time (adjust AUTO/MAN controller as needed).
22. At the desired time, ramp down AUTO/MAN controller to 0%.
23. After 5 minutes into ramp down, turn OFF the Heat Zone (this allows the power supply to cool).
24. When the temperature is $\leq 150^{o}C$, CLOSE the H_2O inlet and outlet hand valves.
25. Turn OFF the ion gauge filament (same switch used to turn it on).
26. Turn ON the low-O_2, N_2, or Ar at tank and regulator; open the ball valve on the furnace to 25.
27. Turn the process selection switch to VENT GAS to backfill the chamber.
28. When the chamber temperature is ~ $30^{o}C$, CLOSE the low-O_2, N_2, or Ar at the tank and regulator; OPEN the chamber; UNLOAD the samples; SECURE the chamber door.
29. If additional runs will be completed in the same day, load the new sample and return to step 10.

<u>System Shutdown:</u>

30. Turn process selection switch to STANDBY; then to ROUGH.
31. Turn ON the ion gauge controller to read TCs.
32. Run the roughing pump until TC2 reads approximately 10^{-2} Torr, then turn the process selection switch to HI VACUUM until TC2 reads approximately 10^{-3} Torr.
33. Turn the process selection switch to STANDBY; turn OFF the turbo-molecular pump.
34. Turn OFF the vacuum interlock bypass.
35. Turn OFF the roughing pump.

36. Turn OFF the ion gauge controller.

37. Turn OFF the main power switch.

38. Turn OFF 80 psi house air.

* For growth at 10^{-3} Torr vacuum pressure, the turbo-molecular pump is never turned on. The Vacuum Interlock Bypass must be turned on in this setup; otherwise the Heat Zone cannot be turned on.

B.3 Detailed Description of the Vacuum System Setup

Table 12. List of the equipment used in the experimental setup.

Product	Purpose	Obtained from:
Stanford Research Systems, Inc. High Voltage Supply	Apply high voltages between the anode and cathode (up to 5000 VDC).	AFIT/ENG Property
Agilent 34401A Multi-Meter	Record the field emission current to 10 nA sensitivity	AFIT/ENG Property
Drytel 31 Pumping System	Rough pump the vacuum chamber	Borrowed from AFIT/ENP
Thermocouple Pressure Gauge/Controller	Measure the vacuum pressure from atmosphere to 10^{-3} Torr	Borrowed from AFIT/ENP
Leybold TURBOVAC 150 CSV turbomolecular pump and controller	Enable the vacuum chamber to reach high vacuum conditions	Borrowed from AFRL/MLP
Neslab RTE 110 chiller/circulation unit	Keep the turbomolecular pump cool	Borrowed from AFIT/ENG
Gate Valve	Close off the vacuum chamber from the pumping components when venting	Borrowed from AFRL/MLP
Vacuum chamber	Provide space to conduct the experiment	Borrowed from AFIT/ENP
Ion gauge and controller	Measure the vacuum pressure below 10^{-3} Torr	Purchased from Kurt J. Lesker Company
Miniature High Voltage (MHV) coaxial feedthrough, 2 terminal	Pass electrical lines into/out-of the vacuum chamber	Purchased from Kurt J. Lesker Company
In-vacuum coaxial cables	Make connections within the vacuum chamber with minimal out-gassing	Purchased from Kurt J. Lesker Company
36" braided vacuum hose	Connect the roughing pump to the turbo pump	Borrowed from AFIT/ENP
Various sized copper flanges	One-time use copper seals at each ConFlat flange (the stainless steel flange's knife edge cuts into the copper flange, creating an ultra-high vacuum seal)	Purchased from MDC Vacuum Components, Inc.

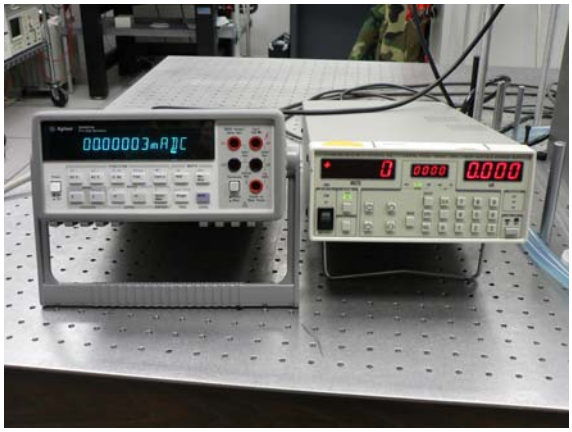

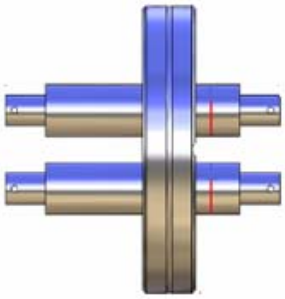

Stanford Research Systems, Inc. High Voltage Supply and Agilent Multi-Meter (left), and schematic of the dual MHV electrical feedthrough (right).

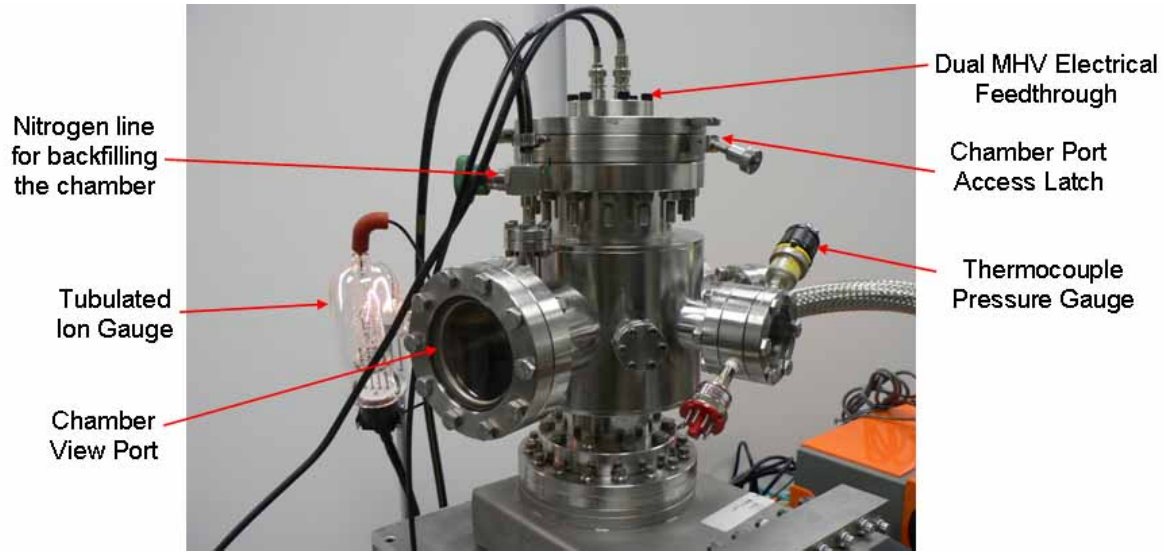

Depiction of the vacuum chamber showing the nitrogen line for backfilling the chamber, and the electrical feedthrough.

Appendix C: Supplementary Data and Images

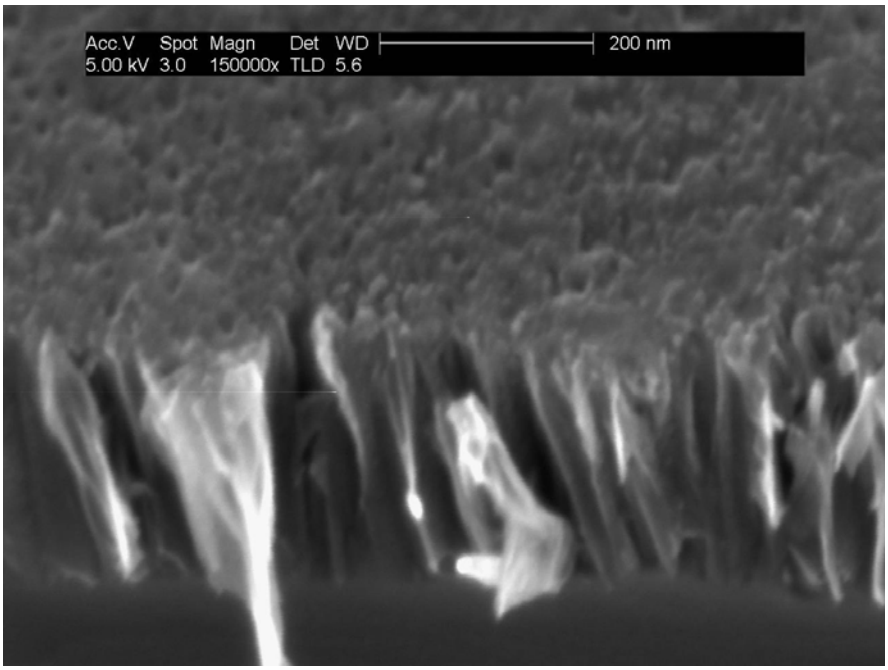

Resultant film from a 1-minute anneal at 620^{o}C under flowing O_2 on CNT film grown for 1-hour under 10^{-5} Torr vacuum at 1700^{o}C (face unknown, 30^{o} stage tilt, 150,000x magnification).

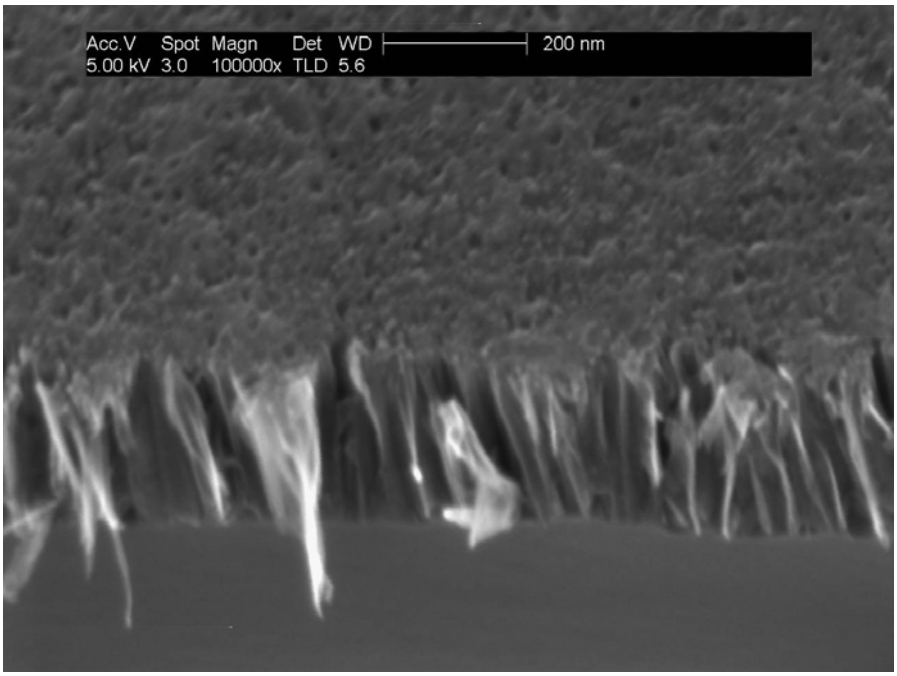

Resultant film from a 1-minute anneal at 620^{o}C under flowing O_2 on CNT film grown for 1-hour under 10^{-5} Torr vacuum at 1700^{o}C (face unknown, 30^{o} stage tilt, 100,000x magnification).

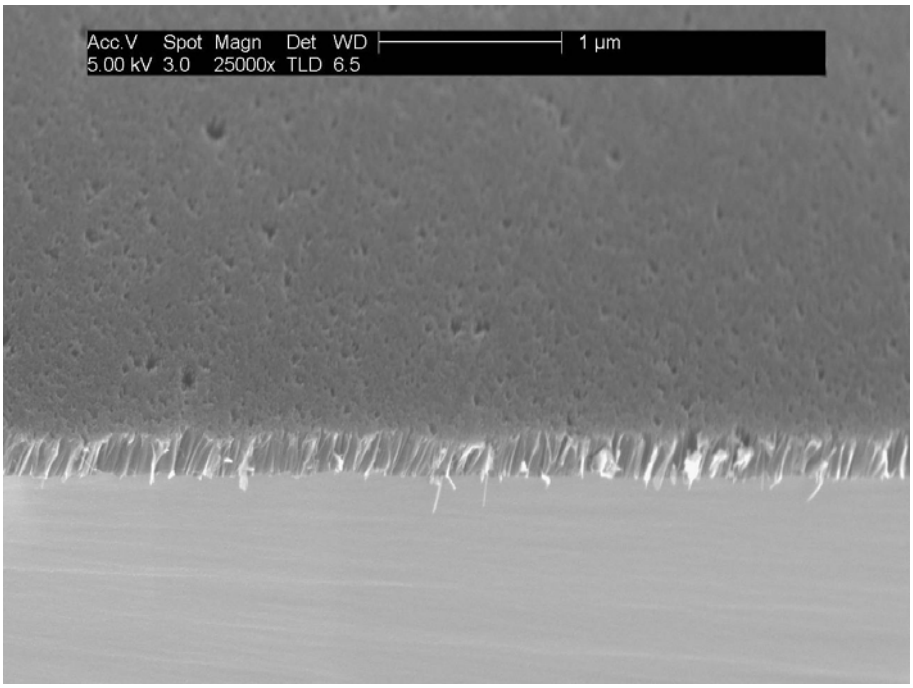

Resultant film from a 5-minute anneal at 620^{o}C under flowing O_2 on CNT film grown for 1-hour under 10^{-5} Torr vacuum at 1700^{o}C (face unknown, 30^{o} stage tilt, 25,000x magnification).

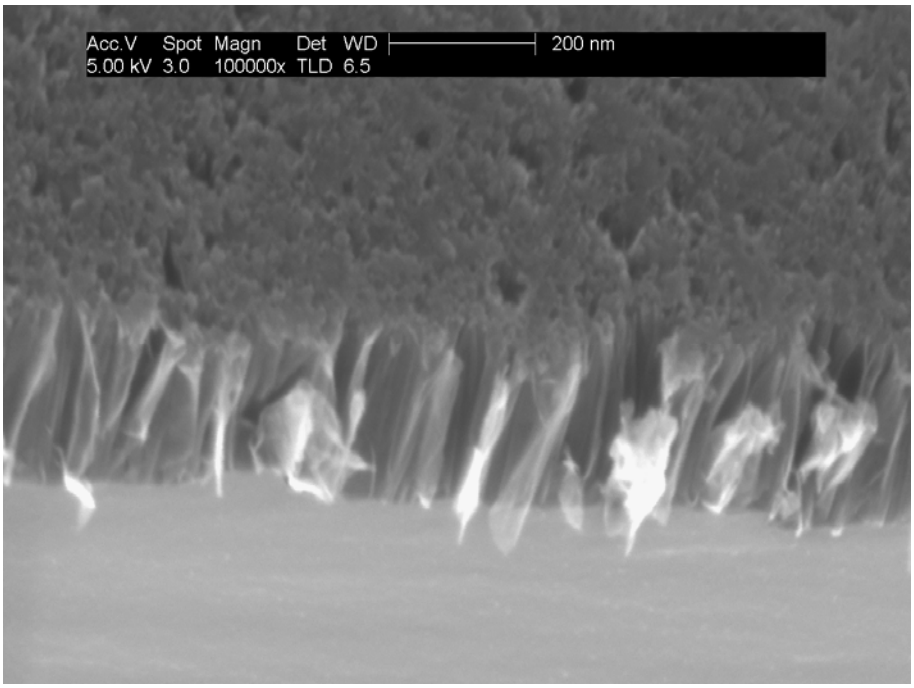

Resultant film from a 5-minute anneal at 620^{o}C under flowing O_2 on CNT film grown for 1-hour under 10^{-5} Torr vacuum at 1700^{o}C (face unknown, 30^{o} stage tilt, 100,000x magnification).

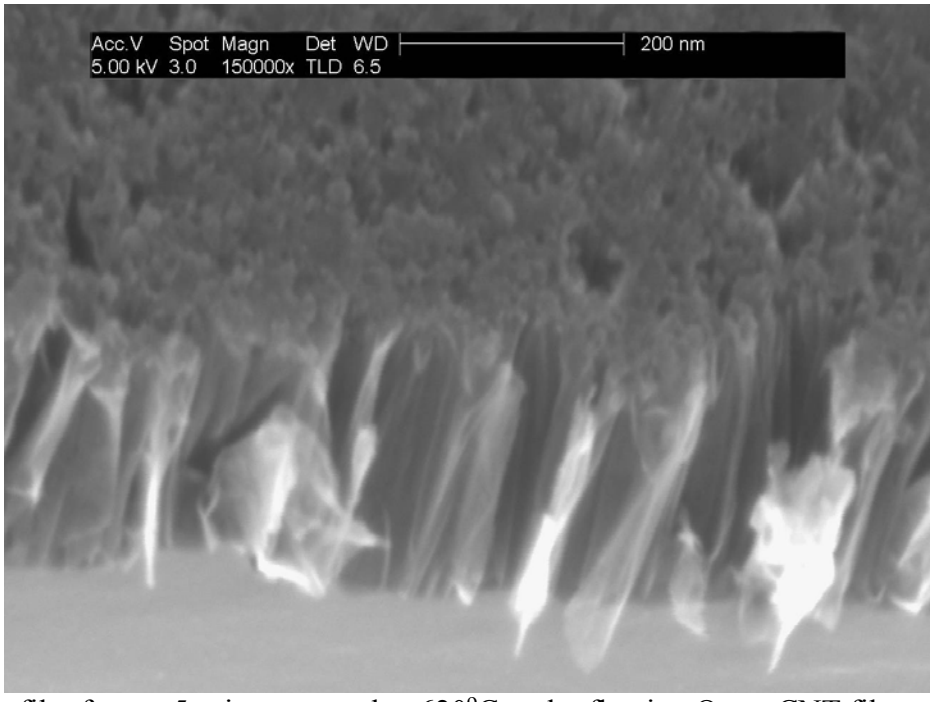

Resultant film from a 5-minute anneal at 620^{o}C under flowing O_2 on CNT film grown for 1-hour under 10^{-5} Torr vacuum at 1700^{o}C (face unknown, 30^{o} stage tilt, 150,000x magnification).

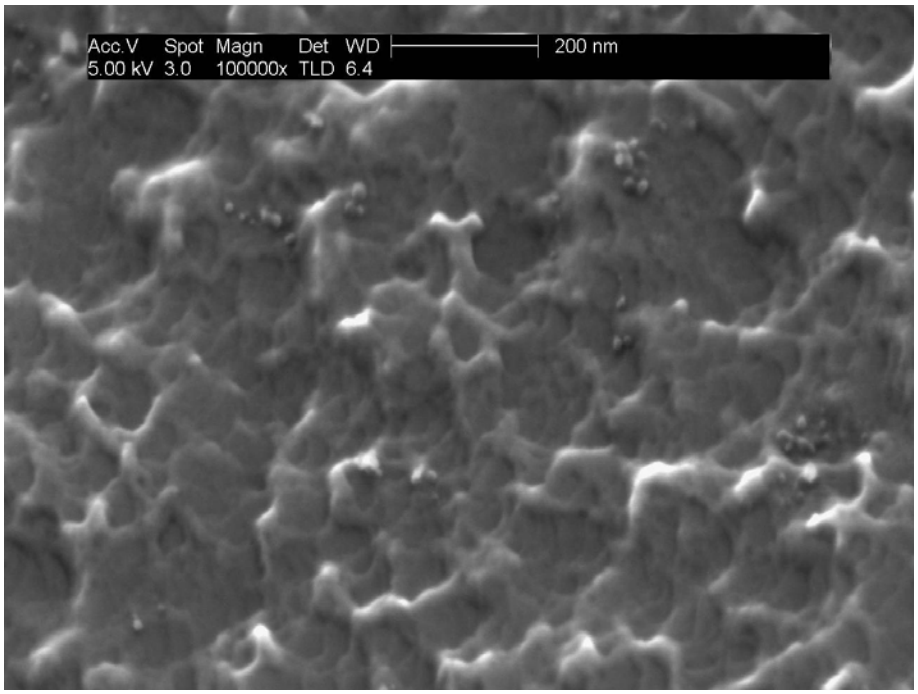

Resultant film from a 10-minute anneal at 620^{o}C under flowing O_2 on CNT film grown for 1-hour under 10^{-5} Torr vacuum at 1700^{o}C, showing no CNTs remaining on the SiC surface (face unknown, 30^{o} stage tilt, 100,000x magnification).

References:

[1] J. M. Bonard, F. Maier, T. Stockli, A. Chatelain, W. A. de Heer, J. P. Savetat, L. Forro, "Field emission properties of multiwalled carbon nanotubes," *Ultramicroscopy*, Volume 73, pages 7-15, 1998.

[2] G. Amaratunga, "Watching the Nanotube," *IEEE Spectrum*, 2003.

[3] S, Iijima, "Helical microtubules of graphitic carbon," *Nature*, volume 354, pages 56-58, 1991.

[4] Y. Saito, "Preparation and Properties of Carbon Nanotubes", 1999 *International Symposium on Micromechatronics and Human Science*.

[5] P. Avouris, J Appenzeller, R. Martel, and S. Wind, "Carbon Nanotube Electronics," *Proceedings of the IEEE*, vol. 91, no. 11, November 2003.

[6] V. Derycke, R. Martel, M. Radosaviljevic, F. M. Ross, P. Avouris, "Catalyst-Free Growth of Ordered Single-Walled Carbon Nanotube Networks," *Nano Letters*, Volume 2, Number 10, pages 1043-1046, 2002.

[7] C. A. Grimes, E. C. Dickey, C. Mungle, K. G. Ong, D, Qian, "Effect of purification of the electrical conductivity and complex permittivity of multiwall carbon nanotubes," *Journal of Applied Physics*, Volume 90, Number 8, 15 October 2001.

[8] H. Chen, Y. Chen, J. S. Williams, "New Approach for Purification of Multi-wall Carbon Nanotubes," *Proceedings of the 1st Nanomaterials Conference*, AEC Centre for Functional Nanomaterials, 2004.

[9] G. Fursey, *Field Emission in Vacuum Microelectronics*, Kluwer Academic/Plenum Publishers, New York, 2005.

[10] L. Solymar, D. Walsh, *Electrical Properties of Materials, Sixth Edition,* Oxford University Press, Oxford, 1998.

[11] R. H. Fowler, L. W. Nordheim, *Proceedings of the Royal Society of London A*, Volume 119, 1928, page 3.

[12] K. Teo, M. Lacerda, L. Robinson, S. Dalal, N. Rupesignhe, M. Chhowalla, S. Kee, D. Jefferson, D. Hasko, G. Amaratunga, W. Milne, P. Legagneux, L. Gangloff, E. Minoux, J. Schnell, D. Pribat, "Carbon nanotube technology for solid state and vacuum electronics," *IEEE Proceedings, Circuits Devices Systems*, Volume 151, number 5, October 2004.

[13] W. C. Mitchel, J. Boeckl, D. Tomlin, W. Lu, J. Rigueur, J. Reynolds, "Growth of Carbon Nanotubes by Sublimation of Silicon Carbide Substrates," Quantum Sensing and Nanophotonic Devices II, *Proceedings of the SPIE*, Volume 5732, January 2005.

[14] S. Iijima, "Carbon Nanotubes and their Recent Developments," *Proceedings of the IEEE*, 1998.

[15] Y. Saito, S. Uemura, "Field emission from carbon Nanotubes and its application to electron sources," *Carbon*, Volume 38, pages 169-182, 2000.

[16] Semet, V., Binh, V. T., Vincent, P., Guillot, D., Two, K. B. K., Chhowalla, M. Amaratunga, G., Milne, W., Legagneux, P., Pribat, D., "Field electron emission from individual carbon nanotubes of a vertically aligned array," *Applied Physics Letters*, Volume 81, Number 2, 8 July 2002.

[17] G. Fursey, D. Glazanov, "Deviations from the Fowler Nordheim theory and peculiarities of field electron emission from small-scale objects," *Journal of Vacuum Science Technology B*., Volume 16, Number 2, March/April 1998.

[18] Richard G. Forbes, C. J. Edgcombe, U. Valdre, "Some comments on models for field enhancement," *Ultramicroscopy*, Volume 95, 2003, pages 57-65, available from Science Direct.

[19] H. Manohara, W. Dang, P. Siegel, M. Hoenk, A. Husain, A. Schere, "Field Emission Testing of Carbon Nanotubes for THz Frequency Vacuum Micro-Tube Sources," *Proceedings of SPIE*, Volume 5342, 2004.

[20] Juntao Li, Wei Lei, X. Zhang, B. Wang, L. Ba, "Field emission of vertically-aligned carbon nanotubes arrays grown on porous silicon substrate," *Solid-State Electronics*, Volume 48, pages 2147 – 2151, 2004.

[21] J. M. Bonard, H. Kind, T. Stockli, L. O. Nilsson, "Field emission from carbon Nanotubes: the first five years," *Solid-State Electronics*, Volume 5, 2001, pages 893 – 914.

[22] Y. Q. Xu, H. Pend, R. H. Huage, R. E. Smalley, "Controlled Multistep Purification of Single-Walled Carbon Nanotubes," *Nano Letters*, Volume 5, Number 1, pages 163-168, 2005.

[23] M. Kusunoki, J. Shibata, M. Rokkaku, T. Hirayama, "Aligned Carbon Nanotube Film Self-Organized on a SiC Wafer," Japanese *Journal of Applied Physics, Part 2: Letters*, Volume 37, Number 5B, pages L605-L606, 15 May 1998.

[24] T. Nagano, Y. Ishikawa, N. Shibata, "Effects of Surface Oxides of SiC on Carbon Nanotube Formation by Surface Decomposition," *Japanese Journal of Applied Physics*, Volume 42, pages 1380 – 1385, 2003.

[25] T. Nagano, Y. Ishikawa, N. Shibata, "Preparation of Silicon-on-Insulator Substrate on Large Free-Standing Carbon Nanotube Film Formation by Surface Decomposition of SiC Film," *Japanese Journal of Applied Physics*, Volume 42, pages 1719 – 1721, 2003.

[26] M. Kusunoki, T. Suzuki, T. Hirayama, N. Shitata, "A formation mechanism of carbon nanotube films on SiC (0001)", *Applied Physics Letters*, Volume 77, Number 4, pages 531-533, 24 July 2000.

[27] Y. Song, F. W. Smith, "Phase diagram for the interaction of oxygen with SiC," *Applied Physics Letters*, Volume 81, Number 16, pages 3061 – 3063, 14 October 2002.

[28] M. Kusunoki, T. Suzuki, T. Hirayama, N. Shibata, "Aligned carbon nanotube films on SiC (0001) wafers, *Physica B*, Volume 323, pages 296 – 298, 2002.

[29] M. Ito, S. Sago, T. Suzuki, M. Kusunoki, T. Hirayama, S. Uemura, "Field Emission from Carbon Nanotube Films Formed by Surface Decomposition of SiC," *International Display Manufacturers Conference*, Korea, 2002.

[30] M. Inagaki, K. Kaneko, T. Nishizawa, "Nanocarbons – recent research in Japan," *Carbon*, Volume 42, pages 1401-1417, 23 February 2004.

[31] H. C. Miller, "Electrical Discharges in Vacuum, 1980 – 1990," *IEEE transactions on Electrical Insulation*, Volume 26, Number 5, October 1991.

[32] A. Evtukh, H. Hartnagel, V. Litovchenko, M. Semenenko, O. Yilmazoglu, "Enhancement of electron field emission stability by nitrogen-doped diamond-like carbon film coating," *Institute of Physics: Semiconductor Science and Technology*, Volume 19, Number 7, pages 923 – 929, July 2004.

[33] J. M. Bonard, J. P. Salvetat, T. Stockli, L. Lorro, A. Chatelain, "Field emission from carbon Nanotubes: perspectives for applications and clues to the emission mechanism," *Journal of Applied Physics A*, Volume 69, pages 245 – 254, 1999.

[34] V. Zhirnov, A. Voronin, E. Givargizov, A. Meshcheryakova, "Emission stability and high current performance of diamond-coated Si emitters," *Journal of Vacuum Science Technology B*, Volume 14, number 3, pages 2034 – 236, May/June 1996.

[35] W. Lu, W. C. Mitchel, C. A. Thornton, W. E. Collins, G. R. Landis, S.R. Smith, "Ohmic Contact behavior of Caron Films on SiC," *Journal of The Electrochemical Society*, Volume 150, number 3, 2003.

[36] W. Lu, W. C. Mitchel, G.R. Landis, T.R. Crenshaw, W. E. Collins, "Ohmic contact properties of Ni/C film on 4H-SiC," *Solid-State Electronics*, Volume 47, pages 2001-2010, 2003.

[37] M. Shur, *Physics of Semiconductor Devices*, Englewood Cliff, NJ: Prentice Hall, Inc., 1990.

[38] D. K. Schroder, *Semiconductor Material and Device Characterization*, New York NY: John Wiley and Sons, Inc., 1990.

[39] M. Dresselhaus, and G. Dresselhaus, "Carbon Nanotures," *Physics World*, January 1998.

[40] F. J. Owens, C. P. Poole, Jr., *Introduction to Nanotechnology*, Hoboken NJ: John Wiley & Sons, Inc., 2003.

[41] H. Bates, O. Brand, G. Fedder, C. Hierold, J. Korvink, O. Tabata, *Enabling Technology for MEMS and Nanodevices*, Weinheim, Germany: Wilely-VCH, 2004.

[42] University of Pennsylvania, Materials Science and Engineering Department website, accessed 10 February 2006, www.seas.upenn.edu/mse/research/nanotubes.html

[43] N. de Jonge, M. Allioux, J. T. Oostveen, "Low noise and stable emission from carbon nanotube electron sources," *Applied Physics Letters*, Number 87, 133118, 23 September 2005.

[44] V. Wong, W. Li, "Bulk Carbon Nanotubes as Sensing Element for Temperature and Anemometry Micro Sensing," Proceedings of the IEEE Micro Electro Mechanical Systems (MEMS), 2003, p 41-44, *IEEE Sixteenth Annual International Conference on MEMS*, Jan 19-23, 2003.

[45] T. Hertel, R. Martel, P. Avouris, "Manipulation of Individual Carbon Nanotubes and Their Interaction with Surfaces," *Journal of Chemistry*, 1998, 102, pages 910-915.

References not cited:

[46] H. Konishi, H. Matsuoka, N. Toyama, N. Naitoh, S. Nishigaki, M. Kusunoki, "Growth control of carbon Nanotubes on silicon carbide surfaces using the laser irradiation effect," *Thin Solid Films*, 464 -465, 2004.

[47] S. C. Kung, K. U. Hwang, I. N. Lin, "Oxygen and ozone oxidation-enhanced field emission of carbon Nanotubes," *Applied Physics Letters*, Volume 80, Number 25, 24 June 2005.

[48] J. Song, M. Sun, Q. Chen, J. Wang, G. Zhang, Z. Xue, "Field emission from carbon Nanotube arrays fabricated by pyrolysis of iron phthalocyanine," *Journal of Physics D: Applied Physics*, Volume 37, pages 5 – 9, 2004.

[49] S. Wind, "Carbon Nanotube Electronics for Future Nanoelectronics," *Proceedings of the IEEE*, April 2003.

[50] P. McEuen, M. Fuhrer, H. Park, "Single-Walled Carbon Nanotube Electronics," *IEEE Transactions on Nanotechnology*, Volume 1, Number 1, March 2002.

Vita

Captain Michael C. Pochet graduated from Suffern High School in Suffern, New York in June 1997. Following high school, he entered undergraduate studies at Virginia Polytechnic Institute and State University in Blacksburg, Virginia. In May 2001, he graduated with a Bachelor of Science degree in Electrical Engineering and was commissioned as a second lieutenant in the United States Air Force through Reserve Officer Training Corps Detachment 875.

His first assignment was at Vandenberg AFB, CA as a developmental engineer assigned to Detachment 9, Space and Missile Systems Center. While at Vandenberg AFB, he completed a Master of Business Administration degree at the University of La Verne in La Verne, California. In August 2004, he entered the Graduate School of Engineering and Management, Air Force Institute of Technology. Upon graduation, he will be assigned to the Air Force Research Laboratory's Directed Energy Directorate at Kirtland AFB, NM.

REPORT DOCUMENTATION PAGE

Form Approved
OMB No. 074-0188

1. REPORT DATE *(DD-MM-YYYY)*	**2. REPORT TYPE**	**3. DATES COVERED** *(From – To)*
23-03-2006	**Master's Thesis**	Sep 2004 – Mar 2006

4. TITLE AND SUBTITLE

Characterization of the Field Emission Properties of Carbon Nanotubes Formed on Silicon Carbide Substrates by Surface Decomposition

5a. CONTRACT NUMBER

5b. GRANT NUMBER

5c. PROGRAM ELEMENT NUMBER

6. AUTHOR(S)

Pochet, Michael, C., Captain, USAF

5d. PROJECT NUMBER

5e. TASK NUMBER

5f. WORK UNIT NUMBER

7. PERFORMING ORGANIZATION NAMES(S) AND ADDRESS(S)
Air Force Institute of Technology
Graduate School of Engineering and Management (AFIT/EN)
2950 Hobson Way
WPAFB OH 45433-7765

8. PERFORMING ORGANIZATION REPORT NUMBER

AFIT/GE/ENG/06-47

9. SPONSORING/MONITORING AGENCY NAME(S) AND ADDRESS(ES)
AFMC AFRL/MLPS
Attn: Dr. John J. Boeckl
3005 Hobson Way, Bldg 651
WPAFB OH 45433-7707 DSN: 785-4474 x3219

10. SPONSOR/MONITOR'S ACRONYM(S)

11. SPONSOR/MONITOR'S REPORT NUMBER(S)

12. DISTRIBUTION/AVAILABILITY STATEMENT
APPROVED FOR PUBLIC RELEASE; DISTRIBUTION UNLIMITED.

13. SUPPLEMENTARY NOTES

14. ABSTRACT

Dense arrays of vertically aligned carbon nanotubes (CNTs) form on the surface of silicon carbide wafers during high temperature anneals under moderate vacuum conditions. The novelty of this growth method is that the CNTs form without the aid of a metal catalyst, allowing for potentially impurity free CNTs to form.

CNT films were grown by the surface decomposition of silicon carbide substrates and the associated field emission characteristics were investigated to determine if films grown using this method possessed advantages over films grown using metal catalyzed methods. The associated turn-on and threshold voltages, maximum current density, and emission current stability of the CNT films were measured using a standard vacuum tube diode test configuration.

Although the samples tested did not demonstrate improved field emission characteristics when compared to values found in the literature for catalyst-grown CNT films, the data collected compares well with data in the literature and shows that further investigation is warranted regarding the emission capabilities of CNT films formed on SiC by surface decomposition. From the measured CNT data, the lowest turn-on electric field was found to be lower than 3.0 V/μm, while exhibiting a high maximum current density of 4.25 mA/cm^2 at 6.7 V/μm.

15. SUBJECT TERMS
Field emission, carbon nanotubes, silicon carbide, surface decomposition.

16. SECURITY CLASSIFICATION OF:			**17. LIMITATION OF ABSTRACT**	**18. NUMBER OF PAGES**	**19a. NAME OF RESPONSIBLE PERSON**
REPORT	**ABSTRACT**	**c. THIS PAGE**			James A. Fellows, Lt Col, USAF (ENG)
U	**U**	**U**	**UU**	180	**19b. TELEPHONE NUMBER** *(Include area code)* (937) 255-3636, ext 7230; e-mail: james.fellows@afit.edu